Modeling and control of overhead cranes: a survey

Mohammad Rasool Mojallizadeh, Bernard Brogliato, Christophe Prieur

Modeling and control of overhead cranes: a survey

Mohammad Rasool Mojallizadeh*[1], Bernard Brogliato†[1], and Christophe Prieur‡[2]

[1]Univ. Grenoble Alpes, INRIA, CNRS, Grenoble INP, LJK, 38000 Grenoble, France

[1]Univ. Grenoble Alpes, GIPSA lab, 38000 Grenoble, France

October 17, 2022

Abstract

In this report, a complete review of the modeling and control schemes employed for overhead cranes has been provided. Different kinds of modeling strategies used for numerical simulations and controllers have been reviewed and their properties and validity have been discussed. Subsequently, the control methods introduced for overhead cranes are reviewed and their characteristics and stability have been analyzed. The studied modeling and control methods are then classified in tabular formats allowing one to select the most appropriate strategy for each specific application at a glance. Finally, some controllers have been selected from each class of controllers and comparative numerical experiments have been made to extract the key characteristics of each method. In the end, some comments and recommendations are provided to select the best modeling and control methods for each specific application.

*mohammad-rasool.mojallizadeh@inria.fr

†bernard.brogliato@inria.fr

‡Christophe.Prieur@gipsa-lab.fr

1 Introduction

Industrial cranes can be found in almost all construction sites and industrial zones. Depending on the application, cranes come in different shapes and configurations such as overhead cranes, boom cranes, tower cranes, mobile cranes, etc. Many other systems also involve flexible cables and certainly share many control and modelling aspects with cranes (helicopters carrying loads suspended to a cable [Ren et al., 2019], cable-driven robotic systems [Lamaury and Gouttefarde, 2013, Merlet, 2017], etc.). Nevertheless this survey work mostly concentrates on the overhead cranes. A 3D view of a typical overhead crane is shown in Fig. 1. As can be seen, a trolley carries the payload through a hoisting cable with length $l(t)$ under tension $T(t)$. The trolley can move in j and k axes to move the payload to a desired place. The length of the cable can also be changed to move the payload in i direction for hoisting the payload. Asynchronous electric motors are usually used as actuators to provide appropriate forces F_h, F_b and F_t in axes i, j and k, respectively.

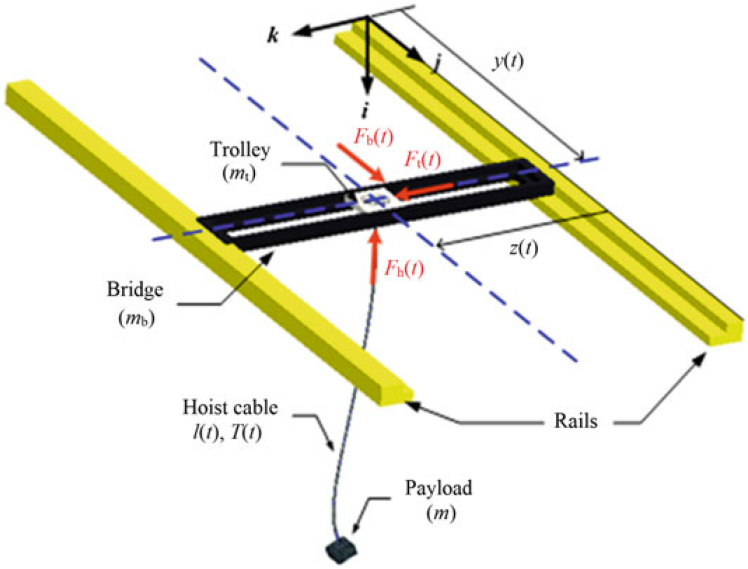

Figure 1: Schematic diagram of an overhead crane [Hong and Shah, 2019]

The main parts of a typical overhead crane are shown in Fig. 2. Appropriate control forces F_b and F_t (see Fig. 1) are applied to the trolley to move it to the desired place and satisfy some control objectives. A hook is usually attached to the cable to carry the payload. The payload is connected to the hook through relatively small links/cables. Hence, this part is usually considered a mass-less rigid body. Cable modeling is probably the most challenging part of the modeling procedure. Other parts of an overhead crane, *e.g.*, electric machines, multi-rope dynamics, nonlinear and nonsmooth effects due to friction, clearances, and backlash, etc. can also be considered in the modeling or in the closed-loop analysis.

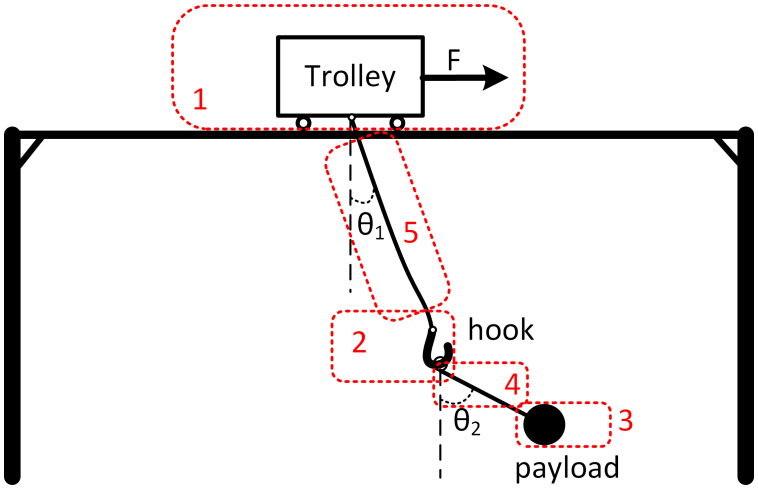

Figure 2: Schematic diagram of an overhead crane in 2D space

2 Modelling aspects: Generalities

Models can be classified according to different criteria: linear *vs* nonlinear, finite-dimensional *vs* infinite-dimensional (PDEs), control design oriented *vs* numerical simulation, 2D operating space *vs* 3D operating space, *etc.* Let us propose a possible classification.

2.1 Models for control

For control-design purposes two main classes have been used so far:

1. Finite-dimensional models with very few degrees of freedom (dof), hence tractable for control design and analysis: trolley+pendulum, where the pendulum is a series kinematic chain made of rigid, or elastic, links with lumped masses at the joints (revolute or spherical). In most of the literature, it has one, or two degrees of freedom (dof). They may be nonlinear (Coriolis and centrifugal torques, gravity torques) or linearized around the vertical posture of the cable. Several subclasses can be considered :

   (a) 2-dimensional (2D) operating space, pendulum-like cable with one or two dofs (or links),

   (b) 3D operating space, pendulum-like cable with one link,

   (c) Single cable cranes,

   (d) Multiple-cable cranes,

   (e) Fixed-length links,

   (f) Variable-length links, with or without control of the length coordinate *via* some winding device,

   (g) links with longitudinal elasticity (and viscous internal damping),

2. Kinematic models: when the payload is related to the trolley with several cables, the detailed kinematics between the cables and the payload have to be modelled to understand the payload manipulation. The trolley+payload system is similar to a cable-driven robotic system. Such models may be used mainly during static postures of the gantry crane, to stabilize the payload.

3. Infinite-dimensional models (ODE+PDEs): trolley+flexible cable. The cable may be represented by a linear wave equation, valid in a neighborhood of the cable's vertical posture (*i.e.*, small angles and small transversal displacement) [d'Andréa Novel et al., 1994, Kim and Hong, 2009, d' Andréa-Novel and Coron, 2000, d'Andréa Novel and Coron, 2002]. Other models consider the cable as an elastic curvilinear domain which can only resist to tensile forces and can only undergo elongation, yielding nonlinear dynamics [Bertrand et al., 2020]. PDEs need to be spatially discretized for simulation and for control application (for instance see [Fatehi et al., 2014]) and yield finite-dimensional Lagrange systems.

It is noteworthy that the models which are used in the control literature, are either nonlinear and with few dofs (typically less than 5), or linear and infinite dimensional (an exception is [Fatehi et al., 2014] where both nonlinearities corresponding to the single-pendulum model and infinite dimensional characteristics of the cable have been taken into account). The literature on cable's modelling is abundant, and many other types of cable models exist [Lv et al., 2020]. However, to the best of the authors' knowledge, these models are barely employed in the control literature, either for control design, or for numerical simulation. The first class is the most used in the Automatic Control literature, by far, see Section 3.5. Different model classes correspond to various control tasks: control of payload's gross motion with compensation of swing or sway angles with very large payload mass (extremely tense cable) or small payload mass (slack/tight cable), attenuation of vibrations in long hoisting ropes under fast trolley motion, control of the payload 3D motion using multiple cables kinematics.

As made clear later, and as a known fact, controlling overhead cranes efficiently, necessarily implies to take into account and use the inertial and dynamical couplings between the state variables, because of their strong underactuation. It is therefore quite useful to characterize rigorously these couplings. This is why it is chosen first to focus on the modeling aspects, before starting the analysis of controllers.

(Linear chains of oscillators) Models as in 1 (g) make the overhead crane a nontrivial extension of linear chains of oscillators whose analysis and control is studied in [Ovseevich and Ananievski, 2021, Ovseevich and Fedorov, 2015]. Then overhead cranes are a kind of nonlinear chain of oscillators. How could the control of cranes with cables in the neighborhood of the vertical posture, benefit from these studies in case of cables with significant longitudinal elasticity? See also section 3.3.4 for relationship with linear chains of oscillators when torsional stiffness is modeled.

2.2 Models for simulation

For the sake of numerical simulation (in order to settle numerical benchmark tests for robustness analysis), several classes of models may be used:

1. Finite-element approximations of wave equation [Egeland and Gravdahl, 2002], of elastic curvilinear domain models [Bertrand et al., 2020], Rayleigh-Ritz discretization [Damaren, 2000].
2. Finite-dimensional models trolley+pendulum with a very large number of pendulum dofs (thus *a priori* untractable for control design). This requires the use of a reliable numerical toolbox able to simulate efficiently a Lagrangian system with typically several tenths of dofs, and also which enables the designer to incorporate neglected dynamics, controller discretization effects. In this work the MATLAB Multibody toolbox (MATLAB2021b).

The boundaries between these two big classes is, of course, never frozen, as new controller design may emerge that use more complex models. The main discrepancy between the models for control design and the models for simulation, is the number of dofs which has to be very large for the latter, so that the cable's flexible modes are well taken into account in the virtual cable. Until now two extreme classes of models seem to be used in the control literature: linear infinite-dimensional and very local (wave equation), and nonlinear finite-dimensional with global dynamics (lumped-mass pendulum). A few number of references, *e.g.,* [Fatehi et al., 2014], have tried to cover both of these extreme cases in a single model. This path is investigated later in this article, see sections 3.1.3, 3.6.1, 3.6.

2.3 Disturbances, uncertainties, neglected dynamics

Also an unwanted effect may be considered as a disturbance, or as being part of the model for control design. In addition to cable flexibilities, other effects considered as disturbances can be incorporated in any of the above for control design or in the numerical benchmarks. Clearly, an efficient simulation toolbox has to incorporate most it not all of these phenomena.

1. Disturbances:
   (a) Coulomb-like friction between the trolley and the rails,
   (b) mechanical play (static or dynamic backlash) at some places like actuators,
   (c) measurement noise (sensors),
   (d) uncertain parameters (inertial parameters), which result in an equivalent disturbance in the closed-loop system.
2. Large parameters variations (*e.g.*, switching between heavy-payload and payload-free subtasks),
3. Neglected dynamics:

(a) actuators dynamics,

(b) cable's flexibilities (for lumped masses pendulum-like models with few dofs),

(c) multiple cables *vs* single cable (kinematics at the payload attachment),

(d) 3D effects (for 2D designs), like payload rotations,

(e) flexibilities in the trolley's dynamics (the trolley being itself a multibody system, and its modelling as a lumped mass point-mass system being an approximation),

(f) flexibilities in the trolley supporting rails,

2.4 Lagrange dynamics in finite dimensions

Let a mechanical system with n degrees of freedom be given, let $q \in I\!R^n$ be the vector of its generalised coordinates, the Lagrange equations are given as:

$$\frac{d}{dt}\frac{\partial L}{\partial \dot{q}} - \frac{\partial L}{\partial q} = Q \tag{1}$$

where $L(q,\dot{q})$ is the Lagrangian function, $L(q,\dot{q}) = T(q,\dot{q}) - U(q)$, $T(q,\dot{q})$ is the system's kinetic energy, $U(q)$ is its potential energy, Q is the vector of generalized forces (that perform work on the coordinate q). It is assumed that q is minimal, which means that there are no redundant coordinates, and (1) describes the system's dynamics without the need to add any equality (bilateral) holonomic constraints. Usually it is much easier to write the dynamics with redundant coordinates, and adding bilateral constraints that represent the joints. As is well-known [Brogliato et al., 2020], the Lagrange dynamics can be rewritten as:

$$M(q)\ddot{q} + C(q,\dot{q})\dot{q} + g(q) = Q \tag{2}$$

where: $M(q) = M^\top(q) \succ 0$ is the mass matrix, or inertia matrix (it may be just $\succcurlyeq 0$), $C(q,\dot{q})\dot{q}$ contains centrifugal and Coriolis nonlinear generalised forces, $g(q) = \frac{\partial U}{\partial q}$ is the vector of forces that derive from a potential (gravity, elasticity, *etc*). The next property is also well-known (since at least the 1980s in the Automatic Control and the Robotics scientific communities):

Property 1 *The matrix $C(q,\dot{q})$, when written with the so-called Christoffel's symbols, verifies*

$$\dot{M}(q,\dot{q}) = C(q,\dot{q}) + C^\top(q,\dot{q}) \quad \Leftrightarrow \quad \dot{M}(q,\dot{q}) - 2C(q,\dot{q}) \quad \textit{is skew-symmetric,} \tag{3}$$

where $\dot{M}(q,\dot{q})$ is the matrix obtained from $M(q)$ by differentiating each one of its entries with respect to time.

Property 1 in (3) is a key property for the design of passivity-based controllers [Brogliato et al., 2020], it implies passivity but it is not implied by passivity. Another fundamental property is that the system (1), seen as an input/output operator $Q \mapsto \dot{q}$, and under a boundedness condition on the potential energy, is passive, *i.e.*, $V(q(t),\dot{q}(t)) - V(q(0),\dot{q}(0)) \leq \int_0^t Q^\top(s)\dot{q}(s)ds$ along the trajectories of the system, and where $V(q,\dot{q}) = T(q,\dot{q}) + U(q)$ is the total mechanical energy.

2.5 Main specific features for control design and analysis

Property 1 is a generic property of Lagrange dynamics, not peculiar to overhead cranes models. Some essential and specific properties of the overhead crane dynamics are the following ones:

1. **Underactuation:** the degree of underactuation d_{unac} is equal to the number of degrees of freedom, minus the number of independent torque inputs in Q. In cranes like in Fig. 2, there are $1+2N$ (with N the number of joints) in the 2D case with varying lengths, or $1+N$ in the 2D case with fixed lengths, or $2+3N$ (3D case with varying lengths) or $2+2N$ in the 3D with fixed lengths, degrees of freedom. In a typical overhead crane, the number of independent inputs varies from 1 (trolley controller in 2D space) to 3 (trolley and length controllers in the 3D space). Thus d_{unac} is usually very large, which makes crane mechanisms occupy a particular place in the class of underactuated systems, which in fact contains a variety of systems [Liu and Yu, 2013].

2. **Dynamical couplings:** in view of large d_{unac}, the couplings between the actuated and the unactuated coordinates dynamics, and between the unactuated coordinates dynamics themselves, play a major role in the general dynamical behaviour of cranes and more specifically in their control.

3. **Passivity:** passivity is one major property of such Lagrange systems. as reminded above. However the passive outputs usually do not correspond to the output to be controlled, mainly due to the noncollocation. Nevertheless a passive mapping can be recovered by defining another suitable output function [Khalilpour et al., 2021, Damaren, 2000].

4. **Output/input collocation or noncollocation:** a pair output/input is said collocated if the feedback is using only the part of the generalized coordinates on which the input torque performs work. For instance the trolley is controlled with the force F which works on the displacement coordinate x, hence the pair (F, x) is collocated. If the actuator dynamics is considered and F is seen as the output of the actuator, then collocation is lost. If F uses the payload's coordinates it is lost also. Noncollocation is known to make the control problem much harder.

5. **High flexibility:** though cables are not the only flexible systems encountered in mechanics, they may be one of the most flexible ones. The high flexibility of cables also leads us to consider various different dynamical regimes:

   - Small amplitude-high frequency waves (vibrations) when the cable stays close to the vertical posture,
   - Large-amplitude motions during which the cable behaves like a pendulum that swings,
   - Large-amplitude waves with lower frequency, which travel through the cable.

An important question for control design is: When do these regimes occur (*i.e.*, with which initial conditions and parameters)? Characterizing the modes of the cable seems mandatory. This may also imply to split the overall control problem into subtasks relying on different models and controllers.

6. **Cables with variable length:** this may be a consequence of cable's longitudinal elasticity, or of winding mechanisms. This is considered in robotic systems involving cables [Khalilpour et al., 2021], in tethered systems with long hoisting ropes (marine or space applications [Quan and Chang, 2020, Kamman and Huston, 2001]). This implies to consider varying cable's total mass (depending on the length in some way) in the derivation of the dynamical equations, and a variation of the trolley's mass as well (the total mass being kept constant). If the length variation is very small the mass variation may be neglected, however [Quan and Chang, 2020].

7. **Cables slackness mode:** cables can exert very large forces when in the tensile mode, however they cannot exert any action when they are slack. Long cables undergoing large oscillations/deformations may undergo such phenomena. This yields models with complementarity constraints [Brogliato, 2016, Example 1.6].

8. **Large variations of the payload mass:** payloads can have very large mass (several tons), and typical tasks involve motions with and without payloads, hence huge variations of the system's inertial parameters. Should this be taken into account designing robust inputs, or adaptive inputs, or switching control strategies?

3 Models: single-cable gantry cranes

This section is dedicated to present the models introduced above, from a general point of view, together with some peculiar properties. The case of gantry cranes with one cable is treated first.

3.1 Lumped-mass models: the trolley-pendulum Lagrange dynamics in 2D operating space

Lumped-mass (multibody) models consist of a multibody system's approach to model cables [Kamman and Huston, 2001, 1985, Huston and Kamman, 1981, 1982, Huston et al., 1978, Winget and Huston, 1981]. As such they can easily handle large deformations and associated nonlinearities. Sometimes they can also be seen as a set of particles linked by suitable potentials. Then they become closer to finite-element spatial (inconsistent) discretization of PDEs, this will be tackled later in this article. Such models are known to be less accurate than those stemming from continuum mechanics Lv et al. [2020], but they have the advantage of being more tractable for control and thus are abundantly used in Robotics.

3.1.1 Calculation of the mass matrix

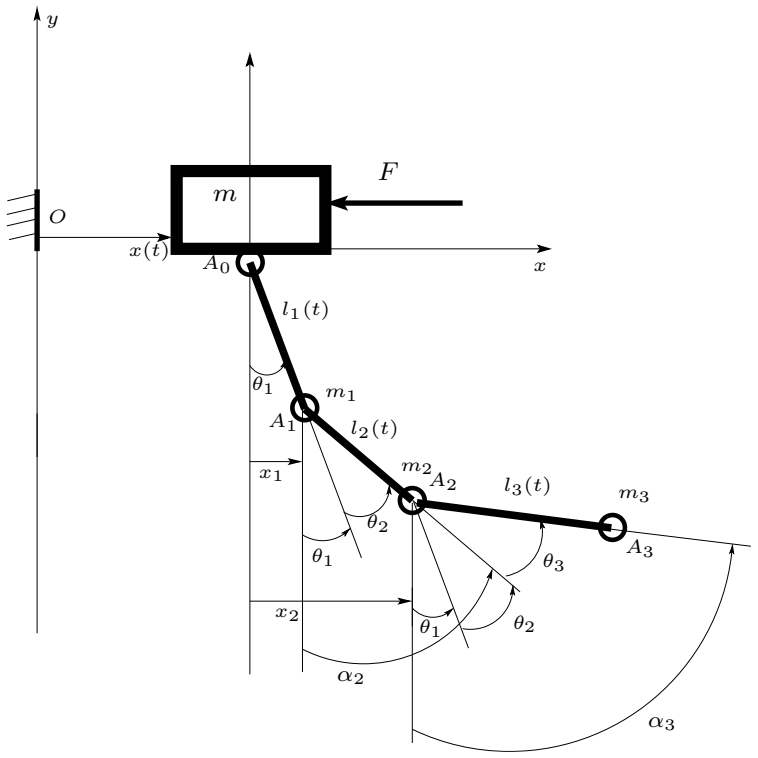

Figure 3: Scheme of an overhead crane (2D operating space), $N = 3$

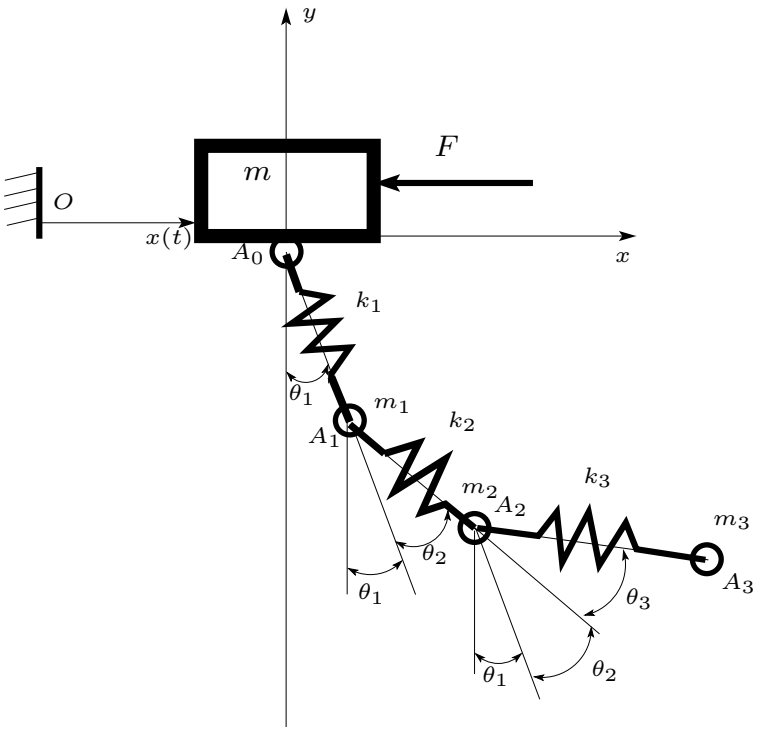

Figure 4: Pendulum with elastic links.

The mass matrix of the system in Figure 3 (2D space with variable length cable) is denoted as:

$$M(q) = \begin{pmatrix} M_{x\theta}(q) & M_{x\theta l}(q) \\ M_{lx\theta}(q) & M_{ll}(q) \end{pmatrix} \in I\!R^{(1+2N)\times(1+2N)}, \tag{4}$$

with $M_{x\theta}(q) \in I\!R^{(1+N)\times(1+N)}$, $M_{ll}(q) \in I\!R^{N\times N}$, and $M_{x\theta l}(q) = M_{lx\theta}^{\top}(q) \in I\!R^{(1+N)\times N}$. It is also possible to go a step further with:

$$M_{x\theta}(q) = \begin{pmatrix} M_{xx}(q) & \bar{M}_{x\theta}(q) \\ \bar{M}_{x\theta}^{\top}(q) & M_{\theta\theta}(q) \end{pmatrix} \tag{5}$$

with $M_{xx}(q) \in I\!R$, $\bar{M}_{x\theta}(q) \in I\!R^{1\times N}$, $M_{\theta\theta}(q) \in I\!R^{N\times N}$.

This expression of the mass matrix corresponds to the choice of the generalized coordinates as $q = (x, \theta_1, \ldots, \theta_N, l_1, \ldots, l_N)^{\top} \in I\!R^{2N+1}$. *Other choices can be made, like those splitting the coordinates into actuated* q_a *and nonactuated ones* q_{na}, *which is a classical way of doing in the Control literature [Reyhanoglu et al., 1999]. This is done below.*

In order to obtain the expressions for the mass submatrices, it is necessary to calculate kinetic energies and then perform differentiations. Roughly speaking, and since we consider that the center of mass G_i of each link is located at the joint A_i, the kinetic energy is equal to the kinetic energy of the centers of mass (N particles), because the inertia operator with respect to $A_i = G_i$ vanishes. In a more general setting where the masses are not lumped, it is possible to model each link as a slender bar with $G_i \neq A_i$, and each bar

has a moment of inertia J_i. Then the total kinetic energy shown below in (11) has to be augmented with terms $\frac{1}{2}J_i\dot{\theta}_i^2$, $1 \leq i \leq N$. When the links' lengths are varying, then $J_i = J_i(t)$. It is sometimes also chosen in the literature to work with a set of nonminimal generalized coordinates $(x_1, y_1, \ldots, x_N, y_N)^\top$ where (x_i, y_i) are the Cartesian coordinates of A_i [Lv et al., 2021]. Since we are interested in Automatic Control, minimal coordinates are usually preferred.

• Kinetic energy of the trolley:

$$T_{trol} = \frac{1}{2}m\dot{x}^2. \tag{6}$$

so that

$$\frac{d}{dt}\frac{\partial T_{trol}}{\partial \dot{x}} = m\ddot{x}. \tag{7}$$

• Translational kinetic energy of each point-mass m_i: let the translational velocity of point A_i be denoted as $V_{A_i} \in I\!R^3$ in the (O, x, y, z) Galilean frame. There is a recursive structure for linear velocities of joints points A_i:

$$V_{A_i} = \begin{pmatrix} \dot{x} \\ 0 \\ 0 \end{pmatrix} + \begin{pmatrix} \sum_{k=1}^{i} l_k \left(\sum_{j=1}^{k} \dot{\theta}_j\right) \cos\left(\sum_{j=1}^{k} \theta_j\right) \\ \sum_{k=1}^{i} l_k \left(\sum_{j=1}^{k} \dot{\theta}_j\right) \sin\left(\sum_{j=1}^{k} \theta_j\right) \\ 0 \end{pmatrix} + \begin{pmatrix} \sum_{k=1}^{i} \dot{l}_k \sin(\sum_{j=1}^{k} \theta_j) \\ -\sum_{k=1}^{i} \dot{l}_k \cos(\sum_{j=1}^{k} \theta_j) \\ 0 \end{pmatrix} \tag{8}$$

The translational kinetic energy of each point mass A_i is $T_{V_{A_i}} = \frac{1}{2}m_i V_{A_i}^\top V_{A_i}$:

$$\begin{array}{rl} T_{V_{A_i}} & = \frac{1}{2}m_i \left(\dot{x} + \sum_{k=1}^{i} l_k \left(\sum_{j=1}^{k} \dot{\theta}_j\right) \cos\left(\sum_{j=1}^{k} \theta_j\right) + \dot{l}_k \sin(\sum_{j=1}^{k} \theta_j)\right)^2 \\ & + \frac{1}{2}m_i \left(\sum_{k=1}^{i} l_k \left(\sum_{j=1}^{k} \dot{\theta}_j\right) \sin\left(\sum_{j=1}^{k} \theta_j\right) - \dot{l}_k \cos(\sum_{j=1}^{k} \theta_j)\right)^2 \end{array} \tag{9}$$

and the total translational kinetic energy of all mass-points is:

$$\begin{array}{rl} T_{trans} & = \frac{1}{2}\sum_{i=1}^{N} m_i \left(\dot{x} + \sum_{k=1}^{i} l_k \left(\sum_{j=1}^{k} \dot{\theta}_j\right) \cos\left(\sum_{j=1}^{k} \theta_j\right) + \dot{l}_k \sin(\sum_{j=1}^{k} \theta_j)\right)^2 \\ & + \frac{1}{2}\sum_{i=1}^{N} m_i \left(\sum_{k=1}^{i} l_k \left(\sum_{j=1}^{k} \dot{\theta}_j\right) \sin\left(\sum_{j=1}^{k} \theta_j\right) - \dot{l}_k \cos(\sum_{j=1}^{k} \theta_j)\right)^2. \end{array} \tag{10}$$

Therefore the total kinetic energy of the system is

$$T(q, \dot{q}) = T_{trol}(\dot{x}) + T_{trans}(\dot{x}, \dot{\theta}_1, \theta_1, \ldots, \dot{\theta}_N, \theta_N, l_1, \dot{l}_1, \ldots, l_N, \dot{l}_N). \tag{11}$$

Remark 1 *A slightly more general model of rigid links modelled as rigid slender rods may be considered. Rotational kinetic energies* $\frac{1}{2}J_i(t)\dot{\theta}_i^2$, $1 \leq i \leq N$, *add terms* $J_i(t)\ddot{\theta}_i + \dot{J}_i(t)\dot{\theta}_i$ *in the Lagrange dynamics. They modify the matrix* $M_{\theta\theta}(q)$ *and the nonlinear terms. If* $J_i(t) = J_i(l(t))$, *then* $J_i(l)\ddot{\theta}_i + \frac{\partial J_i}{\partial l_i}\dot{l}_i\dot{\theta}_i$ *have to be considered. However multibody approaches may not be suitable for modelling variable length cables with winding mechanism at* A_0.

Let us now provide the expressions of the entries of $M(q)$ in (4) and (5), in the general case with varying links' lengths.

Proposition 1 *Let $q = (x, \theta_1, \ldots, \theta_N, l_1, \ldots, l_N)^\top$. The mass matrix entries are calculated as follows:*

- $$m_{11}(q) = m + \sum_{i=1}^{N} m_i \tag{12}$$

- *For $2 \leq p \leq N+1$ (the factor of $\ddot{\theta}_{p-1}$ in the first row of the mass matrix):*

$$m_{1p}(q) = \sum_{i=p-1}^{N} m_i \sum_{k=p-1}^{i} l_k \cos(\sum_{j=1}^{k} \theta_j) \tag{13}$$

In particular the factor of $\ddot{\theta}_N$ is equal to $m_{1(N+1)}(q) = m_N l_N \cos(\sum_{j=1}^{N} \theta_j)$, and the factor of $\ddot{\theta}_1$ is equal to $m_{12}(q) = \sum_{i=1}^{N} m_i \sum_{k=1}^{i} l_k \cos(\sum_{j=1}^{k} \theta_j)$.

- *For $N+2 \leq p \leq 2N+1$ (the factor of $\ddot{l}_{p-N-1}$ in the first row of the mass matrix):*

$$m_{1p}(q) = \sum_{i=p-N-1}^{N} m_i \sin(\sum_{j=1}^{p-N-1} \theta_j), \tag{14}$$

*In particular the factor of $\ddot{l}_N$ (*i.e.*, $p = 2N+1$) is equal to $m_{1(2N+1)}(q) = m_N \sin(\sum_{j=1}^{N} \theta_j)$, and the factor of $\ddot{l}_1$ (*i.e.*, $p = N+2$) is equal to $m_{1(N+2)}(q) = \sum_{i=1}^{N} m_i \sin(\theta_1)$.*

- *The entry $m_{(1+n)1}(q)$ in the mass matrix (which multiplies $\ddot{x}$ in the row corresponding to $\ddot{\theta}_n$, and is thus an entry of $\bar{M}_{x\theta}(q)$ in (5)) is:*

$$m_{(1+n)1}(q) = \sum_{i=n}^{N} m_i \sum_{k=n}^{i} l_k \cos(\sum_{j=1}^{k} \theta_j) \tag{15}$$

- *The entry $m_{(1+n)p}(q)$, $2 \leq p \leq N+1$ which corresponds to $\ddot{\theta}_{p-1}$ in the mass matrix row $M_{(1+n)\bullet}(q)$ of $\ddot{\theta}_n$ (in the submatrix $M_{\theta\theta}(q)$ in (5)) is given by:*

$$m_{(1+n)p}(q) = \sum_{i=\max(n,p-1)}^{N} m_i \sum_{k=p-1}^{i} l_k \left\{ \cos(\sum_{j=1}^{k} \theta_j)(\sum_{k=n}^{i} l_k \cos(\sum_{j=1}^{k} \theta_j)) + \sin(\sum_{j=1}^{k} \theta_j)(\sum_{k=n}^{i} l_k \sin(\sum_{j=1}^{k} \theta_j)) \right\}. \tag{16}$$

This is equal to $m_{p(1+n)}(q)$ by symmetry of $M(q)$.

- *The entry $m_{(1+n)p}(q)$, $N+2 \leq p \leq 2N+1$ which corresponds to $\ddot{l}_{p-N-1}$ in the mass matrix row of $\ddot{\theta}_n$ is given by:*

$$m_{(1+n)p}(q) = \sum_{i=\max(n,p-N-1)}^{N} m_i \left\{ \sin\left(\sum_{j=1}^{p-N-1} \theta_j \right) \sum_{k=n}^{i} l_k \cos(\sum_{j=1}^{k} \theta_j) - \cos\left(\sum_{j=1}^{p-N-1} \theta_j \right) \sum_{k=n}^{i} l_k \sin(\sum_{j=1}^{k} \theta_j) \right\} \tag{17}$$

- *The entry $m_{(1+N+n)p}(q)$, $N+2 \leq p \leq 2N+1$, $1 \leq n \leq N$ is given by:*

$$m_{(1+N+n)p}(q) = \sum_{i=\max(n,p-N-1)}^{N} m_i \cos(\sum_{j=1}^{n} \theta_j - \sum_{j=1}^{p-N-1} \theta_j). \tag{18}$$

Thus for $p = n+N+1$ it follows that $m_{(1+N+n))(1+N+n)}(q) = \sum_{i=n}^{N} m_i$.

The proof with details calculations can be found in [Brogliato, 2022].

The cases $N = 1$ and $N = 2$: these two cases are of interest because quite often used for control design, though rarely derived for both lengths varying. For $N = 1$:

$$M(q) = \begin{pmatrix} m + m_1 & m_1 l_1 \cos(\theta_1) & m_1 \sin(\theta_1) \\ m_1 l_1 \cos(\theta_1) & m_1 l_1^2 & 0 \\ m_1 \sin(\theta_1) & 0 & m_1 \end{pmatrix} = \begin{pmatrix} M_{x\theta_1} & M_{x\theta_1 l_1} \\ M_{x\theta_1 l_1}^\top & M_{ll} \end{pmatrix}. \tag{19}$$

with $M_{ll} = m_1$. For $N = 2$:

$$\begin{cases} m_{11}(q) = m + m_1 + m_2 \\ m_{12}(q) = m_1 l_1 \cos(\theta_1) + m_2(l_1 \cos(\theta_1) + l_2 \cos(\theta_1 + \theta_2)) \\ m_{13}(q) = m_2 l_2 \cos(\theta_1 + \theta_2) \\ m_{14}(q) = (m_1 + m_2) \sin(\theta_1) \\ m_{15}(q) = m_2 \sin(\theta_1 + \theta_2) \end{cases} \tag{20}$$

$$\begin{cases} m_{21}(q) &= m_1 l_1 \cos(\theta_1) + m_2(l_1 \cos(\theta_1) + l_2 \cos(\theta_1 + \theta_2)) \\ m_{22}(q) &= m_1 l_1^2 + m_2 l_1^2 + m_2 l_2^2 + 2 m_2 l_1 l_2 \cos(\theta_2) \\ m_{23}(q) &= m_2 l_1 l_2 \cos(\theta_2) + m_2 l_2^2 \\ m_{24}(q) &= -m_2 l_2 \sin(\theta_2) \\ m_{25}(q) &= m_2 l_1 \sin(\theta_2) \end{cases} \quad \begin{cases} m_{31}(q) &= m_2 l_2 \cos(\theta_1 + \theta_2) \\ m_{32}(q) &= m_2 l_1 l_2 \cos(\theta_2) + m_2 l_2^2 \\ m_{33}(q) &= m_2 l_2^2 \\ m_{34}(q) &= -m_2 l_2 \sin(\theta_2) \\ m_{35}(q) &= 0 \end{cases} \tag{21}$$

$$\begin{cases} m_{41}(q) &= (m_1 + m_2) \sin(\theta_1) = m_{14}(q) \\ m_{42}(q) &= -m_2 l_2 \sin(\theta_2) = m_{24}(q) \\ m_{43}(q) &= -m_2 l_2 \sin(\theta_2) = m_{34}(q) \\ m_{44}(q) &= m_1 + m_2 \\ m_{45}(q) &= m_2 \cos(\theta_2) \end{cases} \quad \begin{cases} m_{51}(q) &= m_2 \sin(\theta_1 + \theta_2) = m_{15}(q) \\ m_{52}(q) &= m_2 l_1 \sin(\theta_2) = m_{25}(q) \\ m_{53}(q) &= 0 = m_{35}(q) \\ m_{54}(q) &= m_2 \cos(\theta_2) = m_{45}(q) \\ m_{55}(q) &= m_2 \end{cases} \tag{22}$$

Fixed-length links: Let us now assume that $q = (x, \theta_1, \ldots, \theta_N, l_1)^\top \in I\!R^{2+N}$, *i.e.*, all links have fixed length excepted the first one. This may be due to lumping the longitudinal elasticity in the first link, or to a winding device mounted at node A_0. Then the cable's length variation may be lumped in the first link, *i.e.*, $l_1(t)$ is varying while the other links are constant. The kinetic energy in (10) becomes equal to:

$$\begin{aligned} T_{trans} &= \tfrac{1}{2} \textstyle\sum_{i=1}^N m_i \left(\dot{x} + \dot{l}_1 \sin(\theta_1) + \sum_{k=1}^i l_k \left(\sum_{j=1}^k \dot{\theta}_j \right) \cos\left(\sum_{j=1}^k \theta_j \right) \right)^2 \\ &\quad + \tfrac{1}{2} \textstyle\sum_{i=1}^N m_i \left(-\dot{l}_1 \cos(\theta_1) + \sum_{k=1}^i l_k \left(\sum_{j=1}^k \dot{\theta}_j \right) \sin\left(\sum_{j=1}^k \theta_j \right) \right)^2. \end{aligned} \tag{23}$$

Calculations yield:

$$
\begin{array}{ll}
\frac{d}{dt}\frac{\partial T_{trans}}{\partial \dot{\theta}_n} & = \sum_{i=n}^{N} m_i \left(\ddot{x} + 2\dot{l}_1\dot{\theta}_1 \cos(\theta_1) + \ddot{l}_1 \sin(\theta_1) + \sum_{k=1}^{i} l_k \left(\sum_{j=1}^{k} \ddot{\theta}_j \right) \cos(\sum_{j=1}^{k} \theta_j) \right. \\
& \left. - \sum_{k=1}^{i} l_k \left(\sum_{j=1}^{k} \dot{\theta}_j \right)^2 \sin(\sum_{j=1}^{k} \theta_j) \right) \left(\sum_{k=n}^{i} l_k \cos(\sum_{j=1}^{k} \theta_j) \right) \\
& + \sum_{i=n}^{N} m_i \left(\dot{x} + \dot{l}_1 \sin(\theta_1) + \sum_{k=1}^{i} l_k \left(\sum_{j=1}^{k} \dot{\theta}_j \right) \cos\left(\sum_{j=1}^{k} \theta_j \right) \right) \\
& \times \left(\sum_{k=n}^{i} -l_k (\sum_{j=1}^{k} \dot{\theta}_j) \sin(\sum_{j=1}^{k} \theta_j) + \left\{ \begin{array}{lll} \dot{l}_1 \cos(\theta_1) & \text{if} & n = 1 \\ 0 & \text{if} & n \geq 2 \end{array} \right. \right) \\
& + \sum_{i=n}^{N} m_i \left(2\dot{l}_1\dot{\theta}_1 \sin(\theta_1) - \ddot{l}_1 \cos(\theta_1) + \sum_{k=1}^{i} l_k \left(\sum_{j=1}^{k} \dot{\theta}_j \right)^2 \cos(\sum_{j=1}^{k} \theta_j) \right. \\
& \left. + l_k \left(\sum_{j=1}^{k} \ddot{\theta}_j \right) \sin(\sum_{j=1}^{k} \theta_j) \right) \left(\sum_{k=n}^{i} l_k \sin(\sum_{j=1}^{k} \theta_j) \right) \\
& + \sum_{i=n}^{N} m_i \left(-\dot{l}_1 \cos(\theta_1) + \sum_{k=1}^{i} l_k \left(\sum_{j=1}^{k} \dot{\theta}_j \right) \sin\left(\sum_{j=1}^{k} \theta_j \right) \right) \\
& \times \left(\sum_{k=n}^{i} l_k (\sum_{j=1}^{k} \dot{\theta}_j) \cos(\sum_{j=1}^{k} \theta_j) + \left\{ \begin{array}{lll} \dot{l}_1 \sin(\theta_1) & \text{if} & n = 1 \\ 0 & \text{if} & n \geq 2 \end{array} \right. \right)
\end{array}
\tag{24}
$$

Remark 2 *In case of a winding mechanism, the cable's total mass varies with its length,* i.e., $m_1 = m_1(l_1)$. *In all rigor this has to be taken into account when deriving the Lagrange dynamics. If $l_1(t)$ varies little then this may be neglected [Quan and Chang, 2020]. In some applications cables' lengths vary a lot and this dependence becomes mandatory modelling. From (23) the part of kinetic energy that depends on $m_1(l_1)$ is given by $\frac{1}{2}m_1(l_1)\left\{ \left(\dot{x} + \dot{l}_1 \sin(\theta_1) + l_1\dot{\theta}_1 \cos(\theta_1) \right)^2 + \left(-\dot{l}_1 \cos(\theta_1) + l_1\dot{\theta}_1 \sin(\theta_1) \right)^2 \right\}$. Using (24) it follows that this does not modify the mass matrix structure but it adds the nonlinear torque*

$$
\frac{1}{2}\frac{\partial m_1}{\partial l_1}\dot{l}_1 \left\{ \left(\dot{x} + \dot{l}_1 \sin(\theta_1) + l_1\dot{\theta}_1 \cos(\theta_1) \right)^2 + \left(-\dot{l}_1 \cos(\theta_1) + l_1\dot{\theta}_1 \sin(\theta_1) \right)^2 \right\} \tag{25}
$$

in the dynamics, for $\frac{d}{dt}\frac{\partial T_{trans}}{\partial \dot{\theta}_1}$. These nonlinearities contain velocity cubic terms $\dot{l}_1^3$ (cubic nonlinearities in position *are present in 3D 1-link pendulum [Abdel-Rahman et al., 2003]).*

- Row $M_{1\bullet}(q) = M_{\bullet 1}^{\top}(q)$:

$$
m_{11}(q) = m + \sum_{i=1}^{N} m_i \tag{26}
$$

$$
m_{1(N+2)}(q) = \sin(\theta_1) \sum_{i=1}^{N} m_i \tag{27}
$$

which is (14) for $p = N + 2$, and for $2 \leq n \leq N + 1$ ($m_{1n}(q)$ is the factor of $\ddot{\theta}_{n-1}$ in $M_{1\bullet}(q)\ddot{q}$):

$$
m_{1n}(q) = \sum_{i=n-1}^{N} m_i \sum_{k=n-1}^{i} l_k \cos(\sum_{j=1}^{k} \theta_j), \tag{28}
$$

which is (13).

• Row $M_{n\bullet}(q)$, $2 \leq n \leq N+1$: the entry multiplying $\ddot{\theta}_{p-1}$, $2 \leq p \leq N+1$, is:

$$m_{np}(q) = \sum_{i=\max(n-1,p-1)}^{N} m_i \sum_{k=p-1}^{i} l_k \left\{ \cos(\sum_{j=1}^{k}\theta_j)(\sum_{k=n-1}^{i} l_k \cos(\sum_{j=1}^{k}\theta_j)) + \sin(\sum_{j=1}^{k}\theta_j)(\sum_{k=n-1}^{i} l_k \sin(\sum_{j=1}^{k}\theta_j)) \right\}. \tag{29}$$

And the entry that multiplies $\ddot{x}$ in the row $M_{n\bullet}(q)$, $2 \leq n \leq N+1$, which corresponds to $\ddot{\theta}_{n-1}$, is:

$$m_{n1}(q) = \sum_{i=n-1}^{N} m_i \sum_{k=n-1}^{i} l_k \cos(\sum_{j=1}^{k}\theta_j) \tag{30}$$

One sees that this is equal to (28) which confirms the symmetry of $M(q)$ with $M_{1\bullet}(q) = M_{\bullet 1}^{\top}(q)$. Finally the factor of $\ddot{l}_1$ is:

$$m_{n(N+2)}(q) \quad = \sum_{i=n-1}^{N} m_i \sum_{k=n-1}^{i} l_k \sin(\theta_1 - \sum_{j=1}^{k}\theta_j) \tag{31}$$

• Row $M_{(N+2)\bullet}(q)$: the entry multiplying $\ddot{x}$ is:

$$m_{(N+2)1}(q) = \sin(\theta_1) \sum_{i=1}^{N} m_i, \tag{32}$$

which is (27), and for $2 \leq p \leq N+1$:

$$m_{(N+2)p}(q) = \sum_{i=p-1}^{N} m_i \sum_{k=p-1}^{i} l_k \sin(\theta_1 - \sum_{j=1}^{k}\theta_j) \tag{33}$$

Case $N = 2$: In case $N = 2$ the 4×4 mass matrix is equal to:

$$M(q) = \begin{pmatrix} m + m_1 + m_2 & m_1 l_1 \cos(\theta_1) + m_2(l_1 \cos(\theta_1) + l_2 \cos(\theta_1 + \theta_2)) & m_2 l_2 \cos(\theta_1 + \theta_2) & (m_1 + m_2)\sin(\theta_1) \\ m_1 l_1 \cos(\theta_1) + m_2(l_1 \cos(\theta_1) + l_2 \cos(\theta_1 + \theta_2)) & m_1 l_1^2 + m_2(l_1^2 + l_2^2) + 2m_1 l_1 l_2 \cos(\theta_2) & m_2 l_2^2 + m_2 l_1 l_2 \cos(\theta_1) & -m_2 l_2 \sin(\theta_2) \\ m_2 l_2 \cos(\theta_1 + \theta_2) & m_2 l_2^2 + m_2 l_1 l_2 \cos(\theta_2) & m_2 l_2^2 & -m_2 l_2 \sin(\theta_2) \\ (m_1 + m_2)\sin(\theta_1) & -m_2 l_2 \sin(\theta_2) & -m_2 l_2 \sin(\theta_2) & m_1 + m_2 \end{pmatrix} \tag{34}$$

3.1.2 Properties of the mass matrix

The next lemma state some generic features of the mass matrix, with varying and constant links' lengths.

Lemma 1 *Let $N \geq 1$ and $q = (x, \theta_1, \theta_2, \ldots, \theta_N, l_1, l_2, \ldots, l_N)^{\top}$. Consider the mass matrix in (4) and (5).*

1. *If small angles are considered (the cable stays in a neighbordhood of the vertical position) with a zero-order approximation,* i.e., $\sin(\theta_i) \approx \theta_i \approx 0$, *then the mass matrix in (4) (5) has the block-diagonal form:*

$$M(q) = \begin{pmatrix} M_{x\theta}(q) & 0 \\ 0 & M_{ll} \end{pmatrix} \tag{35}$$

where $0 \prec M_{x\theta}(q) \in \mathbb{R}^{(1+N)\times(1+N)}$, $0 \prec M_{ll} \in \mathbb{R}^{N\times N}$, and M_{ll} is constant.

2. *If the first order approximation is chosen,* i.e., $\sin(\theta_i) \approx \theta_i$, *then the off-block-diagonal terms $M_{x\theta l}$ and $M_{lx\theta}$ are proportional to the angles θ_i and sums of them.*

3. *The matrix $M_{ll}(q)$ always has constant diagonal entries m_{nn} equal to $\sum_{j=1}^{n} m_j$. The matrix $M_{xx}(q)$ is the entry m_{11} and is constant.*

4. *The matrix $M_{x\theta}(q)$ has entries proportional to angles cosines, or to the sum of cosines and sines, and thus remains bounded away from zero in the neighborhood of the cable's vertical posture (roughly speaking, the inertial couplings between the trolley's and the angle's accelerations, are not weak around the vertical posture).*

5. *The submatrix $M_{\theta\theta}(q)$ has entries made of sums of terms functions of products of cosines only, and of products of sines only. Hence they remain nonlinear in the angles (including terms like $\theta_i\theta_j$) if the first order approximation is chosen. Also the inertial couplings inside $M_{\theta\theta}(q)$ are strong, in the sense that they remain bounded away from zero even in the neighborhood of the cable's vertical posture.*

6. *The submatrix $\bar{M}_{x\theta}(q)$ has entries linear in l_k if the first and second order approximations are chosen.*

7. *The small angles assumption (even the zero order approximation) does not imply that the Coriolis/-centrifugal nonlinearities vanish in the case of varying lengths: products $\dot{l}_j\dot{\theta}_k$ and $l_k\theta_j$ are still present.*

8. *In case of large payload mass, the mass matrix becomes bad-conditionned, since $M_{ll}(q)$ loses its rank around the vertical position when $m_i = 0$, $1 \leq i \leq N-1$, and has low rank when in addition the zero order approximation for small angles is made.*

Using the above equations (26)–(33) it follows that same conclusions hold for the mass matrix when $q = (x, \theta_1, \ldots, \theta_N, l_1)^\top$. Then the following results hold.

Lemma 2 *Let $q = (x, \theta_1, \ldots, \theta_N, l_1)^\top$, then the mass matrix in (4) and (5) has the following properties:*

1. *M_{xx} and M_{ll} are scalar constant positive entries.*

2. *The coupling column $M_{x\theta l}(q) \in \mathbb{R}^{(N+1)\times 1}$ is weak in the neighborhood of the cable's vertical posture, since it is proportional to angles sines.*

3.1.3 Different generalized coordinates

It is always interesting, both for Control or for Numerical Simulation sake, to investigate the influence of different generalized coordinates on the Lagrange dynamics structure.

Generalized coordinates with different angles: Most of the authors work with different angles $\alpha_i = \sum_{j=1}^{i} \theta_j$, with generalized coordinate $q_\alpha = (x, \alpha_1, \ldots, \alpha_N, l_1, \ldots, l_N)^\top$, see Figure 3. The transformation

matrix $q_\alpha = Tq$ is given by $T = \begin{pmatrix} 1 & 0 & 0 \\ 0 & J & 0 \\ 0 & 0 & I_N \end{pmatrix}$, $J \in I\!R^{N\times N}$, with :

$$J = \begin{pmatrix} 1 & 0 & 0 & \dots & 0 & 0 & 0 \\ 1 & 1 & 0 & 0 & \dots & 0 & 0 \\ 1 & 1 & 1 & 0 & 0 & \dots & 0 \\ \vdots & \vdots & & & & & \vdots \\ 1 & 1 & 1 & \dots & 1 & 1 & 0 \\ 1 & 1 & 1 & \dots & & 1 & 1 \end{pmatrix} \quad J^{-1} = \begin{pmatrix} 1 & 0 & 0 & 0 & \dots & 0 & 0 \\ -1 & 1 & 0 & 0 & \dots & & 0 \\ 0 & -1 & 1 & 0 & \dots & & 0 \\ \vdots & \vdots & & & & & \vdots \\ 0 & 0 & \dots & 0 & -1 & 1 & 0 \\ 0 & 0 & \dots & & 0 & -1 & 1 \end{pmatrix} \tag{36}$$

The matrix J is full-rank Toeplitz [Bernstein, 2009, Definition 3.1.3], and its inverse is calculated using [Bernstein, 2009, Fact 3.18.11]. Then

$$\begin{aligned} M_\alpha(q_\alpha) \quad &= T^{-\top} M(q) T^{-1} = \begin{pmatrix} 1 & 0 & 0 \\ 0 & J^{-\top} & 0 \\ 0 & 0 & I_N \end{pmatrix} M(q) \begin{pmatrix} 1 & 0 & 0 \\ 0 & J^{-1} & 0 \\ 0 & 0 & I_N \end{pmatrix} \\ &= \begin{pmatrix} 1 & 0 & 0 \\ 0 & J^{-\top} & 0 \\ 0 & 0 & I_N \end{pmatrix} \begin{pmatrix} M_{x\theta}(q) & 0 \\ 0 & M_{ll} \end{pmatrix} \begin{pmatrix} 1 & 0 & 0 \\ 0 & J^{-1} & 0 \\ 0 & 0 & I_N \end{pmatrix} \\ &= \begin{pmatrix} \begin{pmatrix} 1 & 0 \\ 0 & J^{-\top} \end{pmatrix} M_{x\theta}(q) \begin{pmatrix} 1 & 0 \\ 0 & J^{-1} \end{pmatrix} & 0 \\ 0 & M_{ll} \end{pmatrix} = \begin{pmatrix} M_{x\alpha}(q_\alpha) & 0 \\ 0 & M_{ll} \end{pmatrix}. \end{aligned} \tag{37}$$

Therefore the conclusions of Lemma 1 still hold in the new coordinates.

Generalized coordinates with horizontal positions of the joints: Let us analyse the system when the coordinates are the horizontal coordinates of each point-mass A_i: $x_i = x + \sum_{j=1}^{i} l_j \sin(\sum_{k=1}^{j} \theta_k)$, and the angles θ_i, see Figure 3. The small angle and large payload mass assumptions are made to ease the calculations of the transformation (which otherwise involves trigonometric functions): $x_i = x + \sum_{j=1}^{i} l_j(\sum_{k=1}^{j} \theta_k)$. It is noteworthy that this type of coordinates together with the small angles assumptions, are used in some PDEs approaches [d'Andréa Novel et al., 1994, d' Andréa-Novel and Coron, 2000, d'Andréa Novel and Coron, 2002, Kim and Hong, 2009, Alli and Singh, 1998, He and Ge, 2016]. The new generalized coordinate is $q_x = (x, \theta_1, \dots, \theta_N, x_1, \dots, x_N)^\top$, and the transformation from q to q_x is nonlinear: $q_x = Q(q)$, hence $\dot{q}_x = \frac{\partial Q}{\partial q}(q)\dot{q}$ and $\ddot{q}_x = \frac{\partial Q}{\partial q}(q)\ddot{q} + \frac{d}{dt}\left(\frac{\partial Q}{\partial q}\right)(q,\dot{q})\dot{q}$. In the new coordinates $M_x(q_x) = \frac{\partial Q}{\partial q}^{-\top} M(q) \frac{\partial Q}{\partial q}^{-1}$. We

have:

$$\frac{\partial Q}{\partial q}(q) = \begin{pmatrix} I_{N+1} & 0 \\ 1 & \\ \vdots & Q_L \quad Q_\theta \\ 1 & \end{pmatrix}, \tag{38}$$

with:

$$Q_L = \begin{pmatrix} l_1 & 0 & \dots & & 0 \\ l_1+l_2 & l_2 & 0 & \dots & 0 \\ l_1+l_2+l_3 & l_2+l_3 & l_3 & 0 \quad \dots & 0 \\ \vdots & & & & \vdots \\ \vdots & & & l_{N-1} & 0 \\ \sum_{k=1}^N l_k & \sum_{k=2}^N l_k & \dots & l_{N-1}+l_N & l_N \end{pmatrix} \quad Q_\theta = \begin{pmatrix} \theta_1 & 0 & \dots & & 0 \\ \theta_1 & \theta_1+\theta_2 & 0 & \dots & 0 \\ \vdots & \vdots & & & \vdots \\ \vdots & \vdots & & & 0 \\ \theta_1 & \theta_1+\theta_2 & \dots & & \sum_{k=1}^N \theta_k \end{pmatrix} \tag{39}$$

Clearly Q_θ is not invertible at $\theta_1 = 0$, *etc*, its determinant being equal to $\theta_1(\theta_1+\theta_2)\dots(\sum_{k=1}^N \theta_k)$, and neither is $\frac{\partial Q}{\partial q}(q)$ at these angles, because the lengths l_k cannot be obtained from q_x at those coordinates values. From the matrix inversion Lemma:

$$\frac{\partial Q}{\partial q}^{-1}(q) = \begin{pmatrix} I_{N+1} & 0 \\ -Q_\theta^{-1}\bar{Q}_L & Q_\theta^{-1} \end{pmatrix} \tag{40}$$

with $\bar{Q}_L = \begin{pmatrix} 1 & \\ \vdots & Q_L \\ 1 & \end{pmatrix}$, and $(\dot{x}_1, \dots, \dot{x}_N)^\top = \bar{Q}_L\dot{\theta} + Q_\theta \dot{L}$, $L = (l_1, \dots, l_N)^\top$. Therefore:

$$M_x(q_x) = \begin{pmatrix} I_{N+1} & -(Q_\theta^{-1}\bar{Q}_L)^\top \\ 0 & Q_\theta^{-\top} \end{pmatrix} \begin{pmatrix} M_{x\theta}(q) & M_{x\theta l}(q) \\ M_{lx\theta}(q) & M_{ll}(q) \end{pmatrix} \begin{pmatrix} I_{N+1} & 0 \\ -Q_\theta^{-1}\bar{Q}_L & Q_\theta^{-1} \end{pmatrix} \tag{41}$$

Pure horizontal motion of the nodes A_i: In order to analyze the dynamics using the positions x_i let us try to start directly with the kinetic energy, doing some basic assumptions as done in the PDEs approaches [Egeland and Gravdahl, 2002, section 9.3.1] [d' Andréa-Novel and Coron, 2000, d'Andréa Novel and Coron, 2002, d'Andréa Novel et al., 1994, Kim and Hong, 2009], like pure horizontal motion of the nodes. In this case $q = (x, x_1, x_2, \dots, x_N)^\top$, $V_{A_i} = \dot{x} + \dot{x}_i$, and the total kinetic energy is $T = \frac{1}{2}m\dot{x}^2 + \frac{1}{2}\sum_{i=1}^N m_i\dot{x}_i^2$. In this case the mass matrix is linear invariant with $M(q) = \mathrm{diag}(m, m_1, \dots, m_N)$, and the Lagrange dynamics is easily obtained once the potential energy is known. The bending elasticity corresponds to joint stiffness, and it is linear. Then the Lagrange dynamics is:

$$M\ddot{q}(t) + K_{flex}q(t) = Q(t), \tag{42}$$

for some stiffness matrix K_{flex}.

Remark 3 *It is interesting to note that the spatial discretization of the wave (string) equation, yields for a particular choice of the basis functions, a tridiagonal mass matrix (named the consistent mass matrix), while the diagonal mass matrix obtained from lumped masses is named the nonconsistent mass matrix [Egeland and Gravdahl, 2002, Example 14.7].*

Nodes Cartesian coordinates: each node A_i has coordinates (x_i, y_i) in the Cartesian frame (O, x, y). Hence $q = (x, x_1, \ldots, x_N, y_1, \ldots, y_N)^\top$. The kinetic energy associated with each node is $T_i = \frac{1}{2} m_i(\dot{x}_i^2 + \dot{y}_i^2)$, $1 \leq i \leq N$. The pendulum is seen as a set of N particles (in 2D or in 3D spaces with a third coordinate z_i), with mass matrix $M(q) = M = \text{blockdiag}(m, \text{diag}(m_i), \text{diag}(m_i))$. In case of fixed links' lengths l_i, the coordinates have to satisfy equality holonomic constraints $(x_i - x_{i-1})^2 + (y_i - y_{i-1})^2 = l_i^2$, which can be treated classically either using Lagrange multipliers associated with the constraints [Kamman and Huston, 2001], or reducing coordinates by eliminating N redundant coordinates. In case of elastic links the potential energy is $U_{elas} = \sum_{i=1}^N \frac{1}{2} k_i (l_i - l_{i,r})^2 = \sum_{i=1}^N \frac{1}{2} k_i (\sqrt{(x_i - x_{i-1})^2 + (y_i - y_{i-1})^2} - l_{i,r})^2$, where $l_{i,r}$ are the springs' lengths at rest. Thus $\frac{\partial U_{elas}}{\partial x_n} = k_n(l_n - l_{n,r}) \frac{\partial l_n}{\partial x_n} + k_{n+1}(l_{n+1} - l_{n+1,r}) \frac{\partial l_{n+1}}{\partial x_n} = k_n(l_n - l_{n,r}) \frac{x_n - x_{n-1}}{\sqrt{(x_n - x_{n-1})^2 + (y_n - y_{n-1})^2}} - k_{n+1}(l_{n+1} - l_{n+1,r}) \frac{x_{n+1} - x_n}{\sqrt{(x_{n+1} - x_n)^2 + (y_{n+1} - y_n)^2}}$, $1 \leq n \leq N-1$, $\frac{\partial U_{elas}}{\partial x} = k_1(l_1 - l_{1,r}) \frac{\partial l_1}{\partial x} = -k_1(l_1 - l_{1,r}) \frac{x_1 - x_0}{\sqrt{x_1 - x_0)^2 + (y_1 - y_0)^2}}$, and $\frac{\partial U_{elas}}{\partial x_N} = k_N(l_N - l_{N,r}) \frac{\partial l_N}{\partial x_N} = k_N(l_N - l_{N,r}) \frac{x_N - x_{N-1}}{\sqrt{(x_N - x_{N-1})^2 + (y_N - y_{N-1})^2}}$. Therefore the forces that derive from the elastic potential are nonlinear, and the Lagrange dynamics takes the form (compare with (42)):

$$M\ddot{q}(t) + K_{elas}(q(t))q(t) = Q(t) \tag{43}$$

where it is assumed that $x_0 = x$. The stiffness matrix $K_{elas}(q)$ is given by:

$$\begin{pmatrix} \frac{k_1(l_1 - l_{1,r})}{|l_1|} & -\frac{k_1(l_1 - l_{1,r})}{|l_1|} & 0 & 0 & & \ldots & 0 \\ -\frac{k_1(l_1 - l_{1,r})}{|l_1|} & \frac{k_1(l_1 - l_{1,r})}{|l_1|} + \frac{k_2(l_2 - l_{2,r})}{|l_2|} & -\frac{k_2(l_2 - l_{2,r})}{|l_2|} & 0 & & \ldots & 0 \\ 0 & -\frac{k_2(l_2 - l_{2,r})}{|l_2|} & \frac{k_2(l_2 - l_{2,r})}{|l_2|} + \frac{k_3(l_3 - l_{3,r})}{|l_3|} & -\frac{k_3(l_3 - l_{3,r})}{|l_3|} & 0 & \ldots & 0 \\ \vdots & & & & & & \vdots \\ 0 & \ldots & & & \ldots & 0 & -\frac{k_N(l_N - l_{N,r})}{|l_N|} \quad \frac{k_N(l_N - l_{N,r})}{|l_N|} \end{pmatrix} \tag{44}$$

It is a tridiagonal matrix, and the operator $Q \mapsto \dot{q}$ is passive lossless with storage function $\frac{1}{2}\dot{q}^\top M\dot{q} + U_{elas}(q)$. Joint angular stiffness can be modelled also, where the angles are given by (see Figure 3): $\theta_i = \arctan\left(\frac{x_i - x_{i-1}}{y_{i-1} - y_i}\right) - \arctan\left(\frac{x_{i-1} - x_{i-2}}{y_{i-2} - y_{i-1}}\right)$, $2 \leq i \leq N$, and $\theta_1 = \arctan\left(\frac{x_1 - x_0}{y_0 - y_1}\right)$. The potential energy associated with joint stiffness is $U_{flex}(q) = \frac{1}{2} \sum_{i=1}^N \kappa_{i-1} \theta_i^2 = \frac{1}{2} \sum_{i=2}^N \kappa_{i-1} \left(\arctan\left(\frac{x_i - x_{i-1}}{y_{i-1} - y_i}\right) - \arctan\left(\frac{x_{i-1} - x_{i-2}}{y_{i-2} - y_{i-1}}\right)\right)^2 +$

$\frac{1}{2}\kappa_0 \arctan^2\left(\frac{x_1-x_0}{y_0-y_1}\right)$, where κ_i is the angular stiffness at node A_i. Calculations yield:

$$\begin{aligned}\frac{\partial U_{flex}}{\partial x_n} &= \frac{(\kappa_{n-1}-\kappa_n)\arctan(\frac{x_n-x_{n-1}}{y_{n-1}-y_n})+(\kappa_n-\kappa_{n-1})\arctan(\frac{x_{n+1}-x_n}{y_n-y_{n+1}})}{(y_n-y_{n-1})^2+(x_n-x_{n-1})^2}y_{n-1}\\ &+\frac{\kappa_{n+1}\left(\arctan(\frac{x_{n+2}-x_{n+1}}{y_{n+1}-y_{n+2}})-\arctan(\frac{x_{n+1}-x_n}{y_n-y_{n+1}})\right)-\kappa_n\left(\arctan(\frac{x_{n+1}-x_n}{y_n-y_{n+1}})-\arctan(\frac{x_n-x_{n-1}}{y_{n-1}-y_n})\right)}{(y_n-y_{n+1})^2+(x_{n+1}-x_n)^2}y_n\\ &-\frac{\kappa_n\left(\arctan(\frac{x_{n+1}-x_n}{y_n-y_{n+1}})-\arctan(\frac{x_n-x_{n-1}}{y_{n-1}-y_n})\right)+\kappa_{n-1}\left(\arctan(\frac{x_n-x_{n-1}}{y_{n-1}-y_n})-\arctan(\frac{x_{n-1}-x_{n-2}}{y_{n-2}-y_{n-1}})\right)}{(y_n-y_{n-1})^2+(x_n-x_{n-1})^2}y_n\\ &\frac{\kappa_n\left(\arctan(\frac{x_{n+1}-x_n}{y_n-y_{n+1}})-\arctan(\frac{x_n-x_{n-1}}{y_{n-1}-y_n})\right)-\kappa_{n+1}\left(\arctan(\frac{x_{n+2}-x_{n+1}}{y_{n+1}-y_{n+2}})-\arctan(\frac{x_{n+1}-x_n}{y_n-y_{n+1}})\right)}{(y_n-y_{n+1})^2+(x_{n+1}-x_n)^2}y_{n+1}\end{aligned} \tag{45}$$

for $2 \leq n \leq N-1$, $\frac{\partial U_{flex}}{\partial x_N} = \frac{\kappa_{N-1}\left(\arctan\left(\frac{x_N-x_{N-1}}{y_{N-1}-y_N}\right)-\arctan\left(\frac{x_{N-1}-x_{N-2}}{y_{N-2}-y_{N-1}}\right)\right)}{(y_{N-1}-y_N)^2+(x_N-x_{N-1})^2}(y_{N-1}-y_N)$, and a similar expression is calculated for $\frac{\partial U_{flex}}{\partial x_0}$. This again yields a nonlinear stiffness generalized force of the form $K_{flex}(q)q$, where $K_{flex}(q)$ has a block diagonal form. Hence the joint and the links elasticities yields Lagrange dynamics:

$$M\ddot{q}(t) + K_{elas}(q(t))q(t) + K_{flex}(q(t))q(t) = Q(t). \tag{46}$$

3.1.4 Very large payload mass

When the crane carries very large payloads (this may be in certain applications several tenths of tons), it it legitimate to model the cables as massless bodies. Consider $q = (x, \theta_1, \ldots, \theta_N, l_1, \ldots, l_N)^\top$. Let us investigate how the mass matrix properties change if it is assumed that $m_N \ggg m_i$, $1 \leq i \leq N-1$, which may be interpreted as a massless cable with $m_i = 0$, $1 \leq i \leq N-1$. The goal is to point out that this assumption may lead, in some cases, to a singular mass matrix. Let us characterize the submatrix $M_{ll}(q)$. In the case $N = 2$, $M_{ll}(q) = \begin{pmatrix} m_1+m_2 & m_2\cos(\theta_2) \\ m_2\cos(\theta_2) & m_2 \end{pmatrix}$, see (22). Clearly $m_1 \lll m_2$ and $\theta_2 \approx 0$ implies that $\det(M_{ll}(q)) \approx 0$. In general the entries of $M_{ll}(q)$ are given by (18). Taking $m_i = 0$ for all $1 \leq i \leq N-1$ yields $m_{(1+N+m)p}(q) = m_N \cos(\sum_{j=1}^{n}\theta_j - \sum_{j=1}^{p-N-1}\theta_j)$. Thus at the vertical posture all entries are equal to m_N so that $\text{rank}(M_{ll}) = 1$ and $\text{rank}(M(q)) = 2+N$. At the vertical posture it is also true that $M_{x\theta l} = 0$. The low-rank property means that there exist combinations of nonzero velocities $\dot{l}_i$ which produce no kinetic energy. They are obtained by moving the nodes in such a way that the payload does not move: the massless nodes move but do not contribute to the kinetic energy. Obviously this does not occur if the lengths are constant.

3.1.5 The potential energies

If no elastic torsional joint stiffness and no longitudinal deformation is modeled, this reduces to the gravity potential energy of each link, that of the trolley being constant chosen equal to zero.

$$U_g = -\sum_{i=1}^{N} m_i g \sum_{k=1}^{i} l_k \cos(\sum_{j=1}^{k}\theta_j) \tag{47}$$

Thus:

$$\begin{array}{ll} \frac{\partial U_g}{\partial \theta_n} & = -\frac{\partial}{\partial \theta_n}\sum_{i=1}^{N} m_i g \sum_{k=1}^{i} l_k \cos(\sum_{j=1}^{k}\theta_j) \\ & = -\sum_{i=n}^{N} m_i g \sum_{k=n}^{i} l_k \frac{\partial}{\partial \theta_n}\cos(\sum_{j=1}^{k}\theta_j) = \sum_{i=n}^{N} m_i g \sum_{k=n}^{i} l_k \sin(\sum_{j=1}^{k}\theta_j) \end{array} \tag{48}$$

so that for small angles $\frac{\partial U_g}{\partial \theta_n} = 0$ (the potential energy is almost constant), and for $m_N \ggg m_i$: $\frac{\partial U_g}{\partial \theta_n} = m_N g \sum_{k=1}^{N} l_k \sin(\sum_{k=1}^{M}\theta_k)$. And

$$\begin{array}{ll} \frac{\partial U_g}{\partial l_n} & = -\frac{\partial}{\partial l_n}\sum_{i=1}^{N} m_i g \sum_{k=1}^{i} l_k \cos(\sum_{j=1}^{k}\theta_j) \\ & = -\sum_{i=1}^{N} m_i g \frac{\partial}{\partial l_n}\sum_{k=1}^{i} l_k \cos(\sum_{j=1}^{k}\theta_j) = -\sum_{i=n}^{N} m_i g \frac{\partial}{\partial l_n}\sum_{k=n}^{i} l_k \cos(\sum_{j=1}^{k}\theta_j) \\ & = -\sum_{i=n}^{N} m_i g \cos(\sum_{j=1}^{n}\theta_j) \end{array} \tag{49}$$

For small angles $\frac{\partial U_g}{\partial l_n} = -\sum_{i=n}^{N} m_i g$. For $m_N \ggg m_i$ this gives $\frac{\partial U_g}{\partial l_n} = -m_N g$.

Remark 4 *In case $N = 1$ the general expression (48) gives: $\frac{\partial U_g}{\partial \theta_1} = m_1 g l_1 \sin(\theta_1)$ and from (49) for $N = 1$: $\frac{\partial U_g}{\partial l_1} = -m_1 g \cos(\theta_1)$.*

Joint flexibility: If joint flexibility is added at joints A_i, $1 \leq i \leq N$, in order to model some bending stiffness for the cable, then the additional potential energy is $U_{flex}(\theta) = \frac{1}{2}\sum_{j=0}^{N-1}\kappa_j\theta_{j+1}^2 = \frac{1}{2}\theta^\top \mathcal{K}\theta$, where $\kappa_j \geq 0$ is the angular stiffness at joint A_j and $\mathcal{K} = \mathrm{diag}(\kappa_i)$, $0 \leq i \leq N-1$. Thus:

$$\frac{\partial U_{flex}(\theta)}{\partial \theta_i} = \kappa_{i-1}\theta_i, \;\; 1 \leq i \leq N. \tag{50}$$

This introduces no couplings between the coordinates, contrarily to what occurs in flexible joint manipulators [Lozano and Brogliato, 1992, Brogliato et al., 1995, Tomei, 1991]. In the coordinate angles $\alpha_i = \sum_{j=1}^{i}\theta_j$, $1 \leq i \leq N$, $\alpha = J\theta$ with J in (36), $\theta = J^{-1}\alpha$ with J^{-1} in (36), hence $U_{flex}(\alpha) = \frac{1}{2}\theta^\top\mathcal{K}\theta = \frac{1}{2}\alpha^\top J^{-\top}\mathcal{K}J^{-1}\alpha$. In view of (36): $J^{-1}\alpha = \begin{pmatrix} \alpha_1 \\ \alpha_2 - \alpha_1 \\ \vdots \\ \alpha_N - \alpha_{N-1} \end{pmatrix}$, hence $U_{flex}(\alpha) = \frac{1}{2}\kappa_0\alpha_1^2 + \sum_{i=1}^{N-1}\kappa_i(\alpha_{i+1}-\alpha_i)^2$. It is inferred that

$$\frac{\partial U_{flex}(\alpha)}{\partial \alpha_1} = \kappa_0\alpha_1 - \kappa_1(\alpha_2 - \alpha_1) = (\kappa_0 + \kappa_1)\alpha_1 - \kappa_1\alpha_2, \tag{51}$$

for $2 \leq j \leq N-1$:

$$\frac{\partial U_{flex}(\alpha)}{\partial \alpha_j} = \kappa_{j-1}(\alpha_j - \alpha_{j-1}) - \kappa_j(\alpha_{j+1} - \alpha_j) = (\kappa_{j-1} + \kappa_j)\alpha_j - \kappa_j\alpha_{j+1} - \kappa_{j-1}\alpha_{j-1}, \tag{52}$$

and

$$\frac{\partial U_{flex}(\alpha)}{\partial \alpha_N} = \kappa_{N-1}(\alpha_N - \alpha_{N-1}), \tag{53}$$

so that

$$\frac{\partial U_{flex}(\alpha)}{\partial \alpha} = \begin{pmatrix} \kappa_0+\kappa_1 & -\kappa_1 & 0 & \dots & & & 0 \\ -\kappa_1 & \kappa_1+\kappa_2 & -\kappa_2 & 0 & \dots & & 0 \\ 0 & -\kappa_2 & \kappa_2+\kappa_3 & -\kappa_3 & 0 & \dots & 0 \\ \vdots & & & & & & \vdots \\ \vdots & & & & & & \vdots \\ 0 & \dots & & & 0 & -\kappa_{N-2} & \kappa_{N-2}+\kappa_{N-1} & -\kappa_{N-1} \\ 0 & \dots & & & & 0 & -\kappa_{N-1} & \kappa_{N-1} \end{pmatrix} \tag{54}$$

This time the joint flexibility introduces a triangular structure in the torques that derive from the elasticity potential, since the row $1+n$ of the Lagrange dynamics, $1 \leq n \leq N$, corresponding to $M_{(1+n)\bullet}(q_\alpha)$ and $\ddot{\alpha}_n$, contains the flexibility torque $(-\kappa_{n-1}\alpha_{n-1} + (\kappa_{n-1}+\kappa_n)\alpha_n) - \kappa_n\alpha_{n+1}$. One can think of using a backstepping-like control design using the fictitious input α_{n+1}. However, as seen in Lemma 1, the *vis-à-vis* terms in the submatrix $M_{\alpha\alpha}(q_\alpha)$ always contain strong inertial couplings between $\ddot{\alpha}_n$ and the other angular accelerations. Therefore the global triangular structure of Spong's model for flexible-joint manipulators [Lozano and Brogliato, 1992, Brogliato et al., 1995] does not exist in such overhead crane systems.

Links with Linear Longitudinal Elasticity (2D Operating Space): The same system is considered as in Figure 3, with elastic links to approximate extensible cables. This is depicted in Figure 4. In this case necessarily $q = (x, \theta_1, \dots, \theta_N, l_1, \dots, l_N)^\top$. Each link has a longitudinal linear elasticity with stiffness $k_i > 0$, $1 \leq i \leq N$. Damping can also be modeled, see [Gueners et al., 2021] for details on Kelvin-Voigt model parameters estimation. The same framework as in the foregoing sections is adopted, but the potential energy is augmented with terms $\frac{1}{2}k_i(l_i - l_{i,r})^2$ (assuming that springs are at rest for $l_i = l_{i,r}$). This model is close in spirit to the lumped-mass models developed in [Caverly et al., 2014, Khalilpour et al., 2021], but nonlinearities are considered here. It is also easy to add some viscous friction (linear spring-dashpot or Kelin-Voigt model) $c_i\dot{l}_i$, which is some kind of Rayleigh dissipation [Brogliato et al., 2020, Definition 6.12]. Remind that $l = (l_1, l_2, \dots, l_N)^\top$, one has (compare with (44)):

$$\frac{\partial U_{elas}}{\partial l} = (k_1(l_1 - l_{1,r}), \dots, k_N(l_N - l_{N,r}))^\top \tag{55}$$

3.1.6 Lagrange dynamics

Let us use $q = (x, \theta_1, \dots, \theta_N, l_1, \dots, l_N)^\top$. The Lagrange dynamics of the overhead crane is given by:

$$\frac{d}{dt}\frac{\partial(T_{trol} + T_{trans} - U_g)}{\partial \dot{q}} - \frac{\partial(T_{trol} + T_{trans} - U_g - U_{flex})}{\partial q} = Q, \tag{56}$$

where Q_i works on q_i. More precisely:

$$\begin{cases} \frac{d}{dt}\frac{\partial(T_{trol}+T_{trans})}{\partial \dot{x}} = Q_x = F \\ \frac{d}{dt}\frac{\partial T_{trans}}{\partial \dot{\theta}} - \frac{\partial(T_{trans}-U_g-U_{flex})}{\partial \theta} = Q_\theta = 0 \\ \frac{d}{dt}\frac{\partial T_{trans}}{\partial \dot{l}} - \frac{\partial(T_{trans}-U_g-U_{flex})}{\partial l} = Q_l = (F_1, 0, \dots, 0)^\top \end{cases} \tag{57}$$

It may be useful to introduce viscous friction (Rayleigh dissipation [Brogliato et al., 2020, Definition 6.12]) at the joints. This may allow to avoid chaotic behaviours of conservative pendula. Such dynamical behaviour is unlikely to occur in real cables where a small amount of dissipation and of bending stiffness is always present. The generalized force $F = u + d$ encompasses the trolley's control $u(t)$ as well as disturbances or tangential effects $d(t)$ between the trolley and its rail guide (friction). The actuator which deliver $u(t)$ may be modelled as an additional dynamics [Brogliato et al., 2020, Sections 6.6.1, 6.6.2]. When links longitudinal flexibilities are considered as in (55), then (57) is changed to:

$$\begin{cases} (a) \ \frac{d}{dt}\frac{\partial(T_{trol}+T_{trans})}{\partial \dot{x}} = Q_x = F \\ (b) \ \frac{d}{dt}\frac{\partial T_{trans}}{\partial \dot{\theta}} - \frac{\partial(T_{trans}-U_g-U_{flex})}{\partial \theta} + C_\theta \dot{\theta} = Q_\theta = 0 \\ (c) \ \frac{d}{dt}\frac{\partial T_{trans}}{\partial \dot{l}} - \frac{\partial(T_{trans}-U_g-U_{flex}-U_{elas})}{\partial l} + C_l \dot{l} = Q_l = (F_1, 0, \ldots, 0)^\top \end{cases} \tag{58}$$

with $C_l = \mathrm{diag}(c_i)$, the form of $C_\theta \succcurlyeq 0$ depends on the choice of the coordinates.

The overhead crane dynamics and control may be seen as an extension of the linear chains dynamics and control [Ovseevich and Ananievski, 2021, Ovseevich and Fedorov, 2015]: it is a nonlinear chain that is much more complex than its linear counterpart, where (58) (a) and (b) are absent.

3.2 Some properties useful for controlpurpose

3.2.1 Spong's coordinates partition

Let us further split the matrix $M_{x\theta l}(q) = \begin{pmatrix} M_{xl}(q) \\ M_{\theta l}(q) \end{pmatrix}$, so that:

$$M(q) = \begin{pmatrix} M_{xx} & \bar{M}_{x\theta} & M_{xl} \\ \bar{M}_{x\theta}^\top & M_{\theta\theta} & M_{\theta l} \\ M_{xl}^\top & M_{\theta l}^\top & M_{ll} \end{pmatrix} \tag{59}$$

Item 1 in Lemma 2 allows us to perform Spong's transformation for actuated and unactuated coordinates [Reyhanoglu et al., 1999]. Indeed $\ddot{\theta} = M_{\theta\theta}^{-1}(-\bar{M}_{x\theta}^\top \ddot{x} - M_{\theta l}\ddot{l}_1 - NL_\theta(q,\dot{q}))$, hence:

$$\underbrace{(M_{xx} - \bar{M}_{x\theta}M_{\theta\theta}^{-1}\bar{M}_{x\theta}^\top)}_{\triangleq \mathcal{M}_x}\ddot{x} + \underbrace{(M_{xl} - \bar{M}_{x\theta}M_{\theta\theta}^{-1}M_{\theta l})}_{\triangleq \mathcal{M}_{xl_1}}\ddot{l}_1 - \bar{M}_{x\theta}M_{\theta\theta}^{-1}NL_\theta(q,\dot{q}) + NL_x(q,\dot{q}) = F \tag{60}$$

and

$$(M_{xl}^\top - M_{\theta l}^\top M_{\theta\theta}^{-1}\bar{M}_{x\theta}^\top)\ddot{x} + \underbrace{(M_{ll} - M_{\theta l}^\top M_{\theta\theta}^{-1}M_{\theta l})}_{\triangleq \mathcal{M}_{l_1}}\ddot{l}_1 - M_{\theta l}^\top M_{\theta\theta}^{-1}NL_\theta(q,\dot{q}) + NL_{l_1}(q,\dot{q}) = F_1 \tag{61}$$

where $\mathcal{M}_x \succ 0$ and $\mathcal{M}_{l_1} \succ 0$ from the Schur complement Theorem. Rearranging the matrix in (59) and applying again the Schur complement Theorem, it follows that:

Lemma 3 *Let us consider (60) (61), then:*

$$\mathcal{M}(q) \triangleq \begin{pmatrix} \mathcal{M}_x(q) & \mathcal{M}_{xl_1}(q) \\ \mathcal{M}_{xl_1}^\top(q) & \mathcal{M}_{l_1}(q) \end{pmatrix} = \mathcal{M}^\top(q) \succ 0 \tag{62}$$

Consequently the system in (60) (61) with state $(x, \dot{x}, l_1, \dot{l}_1)^\top$ is controllable, linearizable by state feedback. Then the crucial point concerns the integrability properties of the system of unactuated coordinates [Reyhanoglu et al., 1999]:

$$\ddot{\theta} = M_{\theta\theta}^{-1}(-\bar{M}_{x\theta}^\top \ddot{x} - M_{\theta l}\ddot{l}_1 - NL_\theta(q, \dot{q})) \tag{63}$$

Usually such dynamics are nonintegrable and thus can be interpreted as second-order nonholonomic constraints, which do not reduce the state-space dimension [Reyhanoglu et al., 1999]. From Lemma 2 the term $M_{\theta l}(q)$ vanishes at the vertical cable's posture and is proportional to θ_i and sums of angles in a neighborhood of it. Thus around the vertical posture only $\bar{M}_{x\theta}^\top \ddot{x}$ remains available as a control input to this subdynamics, and some control action may also exist thanks to $NL_\theta(q, \dot{q})$. Said otherwise:

Proposition 2 *Let $q = (x, \theta_1, \ldots, \theta_N, l_1)^\top$, with all links' lengths from l_2 to l_n being constant. The only way to control the θ dynamics (63) in the neighborhood of the cable's vertical posture, is through $\ddot{x}$ and/or some velocity couplings in the nonlinearities $NL_\theta(q, \dot{q})$, as visible in (24).*

Let us now investigate in more details these nonlinearities. Let us take a close look at (24), for $n = N$:

$$\begin{aligned}
\tfrac{d}{dt}\tfrac{\partial T_{trans}}{\partial \dot{\theta}_N} &= m_N \Big(\ddot{x} + 2\dot{l}_1\dot{\theta}_1 \cos(\theta_1) + \ddot{l}_1 \sin(\theta_1) + \textstyle\sum_{k=1}^N l_k \Big(\sum_{j=1}^k \ddot{\theta}_j \Big) \cos(\sum_{j=1}^k \theta_j) \\
&\quad - \textstyle\sum_{k=1}^N l_k \Big(\sum_{j=1}^k \dot{\theta}_j \Big)^2 \sin(\sum_{j=1}^k \theta_j) \Big) l_N \cos(\textstyle\sum_{j=1}^N \theta_j) \\
&\quad + m_N \Big(\dot{x} + \dot{l}_1 \sin(\theta_1) + \textstyle\sum_{k=1}^N l_k \Big(\sum_{j=1}^k \dot{\theta}_j \Big) \cos(\sum_{j=1}^k \theta_j \Big)) \\
&\quad \times \left(-l_N (\textstyle\sum_{j=1}^N \dot{\theta}_j) \sin(\sum_{j=1}^N \theta_j) + \left\{ \begin{array}{lll} \dot{l}_1 \cos(\theta_1) & \text{if} & N = 1 \\ 0 & \text{if} & N \geq 2 \end{array} \right. \right) \\
&\quad + m_N \Big(2\dot{l}_1\dot{\theta}_1 \sin(\theta_1) - \ddot{l}_1 \cos(\theta_1) + \textstyle\sum_{k=1}^N l_k \Big(\sum_{j=1}^k \dot{\theta}_j \Big)^2 \cos(\sum_{j=1}^k \theta_j) \\
&\quad + l_k \Big(\textstyle\sum_{j=1}^k \ddot{\theta}_j \Big) \sin(\sum_{j=1}^k \theta_j) \Big) l_N \sin(\textstyle\sum_{j=1}^N \theta_j) \\
&\quad + m_N \Big(-\dot{l}_1 \cos(\theta_1) + \textstyle\sum_{k=1}^N l_k \Big(\sum_{j=1}^k \dot{\theta}_j \Big) \sin(\sum_{j=1}^k \theta_j) \Big) \\
&\quad \times \left(l_N (\textstyle\sum_{j=1}^N \dot{\theta}_j) \cos(\sum_{j=1}^N \theta_j) + \left\{ \begin{array}{lll} \dot{l}_1 \sin(\theta_1) & \text{if} & N = 1 \\ 0 & \text{if} & N \geq 2 \end{array} \right. \right)
\end{aligned} \tag{64}$$

It can also be calculated that

$$\begin{aligned}
\tfrac{\partial T_{trans}}{\partial \theta_n} &= \textstyle\sum_{i=n}^N m_i \Big(\dot{x} + \sum_{k=1}^i l_k \Big(\sum_{j=1}^k \dot{\theta}_j \Big) \cos \Big(\sum_{j=1}^k \theta_j \Big) + \dot{l}_k \sin(\sum_{j=1}^k \theta_j) \Big) \\
&\quad \times \Big(\textstyle\sum_{k=n}^i -l_k \Big(\sum_{j=1}^k \dot{\theta}_j \Big) \sin \Big(\sum_{j=1}^k \theta_j \Big) + \dot{l}_k \cos(\sum_{j=1}^k \theta_j) \Big) \\
&\quad + \textstyle\sum_{i=n}^N m_i \Big(\sum_{k=1}^i l_k \Big(\sum_{j=1}^k \dot{\theta}_j \Big) \sin \Big(\sum_{j=1}^k \theta_j \Big) - \dot{l}_k \cos(\sum_{j=1}^k \theta_j) \Big) \\
&\quad \times \Big(\textstyle\sum_{k=n}^i l_k \Big(\sum_{j=1}^k \dot{\theta}_j \Big) \cos \Big(\sum_{j=1}^k \theta_j \Big) + \dot{l}_k \sin(\sum_{j=1}^k \theta_j) \Big)
\end{aligned} \tag{65}$$

Hence for $n = N$ it follows that:

$$\begin{array}{ll} \frac{\partial T_{trans}}{\partial \theta_n} & = m_N \left(\dot{x} + \sum_{k=1}^{N} l_k \left(\sum_{j=1}^{k} \dot{\theta}_j\right) \cos(\sum_{j=1}^{k} \theta_j) + \dot{l}_1 \sin(\theta_1)\right) \\ & \times \left(-l_N \left(\sum_{j=1}^{N} \dot{\theta}_j\right) \sin(\sum_{j=1}^{N} \theta_j) + \left\{ \begin{array}{lll} \dot{l}_1 \cos(\theta_1) & \text{if} & N = 1 \\ 0 & \text{if} & N \geq 2 \end{array} \right. \right) \\ & + m_N \left(\sum_{k=1}^{N} l_k \left(\sum_{j=1}^{k} \dot{\theta}_j\right) \sin(\sum_{j=1}^{k} \theta_j) - \dot{l}_1 \cos(\theta_1)\right) \\ & \times \left(l_N \left(\sum_{j=1}^{N} \dot{\theta}_j\right) \cos(\sum_{j=1}^{N} \theta_j) + \left\{ \begin{array}{lll} \dot{l}_1 \sin(\theta_1) & \text{if} & N = 1 \\ 0 & \text{if} & N \geq 2 \end{array} \right. \right) \end{array} \tag{66}$$

These two expressions allows us to calculate the Coriolis/centrifugal velocity quadratic couplings in the Lagrange dynamics row $\frac{d}{dt}\frac{\partial T_{trans}}{\partial \dot{\theta}_N} - \frac{\partial T_{trans}}{\partial \theta_N}$. The terms involving $\dot{l}_1$ are:

$$\begin{array}{l} 2m_N \dot{l}_1 l_N \dot{\theta}_1 \cos(\theta_1) \cos(\sum_{j=1}^{N} \theta_j) + m_N \dot{l}_1 \sin(\theta_1) \left(-l_N (\sum_{j=1}^{N} \dot{\theta}_j) \sin(\sum_{j=1}^{N} \theta_j) + \left\{ \begin{array}{lll} \dot{l}_1 \cos(\theta_1) & \text{if} & N = 1 \\ 0 & \text{if} & N \geq 2 \end{array} \right. \right) \\ + 2m_N \dot{l}_1 l_N \dot{\theta}_1 \sin(\theta_1) \sin(\sum_{j=1}^{N} \theta_j) - m_N \dot{l}_1 \cos(\theta_1) \left(l_N (\sum_{j=1}^{N} \dot{\theta}_j) \cos(\sum_{j=1}^{N} \theta_j) + \left\{ \begin{array}{lll} \dot{l}_1 \sin(\theta_1) & \text{if} & N = 1 \\ 0 & \text{if} & N \geq 2 \end{array} \right. \right) \\ - m_N \dot{l}_1 l_N \sin(\theta_1) \left(\sum_{j=1}^{N} \dot{\theta}_j\right) \sin(\sum_{j=1}^{N} \theta_j) - m_N \dot{l}_1 l_N \cos(\theta_1) \left(\sum_{j=1}^{N} \dot{\theta}_j\right) \cos(\sum_{j=1}^{N} \theta_j) \end{array} \tag{67}$$

The terms involving $\dot{x}$ vanish. For $N = 1$, equation (67) boils down to:

$$\begin{array}{l} 2m_1 \dot{l}_1 l_1 \dot{\theta}_1 \cos^2(\theta_1) + m_1 \dot{l}_1 \sin(\theta_1) \left(-l_1 \dot{\theta}_1 \sin(\theta_1) + \dot{l}_1 \cos(\theta_1)\right) + 2m_1 \dot{l}_1 l_1 \dot{\theta}_1 \sin^2(\theta_1) \\ - m_1 \dot{l}_1 \cos(\theta_1) \left(l_1 \dot{\theta}_1 \cos(\theta_1) + \dot{l}_1 \sin(\theta_1)\right) - m_1 \dot{l}_1 l_1 \sin^2(\theta_1) \dot{\theta}_1 - m_1 \dot{l}_1 l_1 \cos^2(\theta_1) \dot{\theta}_1 = 2m_1 \dot{l}_1 l_1 \dot{\theta}_1. \end{array} \tag{68}$$

For $N \geq 2$:

$$\begin{array}{l} 2m_N \dot{l}_1 l_N \dot{\theta}_1 (\cos(\theta_1) \cos(\sum_{j=1}^{N} \theta_j) + \sin(\theta_1) \sin(\sum_{j=1}^{N} \theta_j)) \\ - 2m_N \dot{l}_1 l_N \left(\sum_{j=1}^{N} \dot{\theta}_j\right) (\cos(\theta_1) \cos(\sum_{j=1}^{N} \theta_j) + \sin(\theta_1) \sin(\sum_{j=1}^{N} \theta_j)) \\ = 2m_N \dot{l}_1 l_N \left(\dot{\theta}_1 \cos(\sum_{j=2}^{N} \theta_j) - \left(\sum_{j=1}^{N} \dot{\theta}_j\right) \cos(\sum_{j=2}^{N} \theta_j)\right) \\ = -2m_N \dot{l}_1 l_N \left(\sum_{j=2}^{N} \dot{\theta}_j\right) \cos(\sum_{j=2}^{N} \theta_j) \end{array} \tag{69}$$

Lemma 4 *Let $q = (x, \theta_1, \ldots, \theta_N, l_1)^\top$, with all links' lengths from l_2 to l_n being constant. The Coriolis/centrifugal velocity couplings in the Lagrange dynamics, corresponding to the θ_N dynamics (the row $M_{(N+1)\bullet}(q)$), and involving $\dot{l}_1$ in the vector $(C(q,\dot{q})\dot{q})_{1+N}$, are given by:*

$$2m_1 \dot{l}_1 l_1 \dot{\theta}_1, \tag{70}$$

for $N = 1$, and

$$- 2m_N \dot{l}_1 l_N (\sum_{j=2}^{N} \dot{\theta}_j) \cos(\sum_{j=2}^{N} \theta_j) \tag{71}$$

for $N \geq 2$.

Clearly quadratic terms in velocities $\dot{\theta}_i$ are present in the nonlinearities also.

3.3 Zero-dynamics

Zero-dynamics and the relative degree are essential characteristics of controlled systems, and for the existence and the analysis of their normal form. Considering the inputs as the generalized forces F and F_1, the zero-dynamics of Lagrangian systems obviously depend on the output. If the output is the passive output, then the vector relative degree is equal to $(1,\dots,1)^\top$, and the zero dynamics possess some stability properties, provided that the storage function are positive definite [Brogliato et al., 2020]. However the passive output for the overhead crane system are the collocated velocities $\dot{x}$ and $\dot{l}_1$. Even if in practice one may replace these by x and l_1 and perform some differentiation (which anyway introduces some additional dynamics), it is possible that other outputs are available only, or that the controller is designed with noncollocated (hence *a priori* nonpassive) outputs, with possibly higher relative degree. The explicit determination of the normal form and of the zero-dynamics for Lagrangian systems, is usually a hard task [Brogliato and Tanwani, 2020, section 4.2.1] and [Lanza, 2021].

3.3.1 Passive outputs (collocated feedback control)

The zero-dynamics may be stable but not asymptotically stable. In this case zero-state detectability (ZSD) and output feedback may be used to get the asymptotic stability of the closed-loop system [Brogliato et al., 2020, Theorem 5.35] [Byrnes et al., 1991]. As seen in section 2.4, Property 1 permits to state that the total energy derivative satisfies along the system's trajectories: $\dot{T}_{total}(t) = \dot{x}F + \dot{l}_1 F_1$. If in addition T_{total} is a positive semidefinite function (a property mainly related to the potential energy form), then the dynamics is passive in Willems' sense [Brogliato et al., 2020, Definition 4.21]. Clearly a PD input $F = -k_{p,x}(x-x_d)-k_{v,x}\dot{x}$ and $F_1 = -k_{p,l_1}(l_1-l_{1,d})-k_{v,l_1}\dot{l}_1$ shapes the potential energy with the additive term $U_{PD} = \frac{1}{2}k_{p,x}x^2+\frac{1}{2}k_{p,l_1}l_1^2$. Then it is possible to show that $\dot{T}_{total} = -k_{v,x}\dot{x}^2 - k_{v,l_1}\dot{l}_1^2 \leq 0$. This is equivalent to applying a static output feedback $\Phi(\dot{x},\dot{l}_1)$ satisfying $(\dot{x},\dot{l}_1)^\top\Phi(\dot{x},\dot{l}_1) = k_{v,x}\dot{x}^2 + k_{v,l_1}\dot{l}_1^2 > 0$ for all $(\dot{x},\dot{l}_1) \neq (0.0)$ to the augmented system. It remains to check that the system is ZSD, *i.e.*, does $F(t) = 0$, $F_1(t) = 0$, $\dot{x}(t) = 0$, $\dot{l}_1(t) = 0$ for all $t \geq 0$, imply that the whole state $(q,\dot{q})$ vanishes asymptotically. This method has certainly been employed in several papers using the passivity-based approach using 1 or 2 dof pendulum. However, it is not clear yet how to extend this to the N dof case. In other words, the ZSD property of the general N-link pendulum system should be studied.

Roughly speaking, the asymptotic stability is attained in the case that the couplings between the trolley and link 1 dynamics, and the remaining part of the cable's dynamics, are such that if the cable is not at rest, then the trolley and link 1 cannot be at rest. This may however not be optimal from the point of view of stabilization speed.

Remark 5 *If the cable links have longitudinal stiffness and varying lengths l_i, but there is no control F_1 and only the trolley is controlled, then ZSD holds only if natural damping is present in the links in addition*

to the stiffness. Indeed when in the vertical posture, the cable can oscillate without acting on the trolley. It is inferred that extensible cables need an additional input for stabilization. If the longitudinal motion is neglected because the cable is extremely stiff, then the above reasoning holds with $\dot{x}$ and F.

3.3.2 Study the Lasalle's invariance principle for multiple-pendulum system

Considering again the general form of a multiple-pendulum system on a cart as $M(q)\ddot{q}+C(q,\dot{q})\dot{q}+g(q)=Q$, it is straightforward to show that the map between the input force applied to the trolley F and the trolley velocity is passive, *i.e.*, $\dot{E}=\dot{x}F$ where $E=\frac{1}{2}\dot{q}^{\intercal}M(q)\dot{q}+g\sum_{i=1}^{N}l_i(1-\cos(\theta_i))\sum_{i=1}^{N-i+1}m_{j+i-1}$. Considering a PD controller $F=-\dot{x}$, according to the Lyapunov theorem, the state variable x is asymptotically stable. However, as can be seen, the Lyapunov theorem doesn't say anything about the internal dynamics since its time derivative is just negative semi definite. To study the stability of other state variables, ZSD has to be investigated. Unfortunately, investigation of ZSD for a general case with arbitrary N seems not to be straightforward enough. So far, the ZSD has just been ensured for $N=1,2$ in the literature.

3.3.3 Payload position and velocity, sway angles as outputs (noncollocated feedback)

The drawback of the "naturally" passive outputs is that they yield a feedback that may not damp the cable's oscillations fast enough. It is then of interest to investigate other solutions, still using passivity, but with different supply rates, using other outputs defined from the payload position and velocity.

3.3.4 Adding control inputs

The classical control inputs in overhead cranes, are the forces F_x (2D operating space) and F_z (3D operating space) exerted on the trolley. A torque representing a possible winding control acting on θ_1 is introduced above. Motivated by studies on suspended cables control (see section 3.6.2), let us add to the system a force input F_i at node A_i. This force works on A_i displacement (x_i,y_i), *i.e.*, $\delta W_i=F_i^{\top}(\delta x_i,\delta y_i)$ (this is trivially extended to 3D operating space).

Another input can be represented by a torque working on the rotational degree of freedom of the trolley along the (A_0,y) axis. Then it is necessary to introduce the torsional stiffness of the cable. If the cable is in the vertical posture, and a torsional spring is associated with each link, the payload rotation control is equivalent to the control of a linear chain of oscillators [Ovseevich and Fedorov, 2015, Ovseevich and Ananievski, 2021].

3.4 Lumped-mass models: the trolley-pendulum Lagrange dynamics in 3D operating space

Some dynamic effects cannot be handled with a 2D operating space model, because they are intrinsically three dimensional. Hence, modeling in the 3D space seems to be mandatory.

3.4.1 3D pendulum models

In a 3D operating space, the pendulum is made of N links with spherical (or ball) joints, while the trolley moves in a plane. The system with fixed links' lengths has $2N + 2$ degrees of freedom, when links have varying lengths it has $3N + 2$ dofs. It is expected, in view of the developments in sections 3.1 and 3.2, that 3D Lagrange dynamics are quite complex and cumbersome to analyze in their full generality. The kinetic energy is the sum of the translational kinetic energies of the links centers of mass, and of the rotational kinetic energies of each link. If we assume as for the 2D case that the masses are lumped at the joints, we may see the system as a system of constrained particles (since in this case the inertia operator of each link, calculated at the center of mass, vanishes). The simplest case $N = 1$ yields with varying link's length a 5×5 mass matrix, while the 2-link pendulum has an 8×8 mass matrix. Calculations reported in [Ouyang et al., 2021, Appendix A] for $N = 2$ and fixed lengths show that the submatrix $M_{x\theta}(q)$ has interesting properties with inertially decoupled coordinates, hence Lemma 1 has to be adapted. The last link may be replaced by a payload with axial flexibility, and unbalanced payload with 3D dynamics, in order to take into account the motion of the payload itself, see section 3.4.3. Single-link pendulum models with possible varying lengths are presented in detail in [Abdel-Rahman et al., 2003] and appear to be strongly nonlinear. The models developed in (43) (46) and (79) adapt to the 3D case by considering particles in a 3D Cartesian frame. However the nonlinearities present in the stiffness generalized forces become more complex, and it is unclear if these dynamics bring significant advantage for Control.

3.4.2 Necessity of 3D models

As alluded to above, 3D dynamics may be necessary in applications to model:

- intrinsically 3D dynamical effects in pendula, studied by the Nonlinear Dynamics scientific community for the 1-link pendulum [Abdel-Rahman et al., 2003],
- 3D motion of the payload, usually called "skew" motion but which deserves more detailed analysis, see Section 3.4.3.

3.4.3 3D payload angular motions

The term “sway” that is largely employed in the literature, may refer to several types of oscillations. The oscillations of the payload along x and y axes for the pendulum-like model refers to a special sway which is called swing or pendulation oscillations. In addition to swing, oscillations of the payload around its axes produce other types of oscillations with respect to the three axes which are called “skew”, “trim” and “list” as shown in Fig. 5. Note that these angles are different from Euler or Bryan angles since they are studied and handled separately. Unlike the swing, skew, trim and list rotations only occurs in 3D space, and efficient control of skew may require modeling in 3D space.

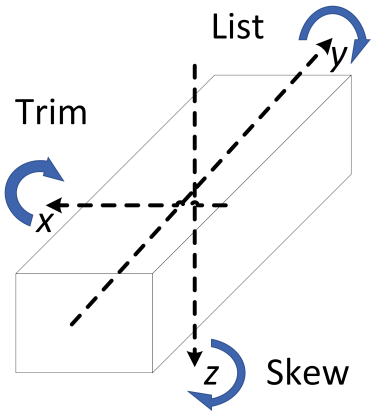

Figure 5: Other types of payload sway (very small rotations)

Some skew control methods require additional actuators on the hoisting cable. [Ngo et al., 2008, Klaassens et al., 1999] assume that the payload is suspended by four cables which can be adjusted separately by four actuators.

3.4.4 Literature review for the 3D space

Considering the cranes in 3D space, the literature should be studied under two different aspects, *i.e.*, *modeling* and *control*. Compared to the 2D models, few references have developed the 3D models for overhead cranes, due to the complexity of obtaining the Lagrange dynamics in their full generality as done in Section 3.1 for the 2D case. Regarding the modeling, the literature can be divided into the following categories:

- **Lumped mass 3D model for single-pendulum system**: In this category, the cart and the payload, and possibly the hook (if any) are assumed to be lumped masses and the cable is massless. This kind of model has been developed by [Maghsoudi et al., 2017, Toxqui et al., 2006, Garrido et al., 2008, Knierim et al., 2010, Lee et al., 2013, Maghsoudi et al., 2016, Tuan et al., 2014, 2012] were the inputs are forces applied to the trolley in x and y axes as well as the force applied to the winch. The state variables are the trolley position in x and y axes, the length of the cable, and the sway angles toward x and y axes. A similar model has been developed in [Wu and He, 2017, Yoshida and Tabata, 2008, Chwa, 2009, Ebeid et al., 1992, Sun et al., 2013, Wu and He, 2016, Chwa, 2017, Vázquez et al., 2014] with this difference that the force applied to the winch is ignored. As the result the cable is assumed to have a fixed length. The same model with the wind disturbance is also developed in [Abdullahi et al., 2018]. It should be noted that such lumped mass models does not allow studying the *trim* and *skew* rotations (see Fig. 5) because of lumped masses. In addition, some studies have also considered skew control problem on the lumped mass models [Chwa, 2017]. However, The definition of skew angle, in such references, is different from the one which has been shown in Fig. 5.

- **Distributed mass 3D model**: At least one distributed mass is considered in the modeling. The

models in this category allow to study the *trim* and *skew* rotations (see Fig. 5). Note that, in this category, it is usually assumed that the payload is connected to the trolley trough multiple cables rather than only one approximated cable. These cable could be considered either as rigid [Morrish et al., 1997, Cartmell et al., 1996, Klaassens et al., 1999] or flexible links [Morrish et al., 1996, Arena et al., 2013, Cartmell et al., 1996, Arena et al., 2015]. The kinematic of the multi cable cranes have been addressed in these references.

The control of overhead cranes in 3D space has also been studied from different point of views. First of all, it should be noted that there is a research gap in the literature concerning the control of multi cable cranes in 3D space[1]. The authors believe that the control methods developed for the cable-driven robots [Wei et al., 2017] can be employed to control multi-cable cranes based on the kinematics developed by [Morrish et al., 1997, Cartmell et al., 1996, Morrish et al., 1996, Arena et al., 2013, Cartmell et al., 1996, Arena et al., 2015, Klaassens et al., 1999]. The studies considering the control of lumped models in 3D space are as follows:

- **Decentralized control**: In this methods, the linearized model around an stable equilibrium point is used to design the controller. Under such condition, the coupling among the axes is eliminated and controllers can be designed for each axis independently, without taking the coupling into account. In this case, the controllers that designed for the 2D space, can be used to control each channel, separately. Some of the studies in this category is as follows [Toxqui et al., 2006, Garrido et al., 2008, Yoshida and Tabata, 2008, Ebeid et al., 1992]. [Maghsoudi et al., 2016] has designed a PID controller to control one axis of a crane modeled in 3D space. The PID controller is tuned using the PSO algorithm to show the best possible payload positioning. [Maghsoudi et al., 2017] has designed an input-shaping control for one axis of a crane. Similarly, PSO algorithm is used to tune the parameters of the shaper. To handle the coupling effect, in at least one study, each controller has been designed independently for each channel and the coupling is considered as a disturbance. For instance, [Vázquez et al., 2014] developed a super-twisting controller while the coupling is considered as disturbance.

- **Control design considering the coupling**: In this category, the controllers are designed based on the nonlinear model of the system and the coupling among the axes has been taken into account in the control design. In this method, the controllers are usually designed based on a Lyapunov function containing the variables corresponding to all axes in order to derive a centralized control rule [Wu and He, 2017]. Partial feedback linearization has been also employed in this category to take the coupling into account [Tuan et al., 2012, 2014, Lee et al., 2013, Sun et al., 2013, Chwa, 2009] and [Wu and He, 2016]. While a centralized control law can be obtained based on these procedures to handle the coupling, the stability is usually ensured locally [Tuan et al., 2012, 2014, Lee et al., 2013]. SMC is another approach in this category in order to handle the coupling [Chwa, 2017]. Flatness control also

[1]It should be noted that some references [Klaassens et al., 1999] proposed basic linear control schemes for the multi-cable cranes ignoring the coupling among the control channels.

automatically lead to a centralized control law [Knierim et al., 2010] in 3D space.

One topic still seems to be unaddressed. In fact, in the literature, the forces applied to the trolley toward the x and y axes as well as the force on the hosting mechanism are the only accessible control inputs. While these inputs might be sufficient for the payload positioning toward the x and y axes, they cannot be used to control the rotation of the payload (see fig. 5). The reason is that the lengths of the cables are always equal and there is not any freedom to change the cables' lengths independently. However, even for the equal cables' lengths, The works just addressed the kinematic problem without taking the control design into account [Morrish et al., 1997, Cartmell et al., 1996, Morrish et al., 1996, Arena et al., 2013, Cartmell et al., 1996, Arena et al., 2015]. In this context, the methods developed for the cable-driven robotic systems [Wei et al., 2017] may be useful to control the payload rotation in 3D space based on the kinematic developed in the above-mentioned references.

According to the discussion above, in summary, different control methods developed for cranes in 3D space are reviewed in Section 3.4.4, and it was mentioned that a portion of these methods are to handle the coupling effect in 3D space. In summary, the control methods developed for cranes with lumped masses in 3D space to handle the coupling are as follows:

- Methods developed by defining a Lyapunov function containing the error variables corresponding to two axes.
- Methods designed based on the partial feedback linearization.
- Methods developed based on the flatness theory.
- Methods derived by adding some extra terms to the previous methods developed for 2D space.
- Methods developed based on the SMC to reject the coupling as a disturbance.

3.5 Distributed-mass models: the trolley-flexible cables dynamics

As is well-known, cables can be also modelled as deformable, infinite-dimensional slender bodies Lv et al. [2020]. The trolley's dynamics imposes to consider ODE-PDE couplings. Interested readers are encouraged to the work by [Rauscher and Sawodny, 2021] where the possible sources of flexibility in cranes have been studied and modeled based on PDEs. In this case, Ritz method is employed to obtain a finite-dimensional equations corresponding to the PDEs (see [Meirovitch, 2010]). Let us first review the infinite-dimensional models to describe this infinite-dimensional systems.

3.5.1 The wave equation model with a fixed length

A first class of such models consists of the so-called wave or string dynamics, which are linear PDEs valid in a neighborhood of the cable's vertical posture. To derive this dynamical model, following e.g. [Reeken,

1977] and [Egeland and Gravdahl, 2002, 9.3.1], we denote s the curvilinear abscissa and $W(s,t)$ the position at time t of the point whose curvilinear abscissa is s (see Fig. 6). Let $\tau(s,t)$ be the tension along the cable and ρ be the lineic mass of the cable. Then, following [Reeken, 1977, d'Andrea Novel et al., 1991, d'Andréa Novel et al., 1994], we have the following dynamics:

$$\rho\ddot{W}(s,t) = \rho g + (\tau(s,t)W_s)_s \tag{72}$$

here W_s denotes the derivative of W with respect to s. The non-stretching assumption gives:

$$W_s(s,t)^2 = 1 \tag{73}$$

Let us note that the equilibrium should satisfy

$$\begin{array}{rcl} W_{ref} & = & se_y \\ \tau_{ref} & = & (m+s\rho)g \end{array} \tag{74}$$

where e_y denotes the unit vertical vector. Let us denote w and δ the deviation of x and of τ with respect to respectively x_{ref} and τ_{ref}. Replacing W and τ in (72) and (73), keeping only first order terms and projecting upon the horizontal e_x axis, we obtain the following system (see [d'Andréa Novel et al., 1994]):

$$\begin{array}{c} \ddot{w} - (aw_s)_s = 0 \\ w_s(L,t) = 0 \\ w(0,t) = x(t) \end{array} \tag{75}$$

where x is the position of the trolley,

$$a(s) = g\left(\frac{m}{\rho} + s\right)$$

and where the first boundary condition follows from the verticality of the cable at the free end, and the second boundary condition is the attached end to the trolley. As far as the trolley dynamics are concerned, we have

$$m\ddot{x} = \frac{(M+\rho L)g}{a(0)}(aw_s)(0,t) + u \tag{76}$$

where u is the force applied to the trolley, m is the mass of the trolley, M is the mass of the payload, and the smallness assumption of the angles has been used. The total kinetic energy is then computed as

$$T = \frac{1}{2}m\dot{x}^2(t) + \frac{1}{2}\int_0^L \rho\big(\dot{x}(t) + \dot{w}(y,t)\big)^2\, ds + \frac{1}{2}M\big(\dot{x}(t) + \dot{w}(L,t)\big)^2 \tag{77}$$

whereas the potential energy is written as

$$U = \frac{1}{2}\int_0^L aw_s^2\, ds \tag{78}$$

See also [Alli and Singh, 1998] for another derivation of these energies.

The reference [Shen and Caverly, 2020] has also considered the flexibility of the cable when the length of the cable is variable. Following this reference, the elongation of the cable at any point between the winch and the payload is given by $d(x,t) = \Psi(x, l_i(t))q^e(t)$ for all $x \in [L - l_i(t), L]$, where $l_i(t)$ is the cable's length at time t, L is the total length of the cable without winding, q^e is the vector of elastic coordinates. The basis function is selected as $\Psi(x, l_i) = [\sin\bar{x},\ \sin 2\bar{x},\ \sin 3\bar{x},\ \dots]$, where $\bar{x} = \pi(x - L + l_i)/(2l_i)$.

3.5.2 The wave equation with a varying cable length

Now, considering the fact that the length $l(t)$ of the cable is varying asks to modify the previous calculus, as done in [Kim and Hong, 2009, d'Andréa Novel and Coron, 2002]. We use the same notation as in the previous section, and we denote J the moment of inertia of the winch, R its radius, and L_0 the total length of the cable. See Fig. 6 where u_1 is the force applied to the platform and u_2 the torque applied to the winch.

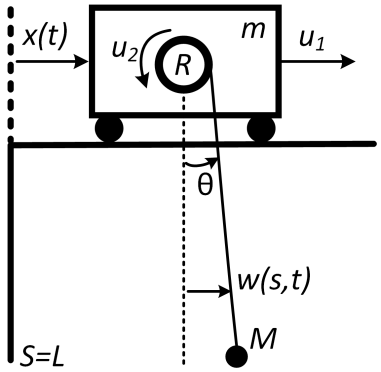

Figure 6: Inline deflection due to the flexibility with winch

Assuming as in [d'Andréa Novel and Coron, 2002], that the cable is completely flexible and non-stretching, and that the transversal and angular displacements are small, we may compute the dynamical model of the cable-load system, that is a partial differential equation of the deviation of the displacement with respect to a fixed position of the trolley, a fixed length for the cable, and the rest position of the cable and the load. To do that we first denote the mass of the part of the cable which is wound on the winch by m_e, we have $m_e = \rho(L_0 - L)$.

Denoting by $\theta(t)$ the angular displacement of the cable at the connection point to the platform, we have

$$w_s(0,t) = \theta(t)$$

The dynamics of the platform at position $x(t) = w(0,t)$, and of the part of the cable wound on the winch is written as

$$(m + m_e)\ddot{x}(t) = u_1 + (\tau(0,t) - \rho\dot{L}^2(t))\theta$$

where the dynamics of the winch is written as

$$(\frac{J}{R^2} + m_e)\ddot{L}(t) = -\frac{-u_2}{R} + \tau(0,t)$$

where $\tau(s,t)$ is still the tension of the cable at curvilinear abscissa s and at time t. The tension could be computed as

$$\tau(s,t) = (M + \rho(L(t) - s))(g - \ddot{L}(t))$$

The partial differential equation for the cable is written as

$$\rho w_{tt}(s,t) = (\tau(s,t)w_s)_s(s,t) - 2\rho\dot{L}(t)w_{st}(s,t) - \rho\ddot{L}(t)w_s(s,t)$$

Of course in the case of a fixed length cable, we retrieve the dynamics of the previous section.

Finally the dynamics of the load mass is written as

$$M\big(w_{tt}(L,t) + 2\dot{L}(t)w_{st}(L,t) + \ddot{L}(t)w_s(L,t) + \dot{L}^2(t)w_{ss}(L,t)\big) = -\tau(L,t)w_s(L,t)$$

According to [Abdel-Rahman et al., 2003], the models in this category are only valid for a lumped mass payload of the same order of magnitude as the mass of the cable and for small trolley displacement and cable angles. So, these models can only be used near the end of the trolley travel. However, even when a crane operates under no-load conditions, the mass of the hook is typically much heavier than the mass of the cable. As a result, this approach has limited practical applications.

3.6 Finite-element models

It is well-known since d'Alembert that the wave equation can be derived from the dynamics of a linear oscillator (a chain of punctual masses linked by linear springs), letting the number of masses (nodes) diverge to infinity. The pendulum with links longitudinal elasticity and/or joint flexibility, can be viewed as a nonlinear oscillator. On the other hand the spatial discretization of infinite-dimensional models like the wave equation, which models the cable in the neighborhood of its vertical posture, yields finite-dimensional dynamics via the finite-element method. In particular the linear oscillator corresponds to the inconsistent mass matrix discretization of the wave (or string) dynamics [Egeland and Gravdahl, 2002]. It is interesting to understand the discrepancies and similarities between these discretized dynamics, and lumped-mass pendulum models. In particular it seems that no study of overhead cranes has yet been published in the Automatic Control literature which uses a finite-element model. A short survey is made now.

3.6.1 Cable as an elastic curvilinear domain

Contrarily to the wave dynamics which describe the cable's dynamics in a neighborhood of the vertical posture, another class of models considers the cable as an elastic curvilinear domain, and allows for large deformations Bertrand et al. [2020]. The obtained dynamics contain nonlinearities. Each infinitesimal element of the cable has the local dynamics $\rho(S)\ddot{\mathbf{x}}(S,t) = \mathbf{R}'(S,t) + \mathbf{b}(S)$, $S \in [0, L]$ is the Lagrangian curvilinear abscissa, L is the cable's length, $\mathbf{R}(S,t)$ is the linear elastic constitutive law of the cable, $\mathbf{b}(S) \in I\!R^3$ gathers the distributed body forces applied to the cable, $\mathbf{x} \in I\!R^3$ is the vector of positions of the cable particles (hence this model applies to 3D operating space), $\rho(S)$ is the cable's linear density. The superscript $'$ is for differentiation with respect to S, the dot is for time derivative. Boundary conditions have to be imposed for $x(0,t)$, $x(L,t)$, $\mathbf{R}(L,t)$ and $\mathbf{R}(0,t)$. The finite element approach considers a certain number of cable's elements indexed by $\mathbf{e} \in I\!N$. Roughly speaking, setting nodal unknowns $x_e \in I\!R^{n_e}$ and shape functions matrices $N(\xi) \in I\!R^{3\times n_e}$, where $\xi \in [0,1]$ is a non-dimensional variable, permits to obtain the dynamics of each element as $M_{\mathbf{e}}\ddot{X}_{\mathbf{e}} + K_{\mathbf{e}}(X_{\mathbf{e}})X_{\mathbf{e}} - b_{\mathbf{e}} - p_{\mathbf{e}}$. The concatenation of the dynamics of each element, yields global dynamics with a similar form as (43) (46), where the nonlinearities are lumped in the

stiffness. Once the **e** elements have been assemblied together and the coordinates have been suitable reduced to a set of independent coordinates, it is found that the cable's dynamics (the counterpart of the pendulum's dynamics) is:

$$M\ddot{X}(t) + K(X(t))X(t) = b(t) + p(t), \tag{79}$$

The vector X groups the Cartesian coordinates of both edges of each element of the cable. It is noteworthy that (79) possesses the same form as (43) (46), with constant mass matrix and nonlinear stiffness (which make these approaches significantly depart from more classical approaches that yield linear dynamics [Egeland and Gravdahl, 2002, Quan and Chang, 2020]). One difference is that in (43) (46) M is diagonal (it is an inconsistent spatial discretization), while it may have off-diagonal entries in (79) depending on the choice of the shape function matrix (consistent spatial discretization).

3.6.2 Other finite-element dynamics: cable vibration control

Finite-element 3D dynamics are derived and used for vibration control in [Gattulli, 2007, Johnson et al., 2007, Faravelli and Ubertini, 2009, Ubertini, 2008], using displacement components along the Cartesian frame. Basic assumption is that the cable is horizontally suspended between two end-points, with little or negligible sag (main applications are in cable-suspended bridges), no longitudinal extension and with small deflection $w(x,t)$. The dynamics in [Johnson et al., 2007] is linear. The dynamics obtained in [Gattulli, 2007, Equations (9) and (27)] (and also in [Gattulli et al., 2004, Faravelli and Ubertini, 2009, Faravelli et al., 2010, Ubertini, 2008]) are nonlinear in the stiffness term. Cubic displacement nonlinearities are derived in [Gattulli, 2007, Equation (27)]:

$$M\ddot{q}(t) + (1 - \mu q^{\top}(t)Nq(t))Gq(t) = f_{damp}(q(t), \dot{q}(t)) + f(t), \tag{80}$$

where $N = N^{\top}$ is a nondimensional matrix, G is a geometric stiffness matrix, and q contains transversal displacements obtained from Rayleigh test functions $\phi_i(x)$, *i.e.*, $w(x,t) = \sum_{i=1}^{n} q_i(t)\phi_i(x)$. The term f_{damp} represents viscous dampers mounted on the cable. It is noteworthy that the objective in [Gattulli, 2007, Johnson et al., 2007, Faravelli and Ubertini, 2009, Faravelli et al., 2010, Ubertini, 2008] is to design controllers that control vibrations, with either active or passive inputs, using advanced control theory.

3.6.3 Cables modeling: conclusions

As surveyed in Lv et al. [2020], several classes of cables models exist, and possess their own advantages and drawbacks, especially when accuracy and calculation complexity are considered [Lv et al., 2020, Table 1]. However, their suitability for control design apparently remains a largely open issue. GEFBE and ALE-ANCF methods should be considered in priority, since they allow for large deformations.

3.7 Complementary-slackness constraints: nonsmooth cables models

Almost all the above modelling approaches (excepted in section 3.6.1) neglect one essential feature: cables, like ropes, cannot exert forces with arbitrary sign along their longitudinal axis. Roughly speaking, cables can pull but they cannot push: they work only in traction [Gueners et al., 2021]. This implies that two main modes have to be modelled: the tensile mode (with or without cables extensibility and elasticity) and the slack mode (in the case of prestressed cables, the slack mode is likely to never occur). The transition from the slack to the tensile mode, can be accompanied by an impact and lead to bouncing motion. Though this may be more present in tethered systems, some overhead crane applications may undergo such effects [Yoon et al., 2010, 2014], if the cable is very long and the payload mass is comparable to that of the cable and the trolley has large accelerations (or a perturbation acts on the payload). Other applications with cable-suspended payloads are in [Foehn et al., 2017]. This yields so-called complementarity constraints [Brogliato, 2016, Example 1.6] [Kanno, 2011] which have to be added in the Lagrange dynamics, rendering them nonsmooth [Brogliato, 2016, Chapter 5]. Let us introduce this modelling approach. It is assumed that the cable is slack if the distance between its tips is smaller than $L > 0$. In other words, if the distance between the attachment points A_0 and A_N is less than L, see Figure 7. The projection of the payload node A_N onto the constraint boundary circle is P_N, and the gap function entering the complementarity constraints is $h(q) = (P_N A_N)^\top \mathbf{n}$ [Brogliato, 2016, sections 4.1.3 and 5.4.1], where $||\mathbf{n}|| = 1$. Calculations yield $h(q) = L - \sqrt{(x_N - x)^2 + y_N^2}$. If the cable is inextensible (fixed links' lengths, hence $N + 1$ degrees of freedom), and given a suitable generalized minimal coordinate vector $q \in I\!R^{N+1}$, the Lagrange dynamics has to be modified as follows:

$$\begin{cases} M(q)\ddot{q} + C(q,\dot{q})\dot{q} + G(q) = Q + \nabla h(q)\lambda_{\rm n} \\ 0 \le \lambda_{\rm n}(t) \perp w(t) = h(q(t)) \ge 0 \\ \nabla h(q)^\top \dot{q}(t^+) = -e_{\rm n}\nabla h(q)^\top \dot{q}(t^-) \text{ if } h(q(t)) = 0 \text{ and } \nabla h(q(t))^\top \dot{q}(t^-) < 0, \end{cases} \tag{81}$$

where $\lambda_{\rm n}$ is the multiplier associated with the unilateral constraint, $e_{\rm n} \in [0,1]$ is the restitution coefficient (the loss of kinetic energy at an impact depends on the cable's internal damping). The mulitplier λ_{rmn} represents the tension in the cable, it is calculated using the contact linear complementarity problem (LCP). Since the links' lengths are constant $L = \sum_{i=1}^N l_i$. The dynamics in (81) is nonsmooth and its study is thoroughly covered in the literature, see [Brogliato, 2016]. Assume that $q = (x, \alpha_1, \ldots, \alpha_N)^\top$ (see Figure 3). Computing $(P_N A_N)^\top \mathbf{n}$ yields $h(q) = L - \sum_{i=1}^N l_i \sin(\alpha_i) \sin(\arctan\left(\frac{\sum_{i=1}^N l_i \sin(\alpha_i)}{\sum_{i=1}^N l_i \cos(\alpha_i)}\right)) - \sum_{i=1}^N l_i \cos(\alpha_i) \cos(\arctan\left(\frac{\sum_{i=1}^N l_i \sin(\alpha_i)}{\sum_{i=1}^N l_i \cos(\alpha_i)}\right))$. It can be checked that at an impact (or a contact) time where $\alpha_i = \alpha$ for all $1 \le i \le N$ for some α (the cable is stretched) and since $\sum_{i=1}^N l_i = L$, then $h(q) = 0$. The gap function is easily rewritten if $q = (x, \theta_1, \ldots, \theta_N)^\top$. If redundant coordinates $q = (x, x_1, \ldots, x_N, y_1, \ldots, y_N)^\top$ are chosen, then the gap function simplifies (see above) but bilateral (equality) holonomic constraints $g_i(q) = (x_i - x_{i-1})^2 + (y_i - y_{i-1})^2 = l_i^2 = 0$, $1 \le i \le N$, have to be added to (81) (we set $x_0 = x$). Then the gradient $\nabla h(q)$ is easily calculated, but the analysis of the impact/contact problem is made more complex due to the bilateral constraints which distort the contact LCP [Brogliato, 2013, Blumentals et al.,

2016] [Brogliato, 2016, section 5.1].

Remark 6 *Calculations show that* $\frac{\partial h}{\partial \alpha_n}(q) = 0$ *at impact times for any* $1 \leq n \leq N$. *Hence the unilateral constraint has no effect on the dynamics and does not induce state jumps (see (81)). This is due to the fact that when the pendulum is stretched, a singularity occurs (as is well-known in Robotics) and a "contact" force along* $\mathbf{n}$ *cannot make the pendulum move. Let* $q = (x, x_1, \ldots, x_N, y_1, \ldots, y_N)^\top$. *Then* $\frac{\partial h}{\partial y_N} = \frac{-y_N}{\sqrt{(x_N - x)^2 + y_N^2}}$ *hence* $\frac{\partial h}{\partial y_N} = 1$ *at an impact time and applying (81) yields* $\dot{y}_N(t^+) = -e_{\rm n}\dot{y}_N(t^-)$. *However all other gradients vanish, proving that the other coordinates cannot be discontinuous. Then the equality constraints derivative* $\nabla g(q(t))^\top \dot{q}(t) = 0$ *at all times yields a contradiction. In fact impacts in bilaterally/unilaterally constrained systems require specific analysis and conditions to be well-posed [Brogliato, 2013, section 6]. In other words, a multibody model like the N-pendulum is incapable of reproducing any "bouncing" of the cable due to its inextensibility. First this is a big discrepancy compared to true impacts with an obstacle. Second it calls into question the use of a multibody model without longitudinal links' elasticity if such slack/taut dynamics is to be modeled.*

It is noteworthy that links with longitudinal elasticity can also be embedded in a complementarity framework *via* a unilateral spring, with $L = \sum_{i=1}^N l_{i,r}$, $l_{i,r}$ are the springs rest lengths. We assume that if the cable's tip A_N is outside the circle with radius R and center A_0, then it is stretched with all angles equal to α. It is also assumed that longitudinal linear elasticity is modeled as in (55). The longitudinal unilateral spring exerts a tensile force $F \in I\!R^2$ along $\mathbf{n}$ which takes the form:

$$F = \begin{cases} 0 & \text{if} \quad h(q) \geq 0 \\ \frac{\Pi_{i=1}^N k_i}{\sum_{i=1}^N k_i}(-L + \sqrt{(x_N - x)^2 + y_N^2})\mathbf{n} = -\frac{\Pi_{i=1}^N k_i}{\sum_{i=1}^N k_i} h(q)\mathbf{n} & \text{if} \quad h(q) < 0. \end{cases} \tag{82}$$

The switching "contact" force in (82) is equivalently rewritten in a complementarity framework as $F = \lambda \mathbf{n}$ where λ is the solution of:

$$0 \leq \lambda_{\rm n} \perp \lambda_{\rm n} + \frac{\Pi_{i=1}^N k_i}{\sum_{i=1}^N k_i} h(q) \geq 0 \Leftrightarrow \lambda_{\rm n} = \max(0, -\frac{\Pi_{i=1}^N k_i}{\sum_{i=1}^N k_i} h(q)). \tag{83}$$

The corresponding continuously differentiable unilateral elasticity potential energy is

$$U_{uel}(h) = \begin{cases} 0 & \text{if} \quad h \geq 0 \\ \frac{1}{2}\frac{\Pi_{i=1}^N k_i}{\sum_{i=1}^N k_i} h^2 & \text{if} \quad h < 0. \end{cases} \tag{84}$$

Therefore $\frac{\partial U_{uel}(h(q))}{\partial q} = \frac{\partial h}{\partial q}\frac{\partial U_{uel}(h)}{\partial h} = \nabla h(q)\frac{\partial U_{uel}(h)}{\partial h} = \nabla h(q)\lambda_{\rm n}$ enters the right-hand side of the Lagrange dynamics:

$$\begin{cases} M(q)\ddot{q} + C(q,\dot{q})\dot{q} + G(q) = Q + \nabla h(q)\lambda_{\rm n} \\ 0 \leq \lambda_{\rm n} \perp w(t) = \lambda_{\rm n} + \frac{\Pi_{i=1}^N k_i}{\sum_{i=1}^N k_i} h(q) \geq 0. \end{cases} \tag{85}$$

The big difference between the complementarity Lagrange dynamics in (81) and in (85), lies in the relative degree r between the complementarity variables $\lambda_{\rm n}$ and w: in (81), and provided the gradient matrix has full column rank, $r = 2$ while in (85), $r = 0$ [Brogliato, 2016, Brogliato and Tanwani, 2020].

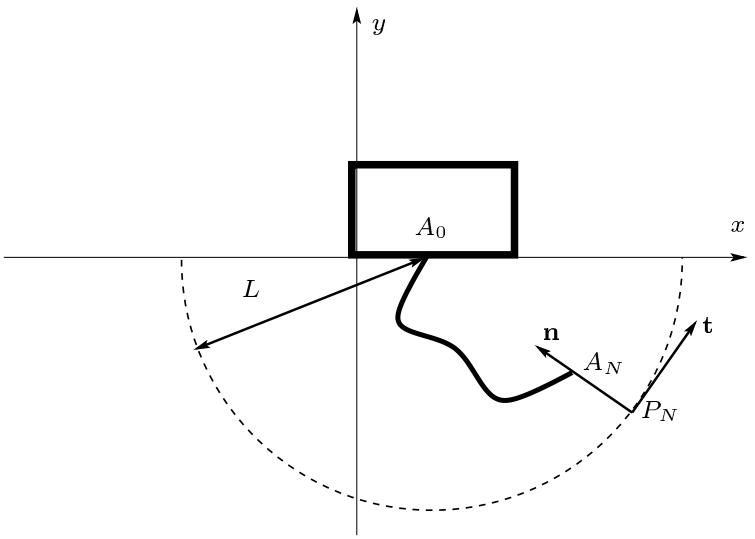

Figure 7: Slack cable.

3.8 Natural frequencies of the double-pendulum system

One of the objectives of this project is to calculate the natural frequencies of the double-pendulum system. This can be done by linearization of the Euler-Lagrange model around the nominal operating point as done in [Singhose et al., 2008], and the following formula has been obtained:

$$\begin{aligned} \omega_{1,2} &= \sqrt{\frac{g}{2}}\sqrt{(1+R)\left(\frac{1}{L_1}+\frac{1}{L_2}\right) \mp \beta} \\ \beta &= \sqrt{(1+R)^2\left(\frac{1}{L_1}+\frac{1}{L_2}\right)^2} \end{aligned} \tag{86}$$

where R is the ratio of the payload mass to the hook mass. This formula has been validated for a double=pendulum system with hook mass 0.4326kg, load mass 8.8 kg, $l_1 = 1.079m, l_2 = 0.27m$. According to this formula, the natural frequencies are 0.4308 and 4.9367 Hz. The spectrum of the first angle sway has been provided in Fig. 8. According to this photo, one can see that the dominant frequency component of the first sway angle is equal to 0.43 which validates the formula. Note that this waveform has been obtained under an open-loop control force.

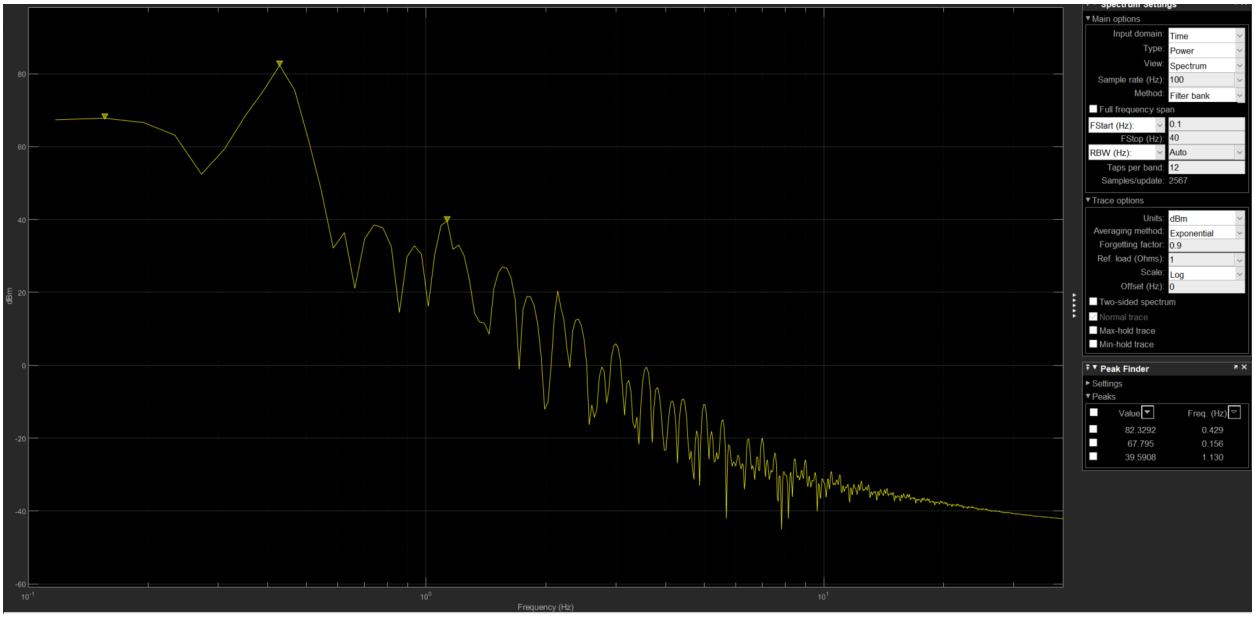

Figure 8: Spectrum of the first sway angle

4 Models: multiple-cable gantry cranes

Most of overhead crane systems are designed with several cables and pulleys mounted on the trolley, hook, and spreader. Single-cable models may then be seen as an approximation where the multiple-cable dynamics/kinematics is lumped in a unique equivalent cable, however, they are unable to take the rotations of the payload/hook into account. A fine model has to take into account the kinematics of the pulley/multiple cables, which does not exist in the case of a single cable. During gross motions of the system, the multiple-cable crane may be modelled as a single-cable crane (in which case an equivalent cable has to be determined). During static postures (trolley at rest), multiple cables introduce a specific kinematics between the trolley and the payload, which can be used for fine manipulation and stabilization of the payload: the overall control problem is then similar to that of cable-driven robotic systems [Wei et al., 2017], the study of which has witnessed an abundant literature in the Robotics scientific community [Merlet, 2017, Lamaury and Gouttefarde, 2013]. Multiple-cable mechanisms can be very useful to control the motion of the payload as described in section 3.4.3.

Some studies have been conducted to model or control cranes with multi-cables. The first approach in this category is to consider the cables as rigid links studied by [Morrish et al., 1997, Nayfeh et al., 2005, Nayfeh and Baumann, 2008, Cartmell et al., 1996, Kim et al., 2004]. More accurate models have also been developed in the literature to take the cable's longitudinal extension into account [Morrish et al., 1996, Arena et al., 2013, Cartmell et al., 1996, Arena et al., 2015].

A planar model for a multi-cable crane has been developed by [Nayfeh et al., 2005, Nayfeh and Baumann, 2008] (see also [Kim et al., 2004]) where the cables are considered as rigid links. The diagram used in these

references are shown in Fig. 9. Considering OP= l, the following constraints can be written for the loop AOPB:

$$\begin{cases} l\sin\phi - \frac{1}{2}w\cos\theta + \frac{1}{2}d = L\sin\phi_1 \\ l\cos\phi - \frac{1}{2}w\sin\theta = L\cos\phi_1 \end{cases} \tag{87}$$

Similarly, for the loop ODCP, one has:

$$\begin{cases} l\sin\phi + \frac{1}{2}w\cos\theta - \frac{1}{2}d = L\sin\phi_2 \\ l\cos\phi + \frac{1}{2}w\sin\theta = L\cos\phi_2 \end{cases} \tag{88}$$

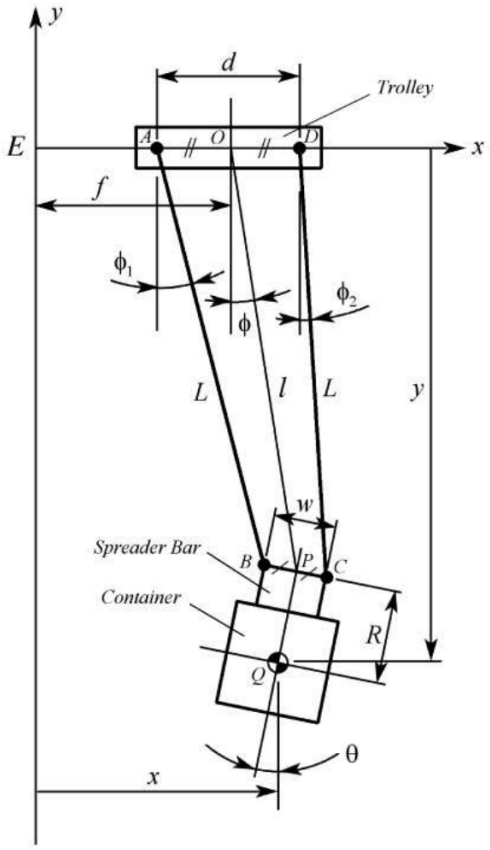

Figure 9: Modeling a multi-cable crane with rigid link [Nayfeh et al., 2005, Nayfeh and Baumann, 2008]

Squaring and adding both equations shown in (87) gives:

$$\left(l\cos\phi - \frac{1}{2}w\sin\theta\right)^2 + \left(l\sin\phi - \frac{1}{2}w\cos\theta + \frac{1}{2}d\right)^2 = L^2. \tag{89}$$

And for the (88)

$$\left(l\cos\phi + \frac{1}{2}w\sin\theta\right)^2 + \left(l\sin\phi + \frac{1}{2}w\cos\theta - \frac{1}{2}d\right)^2 = L^2. \tag{90}$$

Eliminating L^2 from (89) and (90) gives:

$$d\sin\phi = w\sin(\phi+\theta) \tag{91}$$

This equation shows that for a multi-cable crane when the cables are considered as rigid links, the sway angles are not independent, like the one for the single-link double-pendulum system. Substituting (91) into (90) gives:

$$l^2 = L^2 - \frac{1}{4}(d^2 + w^2 - 2dw\cos\theta) \tag{92}$$

The value of l from (92) can be used for a single-pendulum approximate model as shown in Fig. 10.

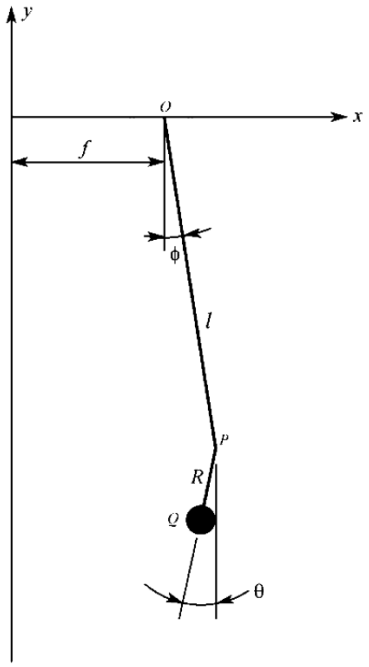

Figure 10: Modeling a multi-cable crane with rigid link [Nayfeh and Baumann, 2008]

A 3D modeling scheme (compared to [Nayfeh et al., 2005, Nayfeh and Baumann, 2008] which was developed for the planar movements) for the cranes with four rigid links have been presented in [Morrish et al., 1997, Cartmell et al., 1996]. This model can be specially used for rubber tyred gantry (RTG) cranes shown in Fig. 11. The kinematic of the RTG crane is specifically addressed in these studies with the selected frames illustrated in Fig. 12. The effect of the cable stretch on this model has also been taken into account by [Arena et al., 2015, 2013], and it is shown that it can change the payload oscillation by 8% depending on the cable length. The purpose of such studies is to obtain the position and the rotation of the payload required to calculate the Lagrangian.

All the studies on the multi-cable modeling, *i.e.*, [Nayfeh et al., 2005, Nayfeh and Baumann, 2008, Arena et al., 2015, 2013, Morrish et al., 1997, Cartmell et al., 1996], share the following specifications:

- The dynamic of the trolley is neglected, *i.e.*, its energy is ignored when calculating the Lagrangian.
- These models are developed without considering the external forces. The only exception is [Cartmell et al., 1996] where the effect of the wind disturbance, and not the control force, is considered.

- Reference [Cartmell et al., 1996] is the only one that considered the control problem of the multi-cable system. However, this is a fuzzy control method that is designed based on the linguistic fuzzy rules, and not the mathematical model. Moreover, the controller is to generate the desired trajectory, and not the force.
- The effect of the sway angles corresponding to the skew rotations has not been considered in these references.

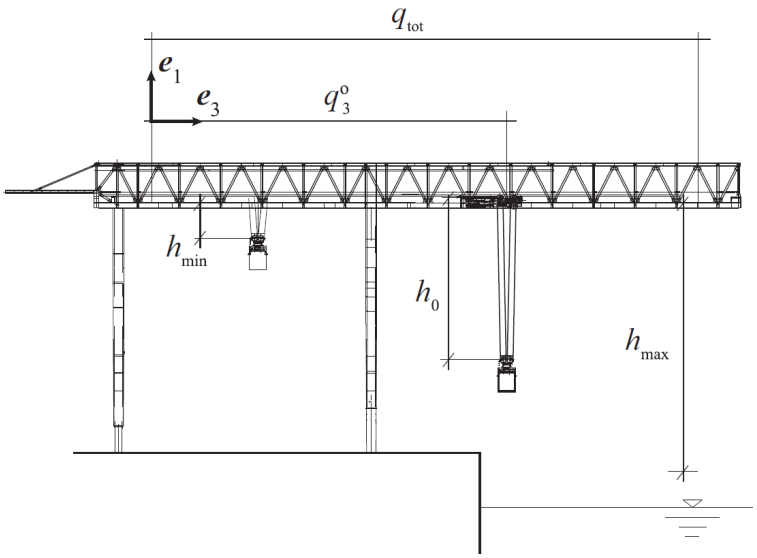

Figure 11: Schematic of a RTG crane

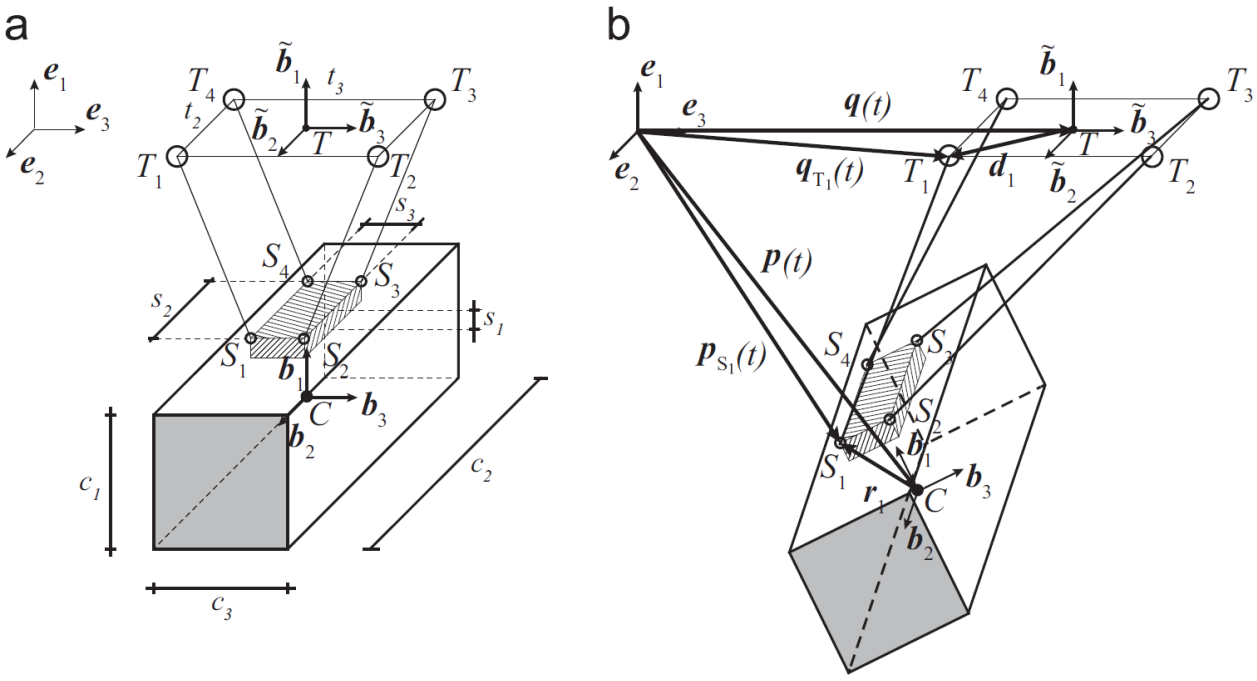

Figure 12: Frames considered in [Arena et al., 2015] to address the kinematic of RTG cranes.

5 Models used in the Control Literature

This section surveys the modelling approaches which have been chosen in the Automatic Control literature dedicated to overhead cranes, since the beginning of the 1980s.

5.1 Dimension of the operating space

Industrial cranes operate in 3D space. However, for the sake of simplicity, some references provide the models only for a 2D space. Depending on the operating space dimension, the references can be classified into the following parts.

5.1.1 2D models

The most convenient but not necessarily accurate way to model an overhead crane is to consider that as a single-pendulum mounted on a trolley (see Section 2.5 for $N = 1$). In this solution, the cable is assumed to be a rigid massless link as explained in Section 3.1. Such a strategy has been employed in many studies such as [Schindele and Aschemann, 2011, Ngo and Hong, 2012, Chen et al., 2019, Hamdy et al., 2018, Zhang, 2019, Chen et al., 2016, Bonnabel and Claeys, 2020, Singhose et al., 2000, Ohnishi et al., 1981, Manson, 1982, Yoshida and Kawabe, 1992, Fliess et al., 1991, Yu et al., 1995, Lee et al., 1997, Liang and Koh, 1997, Singhose et al., 1997, Collado et al., 2000, Fang et al., 2001, Piazzi and Visioli, 2002, Hong et al., 2003, Yi et al., 2003, Omar, 2003, Omar and Nayfeh, 2005, Kuo-Kai Shyu et al., 2005, Kolonic et al., 2006, Hičár

and Ritók, 2006, Park et al., 2008, Aschemann, 2009, Sano et al., 2010, Le et al., 2012, Sun and Fang, 2012, Wu and Xia, 2014, Zhang et al., 2014, Vaughan et al., 2010, Chen et al., 2016, Smoczek and Szpytko, 2017]. Some studies have also taken into account the friction between the trolley and the surface [Fang et al., 2012, Wu and He, 2015, Wu et al., 2015, Zhang et al., 2017a]. In addition to the friction, some references [Lu et al., 2017] have also considered the disturbances as external forces appear in Q (see (2)).

The single-pendulum model may not be accurate enough specially in the presence of heavy hooks. In this case, double pendulum models (see Section 2.5 for $N = 2$) are employed by [Sun et al., 2017, Ramli et al., 2017, Sun et al., 2018, Sun et al., 2019, Ouyang et al., 2019a, Singhose et al., 2008, Zhang et al., 2016, Tang and Huang, 2016, Khorshid and Al-Fadhli, 2021, Ouyang et al., 2019, Ouyang et al., 2019b, Sun et al., 2018, Sun et al., 2019]. This scheme also allows to study the wind disturbances applied to the trolley [Zhang et al., 2016]. Double pendulum with trolley friction is also considered by [Ouyang et al., 2019, Ouyang et al., 2019b, Sun et al., 2018]. Double pendulum models with joint flexibility [Sun et al., 2019] has also been considered to avoid PDEs corresponding to cable modeling. Distributed payload mass in double-pendulum model was also the topic of [Tang and Huang, 2016].

In real Cranes, there is always a hoisting mechanism which is composed of a winch which are completely ignored in the above-mentioned references. To fill this gap, some studies has also taken into account the dynamic of the hoisting mechanism as can be seen in [Sakawa and Shindo, 1982, Auernig and Troger, 1987, Moustafa, 1994, Kimiaghalam et al., 1999, Bartolini et al., 2000, Karkoub and Zribi, 2001, Bartolini et al., 2002, Lee, 2004, Kim et al., 2004, Lee et al., 2006, Park et al., 2007, Moon et al., 2013, Le et al., 2014, Park et al., 2014, Sun et al., 2015].

Compared to the above-mentioned modeling schemes, another approach is to consider the cable as a flexible object as explained in Section 3.5 [Chentouf and Han, 2020, He and Ge, 2016, Shen and Caverly, 2020, d' Andréa-Novel and Coron, 2000, d'Andréa Novel and Coron, 2002, Alli and Singh, 1998]. Small transversal displacements is the main assumption of such strategies. Hence, these models are mainly introduced for vibration control. As the results, when dealing with large transversal displacements caused by shocks, large amounts of forces or external disturbances, these kinds of models may not be efficient enough. Moreover, a spatial discretization method might be necessary along with this modeling strategy to convert the PDEs into ODEs appropriate for numerical simulations or controller design.

In addition to the cable dynamics, the payload can also play an important role on the overall dynamic equations. In this context, introducing more sophisticated models rather than just point-mass models was the topic of some studies (for instance, see [Alshaya and Alghanim, 2020, Khorshid and Al-Fadhli, 2021] where the dynamics of the payload containing liquid has been considered).

In addition to the aforementioned modeling scheme, special modeling issues can also be found in the literature. For special cases when there are two trolleys [Lu et al., 2020], or modeling the Multi-rope structures [Lu et al., 2018]. In this category, the effect of "shearing deformation" and "rotational inertia" of the bridge beam are also taken into account in a PDE model [Xing et al., 2020].

5.2 Other static/dynamic effects

In addition to the trolley, cable and payload, other parts can also potentially affect the operation of an industrial crane such as dynamics of electric Motors [Ebeid et al., 1992, Omar and Nayfeh, 2005], friction between the trolley and the surface [Fang et al., 2012], etc. Considering these details can be very crucial in real implementation. For example, [Omar, 2003] has reported that without considering the friction, the experimental results can be unacceptable.

The strategy used by [Sun and Fang, 2012] for friction compensation is interesting since it is independent of the controller design. In other words, the inverse of the friction model is used to modify the input force for friction compensation.

6 Control strategies

The main control objective in any industrial crane is to put the payload into the desired position as fast as possible with as small as possible payload sway. To this end, the controllers are designed based on one of the following strategies:

- **Input-shaping**: this is an open-loop control scheme where the force is calculated offline based on the system's dynamic equation.
- **Trolley control (collocated control)**: as it can be inferred from the name, this strategy mainly controls the trolley position/velocity without directly taking into account the sway angles.
- **Payload control (noncollocated control)**: in this strategy, the controller directly takes into account both the trolley position/velocity and the sway angles.

One can find a few surveys on crane control methods in the literature [Ramli et al., 2017, Abdel-Rahman et al., 2003, Bonnabel and Claeys, 2020]. Comparing these two strategies, the trolley control strategy usually needs less number of sensors since the payload control usually requires some additional feedback from the payload. A general study has been conducted by [Vaughan et al., 2010] on the input-shaping methods and it is concluded that the input-shaping or more generally open-loop control can provide more economical solutions compared to the closed-loop control systems.

6.1 Input-shaping

Input-shaping is a completely open-loop strategy where the input of the system (usually force applied to the trolley) is calculated such that the natural frequencies of the sway angles are not excited (see for example [Hazlerigg, 1972] for the very first works in this topic). A common approach in this category is to obtain the dynamic equations and extract its linearized approximation around a nominal operating condition. The linear model is then used to analyze the modes or natural frequencies of the payload. This approach is usually

used along with a human-operated crane system where the trajectory is generated by the driver [Singhose et al., 1997]. Input-shaping can also be integrated with some other algorithms like the one which is presented in [Tang and Huang, 2016] where an input-shaping method is integrated with a wind rejection algorithm to help an operator get rid of the wind disturbances as well as load sway. The input-shaping technique has also been developed for double-pendulum models to avoid excitation of the primary and secondary oscillatory modes [Singhose et al., 2008, Vaughan et al., 2010]. Some references have also considered input-shaping design for specific applications such as a suspended liquid container with sloshing dynamics [Alshaya and Alghanim, 2020, Khorshid and Al-Fadhli, 2021].

Zero-vibration (ZV) [Singhose et al., 1990] and zero-vibration-derivative (ZVD) [Vyhlídal et al., 2013] are two well-known input-shaping algorithms which achieve sway reduction by convolving the desired command with a sequence of impulses to obtain the amplitudes and time locations of the impulses for sway reduction. These approaches have also been utilized by taking into account some constraints on the sway angles during the transient [Hong et al., 2003]. While input shapers are usually designed based on tangent linearization of the nonlinear models, there are also some works that are dedicated to nonlinear input-shaping design based on heuristic algorithms such as particle swarm optimization (PSO) [Maghsoudi et al., 2017].

Another input-shaping scheme has been proposed by [Alhazza et al., 2016] based on the trigonometric manipulations of the responses when tangent linearization is employed. It is shown that in the nominal case (when there is no perturbation), the final sway can be eliminated. Moreover, this method shows faster responses compared to the ZV method. The effect of the hoisting during the motion in the presence of several input shapers has also been studied by [Singhose et al., 2000]. It should be noted that in the input-shaping strategy, the required force is directly generated to be applied to the cart. It is different from the so-called command-shaping strategy where the cart's trajectory is modified in order to reduce the payload sway. In other words, for the command-shaping strategy, a closed-loop controller has to be used to generate the required force based on the shaped trajectory.

6.2 Trolley control

Compared to the input-shaping, this is a closed-loop strategy where the aim is to control the trolley position without directly taking into account the payload's dynamic. This strategy is also called collocated control since only the collocated feedback (trolley position, velocity, and acceleration, *etc.*) is used to synthesize the control law. Unlike the input-shaping, the required force applied to the trolley is calculated by a closed-loop controller based on the trolley position and/or velocity feedback according to the following strategies:

6.2.1 PID and linear controllers

PID control is the most utilized one in the collocated strategy. This kind of controller is implemented by default on many motor speed drivers used in industrial cranes. PID controllers are usually designed based on the tangent linearized models using classic control tools like loop-shaping [Lee et al., 1997]. Reference

[Ouyang et al., 2019a] has developed a velocity reference trajectory for the trolley based on the S-curve technique to control the sway. Afterward, a PID controller has been used to track the mentioned velocity reference where the only feedback signal is the trolley position. Similarly, a PID controller along with a command-shaping scheme has been developed in [Garrido et al., 2008] for sway control. The proposed method can detect sway angle specifications caused by disturbances using filters and generate appropriate velocity trajectories to remove their effects. Many details like PID tuning, filter design, and practical implementations have been addressed in this paper which make it worthwhile for practical applications. It is shown in [Weiping et al., 2004] that a single PD controller with just feedback from the trolley can make the whole system asymptotically stable including the underactuated dynamics even in a 3D space [Ouyang et al., 2021]. However, it is noted in [Ouyang et al., 2021] that this strategy may lead to poor sway reduction. Hence, extra measurements from the sway angles are included in the control law by [Ouyang et al., 2021] to increase the damping on the angles. [Kimiaghalam et al., 1999] has obtained the linearized dynamic corresponding to the trolley and then used the inverse of the model as the feed-forward controller. Subsequently, a genetic algorithm is used to generate the optimal trajectory for collision avoidance and sway reduction.

6.2.2 Flatness

Flatness theory is studied in the literature to handle the underactuated dynamics of overhead cranes. The aim of this method is to modify the reference trajectories in order to achieve the payload position tracking [Fliess et al., 1995]. This is mainly an open-loop technique that can be combined with other closed-loop controllers [Zhang et al., 2017b, Knierim et al., 2010, Diwold et al., 2022]. Before explaining this topic, it should be noted that desired trajectory is normally defined for the payload and not for the cart. Assuming that x and x_p are positions of the cart and the payload, respectively, the control objective is that x_p converges to the desired payload trajectory, *i.e.*, $x_p \to x_{pd}$. For $\theta = 0$, x_{pd} is equal to the desired cart position x_d which may not be the case during the motion when $\theta \neq 0$. According to the literature, the flatness theory can help with the following items:

- Calculating the desired cart position x_d based on the desired payload position x_{pd}. This is especially useful for applications with the pre-installed speed driver where the input is the desired trolley position [Bonnabel and Claeys, 2020, Fliess et al., 1995].
- Flatness theory can be used to generate the desired trajectory based on the desired final position such that the total motion is robust against the perturbations [Zhang et al., 2017b].
- Calculating the control force required for tracking [Zhang et al., 2017b, Fliess et al., 1995].
- System linearization, different from the feedback linearization strategy [Zhang et al., 2017b].

- Taking the actuator dynamic into account for the controller design [Knierim et al., 2010, Fliess et al., 1995].

Flatness theory can only be performed on flat systems. A nonlinear system $\dot{x} = f(x, u)$ with the state vector $x \in \mathbb{R}^n$ and the input $u \in \mathbb{R}^p$ is differentially flat if there is an output $y = g(x, u, \dot{u}, \ldots, u^{(m)}) \in \mathbb{R}^q$ such that x and u can be written as functions of y and a finite number of its derivatives as follows:

$$\begin{cases} x = f_x(x, y, \dot{y}, \ldots, y^{(r_x)}) \\ u = f_u(x, y, \dot{y}, \ldots, y^{(r_u)}) \end{cases} \tag{93}$$

where $r_x \in \mathbb{N}$ and $r_x \in \mathbb{N}$.

Assuming that the Cartesian payload position $y = [y_1, y_2]^\intercal$ is the output of a single-pendulum system, and x and θ be the state variables, one has:

$$\begin{aligned} y_1 &= x + l\sin(\theta) \\ y_2 &= -l\cos(\theta). \end{aligned} \tag{94}$$

Following [Zhang et al., 2017b], the state variables can be written as functions of the output and finite numbers of their derivatives as shown in (95) which indicates the flatness of the system with the flat output y.

$$\theta = \arctan\left(\frac{\ddot{y}_1}{\ddot{y}_2 + g}\right) \tag{95a}$$

$$x = y_1 - \frac{\ddot{y}_1 y_2}{\ddot{y}_2 + g}. \tag{95b}$$

Similarly, the input of the system, *i.e.*, the force applied to the trolley, can also be expressed as functions of flat output and its time derivatives as follows [Zhang et al., 2017b]:

$$\begin{aligned} F = {} & (m_0 + m_1)\tfrac{d^2}{dt^2}\left(y_1 - \frac{\ddot{y}_1 y_2}{\ddot{y}_2 + g}\right) - m_1 l\cos\left(\arctan\left(\frac{\ddot{y}_1}{\ddot{y}_2 + g}\right)\right)\left(\tfrac{d^2}{dt^2}\left(\arctan\left(\frac{\ddot{y}_1}{\ddot{y}_2 + g}\right)\right)\right) + \\ & + m_1 l\sin\left(\arctan\left(\frac{\ddot{y}_1}{\ddot{y}_2 + g}\right)\right)\left(\tfrac{d}{dt}\left(\arctan\left(\frac{\ddot{y}_1 y_2}{\ddot{y}_2 + g}\right)\right)\right)^2 \end{aligned} \tag{96}$$

The above-mentioned equations can be used for several applications. According to [Fliess et al., 1995], (95b) can be used in applications with a pre-installed speed driver where the input is the desired position of the trolley to calculate the trolley trajectory based on the desired payload position in order to suppress the sway at the end of the motion. This equation only depends on g which makes the calculations independent to the system's parameters. Moreover, according to the simulations conducted in [Fliess et al., 1995], in the presence of a non-ideal speed driver (non-perfect trolley position tracking) the overall performances of the system are still acceptable enough (according to [Fliess et al., 1995], this can be concluded from the singular perturbation theory of ordinary differential equation). Note that a PID controller has been used in the example provided in [Fliess et al., 1995] as the speed driver without further addressing its effect in the

design procedure. Furthermore, according to [Knierim et al., 2010], the actuator dynamics can be taken into account when using the flatness theory.

In applications without a pre-installed speed driver, the flatness theory can also be used to generate a payload trajectory for robust movements of the payload. According to [Zhang et al., 2017b], since the diffeomorphic relationship (95) exists, full-state feedback linearization can be performed on the flat output as follows:

$$\begin{aligned} y_1^{(4)} &= u_1 \\ y_2^{(4)} &= u_2 \end{aligned} \tag{97}$$

where u_1 and u_2 are the virtual inputs to be designed in order to generate the desired payload trajectory. Considering that the desired final Cartesian payload position is (y_{1d}, y_{2d}), the dynamic of the error can be formulated as follows [Zhang et al., 2017b]:

$$\begin{aligned} &e_1 = y_1 - y_{1d}, \quad e_2 = \dot{y}_1, \quad e_3 = \ddot{y}_1, \quad e_4 = y_1^{(3)} \\ &\begin{cases} \dot{e}_1 = e_2 \\ \dot{e}_2 = e_3 \\ \dot{e}_3 = e_4 \\ \dot{e}_4 = u_1 \end{cases} \end{aligned} \tag{98}$$

The following virtual control can exponentially stabilize the error dynamic system [Zhang et al., 2017b]:

$$u_1 = -c_1 e_1 - c_2 e_2 - c_3 e_3 - c_4 e_4 \tag{99}$$

where $c_i, i = 1, \ldots, 4 \in \mathbb{R}^+$. The same procedure can be done for u_2. Substituting the obtained virtual control into (98), the desired payload trajectory can be synthesized. Other virtual control signals, *e.g.*, finite-time control [Zhang et al., 2017b], can also be used. The flatness of the discrete-time equations corresponding to the overhead cranes has also been addressed in [Diwold et al., 2022]

6.2.3 Adaptive control

A model reference adaptive control has been proposed in [Abdullahi et al., 2018] for payload sway reduction. In this work, the transfer function of a crane is obtained using tangent linearization considering the torque as the input and position as the output. Subsequently, a feed-forward controller is considered such that under an adaptation law, the system tracks a reference system with the desired damping.

6.3 Payload control

As it was mentioned before, payload control schemes are more sophisticated than trolley control one since they also take into account the payload and receives some additional types of feedback like the sway angles, etc. Moreover, payload control schemes can potentially provide better stability proof since it also takes into account the underactuated dynamics. The studies are categorized below, based on the control strategies.

6.3.1 Gain-scheduling

Gain-scheduling refers to a method where the gains of controllers are calculated offline to build a lookup table based on the operating condition. [Omar, 2003, Omar and Nayfeh, 2005] has developed such a strategy where the gains of a feedback controller are selected based on the linearized model such that the response is critically damped to avoid sway oscillations. The least-square algorithm is also used to estimate the friction parameters in an offline manner.

6.3.2 PID (quasi-PID) control

In addition to the trolley control scheme (see Section 6.2.1), the PID controllers are also employed for payload control. A quasi-PID control law has been proposed by [Sun et al., 2019] based on a Lyapunov function for a double-pendulum model. The state space variables are required to synthesize this control law. A PID controller combined with the neural network to compensate for the steady-state error has also been introduced in [Toxqui et al., 2006].

It should be noted that the application of PID controllers when a driver is in the loop has been considered by [Peng et al., 2012]. In this study, the error signal is the difference between the desired payload position and the real payload position which is measured by a vision sensor. Command-shaping is also utilized along with the PID control loop. However, the stability has not been proved by analytical calculations. Several configurations of PID control families have been studied for overhead cranes by [Omar, 2003] and compared with a fuzzy controller. The dynamic of the actuator has been taken into account in this study and the input of the system is the velocity command, i.e, the controller generates the velocity reference.

6.3.3 Linear state-feedback control

In this method, a linear model is developed based on a linearized model using tangent linearization, and then a state-feedback law is developed based on classic methods like [Ackermann, 2012, Jaulin and Éric Walter, 1996, Piazzi and Marro, 1996, Moustafa, 1994]. Such a strategy is used by [Piazzi and Visioli, 2002] along with a state-observer. Subsequently, a trajectory has been designed based on the inverse of the closed-loop transfer function.

6.3.4 Passivity-based control

The very basics of this method are briefly introduced in Section 3.3.1. While the above-mentioned strategy makes the whole closed-loop control system asymptotically stable (as reported by several references such as [Collado et al., 2000, Fang et al., 2003]), it may not be able to control the payload sway efficiently since the noncollocated dynamics are controlled only because of the natural coupling between the trolley dynamic and the payload one. This issue has been addressed by [Fang et al., 2003] and two new control laws namely, E^2 *coupling* and *nonlinear coupling* have been proposed. While experimental results reveal that the new control

rules can improve the transient response compared to that of the PD control, there are no analytical results to show the stability of the new control laws.

The aforementioned issue has been further addressed by [Sun and Fang, 2012] and supported by analytical results, where horizontal displacements of the payload have been considered as a new output (see (8) in [Sun and Fang, 2012] as well as [Chen et al., 2019]) and it is shown that the map between the input force and the horizontal payload velocity can also be passive and dissipative (see (11) in [Sun and Fang, 2012]). This can be done by defining a new storage function that includes the payload horizontal displacement. Subsequently, a new passivity-based control law has been proposed which includes both actuated (trolley position) and underactuated (payload position) variables and the asymptotic stability has been ensured based on the Lyapunov and LaSalle's invariance theorems. Since the new control law contains the underactuated dynamics, it may lead to a more efficient sway control strategy as reported by [Sun and Fang, 2012]. The same idea has been employed in [Chen et al., 2019] where the problem of the emergency stop of a crane is considered. In such a strategy, the payload position is more important than the trolley position. Hence, the underactuated dynamic, *i.e.*, payload position, has been taken into account in the control design. A new term has been added to the Lyapunov function to guarantee the safety of the braking and make the payload position bounded during emergency braking. This is a full state control feedback, and the asymptotic stability has been ensured based on Lyapunov and LaSalle's invariance theorems.

Another approach for passivity-based control design has also been introduced which is called interconnection and damping assignment (IDA). In this approach, the sum of the potential and kinetic energies are considered as the Hamiltonian of the system and the controller is designed such that the amount of the Hamiltonian is minimized for the desired equilibrium point. IDA-PBC provides a systematic way to obtain stabilization through two steps. The first step is the so-called *energy shaping* where the desired storage function is designed. Subsequently, the *damping injection* technique is utilized to provide asymptotic stability. However, IDA-PBC law usually requires solving PDEs which might be difficult to handle. Such a strategy has been developed for underactuated systems by [Aschemann, 2009] and the implementation on an overhead crane based on some simplifying assumptions, *e.g.*, $\sin(\theta) \simeq \theta$ and $\cos(\theta) \simeq 1$. Subsequently, it is concluded that the IDA-PBC may be sensitive to uncertainties, and friction compensation and uncertainty observers are designed to address this issue.

Passivity and dissipation have been also well-studied for linear time invariant systems. Several available theorems have been reminded by [Alli and Singh, 1998]. Subsequently, two LTI models have been developed for overhead cranes. The first one is based on the tangent linearization of the single-pendulum model. To obtain the other LTI model, the flexibility of the cable corresponding to the single-pendulum model has been taken into account which led to a PDE. Subsequently, the PDE has been solved based on the Laplace transformation to form the transfer functions in the Laplace domain. It is shown that these two transfer functions are positive real (PR). Hence, any strictly positive real (SPR) block can be placed in the feedback path to form a passive closed-loop control system (see [Alli and Singh, 1998] for the related theorems). The

coefficients of such SPR controllers are designed based on an optimization technique. The same strategy has been employed by [Shen et al., 2021] with this difference that the torque applied to the winch drum has been also taken into account for position tracking of the load. Adaptation rules are also designed to make the overall control law independent of the system parameters. The control is based on the full-state feedback where six state variables are required to synthesize the control law. The asymptotic stability has been assured based on the Lyapunov theorem.

An energy shaping method has been introduced by [Sun et al., 2013] for 3D problems where the differentiations of the variable do not appear in the control law to form an output feedback control. The method is different from the IDA-PBC and another storage function has been defined based on the concept of virtual payload. Another PBC design has been introduced by [Wu and He, 2017] where the main contribution is to define a new output function that contains both trolley and payload coordinates. Subsequently, a storage function is defined based on this output. Note that partial feedback linearization is used in the beginning to obtain an appropriate dynamic equation for the control design. Since the position has been taken into account in the error signal, the damping characteristic is not constant and changes according to the distance to the desired position which can reduce both load sway and operation time. Lyapunov theorem and LaSalle's theorems are employed to show asymptotic stability.

In [Zhang et al., 2020], a dynamic equation mapping the control input and the underactuated dynamics has been obtained by canceling the actuated dynamic to show the internal damping. Subsequently, a new storage function containing both actuated and underactuated dynamics has been proposed to form a noncollocated control strategy. The method has been validated experimentally and it is shown that the proposed controller shows appropriate responses in case of overshoot and oscillations. Specifications of some of the passivity-based controllers are summarized below:

Table 1: Specifications of the controllers

reference	control problem
[Sun et al., 2013]	regulation
[Lu et al., 2020]	regulation
[Fang et al., 2012]	tracking
[Sun and Fang, 2014]	tracking
[Sun and Fang, 2012]	regulation
[Fang et al., 2001]	regulation
[Fang et al., 2003]	regulation
[Lu et al., 2018]	regulation
[Sun et al., 2018]	regulation
[Sun et al., 2019]	regulation
[Sun et al., 2017]	regulation
[Lu et al., 2017]	regulation
[Sun et al., 2019]	regulation
[Zhang et al., 2020]	regulation
[Zhang et al., 2018]	tracking

6.3.5 Feedback linearization

As it is reported by [Wu and He, 2017], for underactuated systems it may not be possible to use feedback linearization directly. In this context, either partial feedback linearization or nonlinear coordinate transformation is used.

In [Park et al., 2007], firstly, the dynamic model of an overhead crane considering the length as a time-variant variable has been obtained and it is shown that there is a coupling between the cable's length and the sway dynamic. Subsequently, a control law has been proposed which can be divided into two parts, to control the actuated and underactuated dynamics. Asymptotic stability is also shown using the Lyapunov theorem. However, the feedback linearization approach should be studied more clearly for such a system. [Le et al., 2014] has proposed a partial feedback linearization controller for the trolley motion to control the sway angle. Subsequently, a sliding-mode controller is designed for the hoisting mechanism. The combination of these two controllers is also addressed.

A control scheme based on feedback linearization has been developed in [Chwa, 2009] and its asymptotic stability has been studied. This scheme has also been compared with the PD [Fang et al., 2003] and a Lyapunov-based control called E^2 coupling control law [Fang et al., 2001]. In [Lee et al., 2013], firstly, a single pendulum 3D model has been obtained which includes three inputs and five outputs and then the actuated and underactuated dynamics have been separated. Subsequently, a map between actuated

and underactuated systems has been developed. After that, the feedback linearization technique is utilized to obtain the required control forces for the actuated and underactuated dynamics and finally, the linear combination of these control laws is considered as the controller. This strategy has also been integrated with the SMC by [Tuan et al., 2014]. Another partial feedback linearization has been proposed in [Wu and He, 2016] along with a new error signal for a 3D crane. The reference trajectory is added with some integrations corresponding to the payload sway to provide command-shaping. Asymptotic stability has been ensured using the Lyapunov theory.

A feedback linearization control has been studied in [Boustany and d'Andrea Novel, 1992]. Since this method can be sensitive to the payload mass, an estimation technique has been developed. The exponential stability has been assured using the Lyapunov theorem. Another feedback linearization control for 3D motion of an overhead crane is introduced in [Tuan et al., 2012] where the controller is mainly designed for the actuated parts and the sway angle is considered as an internal dynamic. Subsequently, it is shown that the internal dynamics are asymptotically stable.

While feedback linearization can lead to a lack of robustness (since it relies on the system's parameters) it can stabilize the internal dynamics [Hamdy et al., 2018]. The deadbeat control scheme is then utilized by [Hamdy et al., 2018] after feedback linearization to improve the time optimality. According to [Yu et al., 1995], in feedback linearization, the singularity may occur around the equilibrium point which makes the control design cumbersome. This problem has been resolved by separating the whole dynamics into fast and slow parts, corresponding to the average and oscillatory movements, and designing two different controllers for these parts [Yu et al., 1995].

6.3.6 Sliding-mode control

Sliding-mode control (SMC) is another widely used approach in this topic. In the simplest case, the single-pendulum model with a constant length link is considered, and a linear sliding surface is defined containing the trolley position error, sway angle, as well as their time derivations [Chen et al., 2020]. Subsequently, an equivalent-based control law is proposed, and the asymptotic stability of the closed-loop system is ensured based on the Lyapunov stability theorem. This classic approach has been employed in many references including [Kuo-Kai Shyu et al., 2005]. A similar procedure with a variable length link has also been developed where the sliding surface also contains error variables corresponding to the length of the link [Lee et al., 2006]. The SMCs in this topic need full-state feedback.

SMC with a nonlinear sliding surface has also been introduced for the single-pendulum [Lee, 2004] with variable length cable and double-pendulum [Ouyang et al., 2019] systems. Such a sliding surface can change the damping ratio of the system depending on the operation condition to reduce the load sway [Ouyang et al., 2019]. Finite-time convergence of such a strategy has been studied by [Ouyang et al., 2019]. SMC has also been integrated with disturbance observers to compensate for disturbances based on the single-pendulum model [Lu et al., 2017]. Moreover, [Park et al., 2014, 2008] have developed a fuzzy observer for this purpose

to estimate the dead-zone characteristic of the actuator as an uncertainty. Furthermore, [Moon et al., 2013] has proposed an SMC for trolley position, hoisting, and sway control. Since this control law depends on the payload mass and friction factors, adaptation laws are developed to estimate these parameters [Moon et al., 2013].

In addition to the first-order SMCs, Other variants of the SMCs have also been developed for the overhead cranes such as super-twisting SMC [Vázquez et al., 2014]. Second-order SMC for controlling the trolley in both x and y axes without considering the hoisting mechanism has been addressed in [Bartolini et al., 2000]. This strategy has been further developed by [Bartolini et al., 2002] to include the hoisting mechanism. The sliding surface depends on the load sway for sway reduction. As a result, a kind of virtual damping is added to the closed-loop equations which stabilizes the zero dynamics corresponding to the underactuated dynamic. Such a control strategy has been compared with state-feedback controllers and linear robust controllers like μ-synthesis by [Karkoub and Zribi, 2001].

It should also be noted that SMC has been used along with the feedback linearization scheme because of its robustness. For instance, [Le et al., 2014] has designed a partial feedback linearization controller for the trolley motion to control the sway angle. Subsequently, a sliding-mode controller is designed for the hoisting mechanism. Furthermore, a hybrid control strategy has been proposed by [Tuan et al., 2014] where SMC and partial feedback linearization (PFL) have been utilized together. The PFL is for sway control and the SMC is used for payload lifting and position tracking.

An adaptive tracking SMC has been developed in [Ouyang et al., 2019b] for a double pendulum model where one of the parameters of the sliding-surface, *i.e.*, the pole of the linear sliding surface, is calculated based on an adaptation law. Asymptotic stability has been ensured based on the Lyapunov theorem. Practical experiments show that the adaptive method can improve the tracking performance, compared to a few non-adaptive schemes.

A discrete-time integral SMC (ISMC) has been developed in [Xi and Hesketh, 2010] for a general class of discrete-time linear systems and robustness in the presence of matched and mismatched uncertainties (which cannot be handled in typical SMCs) has been addressed. In this scheme, the order of the closed-loop system during the sliding phase is equal to the order of the open-loop system. The application of this controller to an overhead crane in 3D space is also considered.

A nonlinear 3D model for an offshore container crane has been obtained by [Ngo and Hong, 2012] and a first-order SMC has been developed to control the load position in one-dimensional space as well as load in two-dimensional space. The asymptotic stability of the closed-loop system has been studied using the Lyapunov theorem. An adaptive fuzzy SMC has been developed by [Lee et al., 2014] for trolley position and sway control in two (x, y) directions where two linear sliding surfaces have been defined for the position and sway angle. The values of the sliding surfaces are fed into a fuzzy system through two gains to generate the control signal. The gain of the sway angle is calculated adaptive to achieve both tracking and sway reduction simultaneously. This method is integrated with visual feedback using two cheap handy cameras.

It should be noted that the above-mentioned references mainly utilized explicit (forward) Euler discretization leading to numerical chattering. To solve this issue, saturation functions are utilized instead of the sign function. Some studies have also been dedicated to the numerical chattering reduction of SMCs implemented explicitly using alternative methods. In [Park et al., 2008], the control gain of an SMC is calculated using a fuzzy system to determine the width of the boundary layer of the saturation function to reduce the numerical chattering. Two sliding-mode control, *i.e.*, first and second orders strategies, along with the sliding-mode based differentiators are developed in [Bartolini et al., 2003] and compared with the PI controller and a time-varying feedback strategy. Experimental results indicate that the SMC schemes are more robust than the other counterparts.

An SMC namely "Global-Equivalent" SMC has been introduced by [Wang et al., 2021a] and compared with conventional SMC and the PID controller. The control is designed for the single-pendulum model with a varying length link. The asymptotic stability has been proved using the Lyapunov stability theorem. The simulations show that the proposed scheme shows better transient and steady-state performances. Moreover, it shows less chattering than the conventional SMC. The reaching phase of the system has been ensured. However, the sliding phase as well as the stability of the sliding surface has to be further addressed. Additionally, the chattering reduction mechanism, *i.e.*, replacing the saturation function with the sign one, imposes extra design parameters to the system, where there is not any straightforward tuning procedure. This strategy has been further modified by [Wang et al., 2021b] to form a time-variant sliding surface. This controller has been designed based on the double-pendulum model with a fixed length.

6.3.7 Dynamic programming

The literature shows that dynamic programming is a popular control strategy for overhead cranes. In this method, the control law is calculated in an offline manner based on the model to minimize an objective function for some sort of optimality such as energy [Sun et al., 2018] or time [Zhang et al., 2014]. However, this is an offline scheme that may be too sensitive to uncertainties and disturbances.

Some of the command-shaping schemes can also be categorized in this section. For example, [Zhang et al., 2014] has used dynamic programming to optimize the trajectory based on the command-shaping strategy. In these kinds of studies, the effect of the controller on the optimality of the trajectory is usually neglected.

6.3.8 Convex combination of several time-varying systems

Overhead cranes are classified as nonlinear time-variant systems which makes the control design difficult. [Kolonic et al., 2006] has developed a linear time-invariant model for such a system based on the convex combination of several subsystems linearized around different operating conditions.

6.3.9 Lyapunov-based control design

In this strategy, a Lyapunov function is proposed, and the control law is determined such that the time derivative of the function is negative definite to ensure at least the asymptotic stability of the system. This strategy usually leads to full-state feedback for 2D [Sun et al., 2018] and 3D problems [Fang et al., 2001]. This strategy has also been compared with the LQR and PD controllers for a single-pendulum model [Zhang et al., 2017a]. Note that there is a very strong link between the Lyapunov-based control and passivity-based control when the Lyapunov function indicates the physical energy of the system. In this case, passivity-based theory can be used to investigate the stability and behavior of the system [Sun and Fang, 2012, Fang et al., 2001]. Some studies have also been conducted to develop output feedback strategies based on this scheme [Sun et al., 2017]. Furthermore, it is possible to avoid the control saturation in this method [Sun et al., 2017]. Reference [Wu and He, 2015] has proposed two Lyapunov functions for overhead cranes. The first one only includes the sway angle. Then, by calculating the time derivative, the desired velocity trajectory has been obtained to control the sway. The other Lyapunov function includes both the sway angle and the cart position. Hence, by calculating the time derivative, the control law for force is calculated.

[Zhang et al., 2016] has proposed to integrate the Lyapunov-based control strategies with command-shaping schemes to reduce the payload swinging. The control law as well as the adaptation laws are obtained based on Lyapunov functions for the length of the rope, weights, and eternal forces. In [Fang et al., 2012], a command input-shaping is developed such that if the trolley tracks that, the sway angle will be sufficiently reduced. Then an adaptive controller is designed based on a Lyapunov function. This is a full-state feedback control, and the adaptation laws are for frictions, external forces, cable length, and weights. [Sun et al., 2015], has proposed a Lyapunov function that allows deriving the control laws without having feedback from the sway angle. Furthermore, some adaptation rules are also developed in this study based on the Lyapunov function for uncertainties in the payload's weight, frictions, etc. Lyapunov-based control design has also been considered for a multi-rope overhead crane by [Lu et al., 2018]. A Simple linear state-feedback controller is obtained in the study which just contains the first derivatives of the state variables. Asymptotic stability has also been addressed based on the Lyapunov theorem.

The effect of the time delay in the state feedback when considering PDE models corresponding to flexible cables has been studied by [Chentouf and Han, 2020] and it is shown that the system can remain exponentially stable. A Lyapunov-based feedback controller has been introduced by [d'Andréa Novel et al., 1994] where the model of the overhead crane is described by PDE-ODE models and the flexibility of the cable has been taken into account. This control law only needs the absolute position of the trolley and the angle between the cable and the vertical axis at the attached end. Asymptotic stability of the closed-loop system is ensured, and by studying the *decay of the energy* it is concluded that the provided feedback cannot ensure uniform convergence. See also [Chentouf and Han, 2020] for similar results with an input delay and [He and Ge, 2016] for the use of cooperative control in presence of parameter uncertainties. Note that the Lyapunov approach has also been used for the controller design when the cable flexibility is considered modeled with the joint

stiffness [Sun et al., 2019].

A tracking controller for the 3D space has been proposed in [Zhang et al., 2018]. It is concluded that this controller supersedes the collocated PD and the energy coupling output feedback [Sun et al., 2013] in terms of transient response. Another Lyapunov-based [Shi et al., 2022] control strategy has been introduced for the double pendulum system where the length of the first link is variable. Subsequently, a Lyapunov function has been defined containing the error variables of both the trolley position and the cable's length to obtain the coupled control forces applied to the trolley as well as the cable's winch for the tracking case.

6.3.10 Model-free control

In this category, the mathematical model of the system is not required for the controller design. [Smoczek and Szpytko, 2017] has assumed that the dynamic of the trolley and the sway angle are decoupled. Then two discrete-time transfer functions are obtained for input force to trolley velocity and trolley velocity to the sway angle. These transfer functions have fixed orders (first and second-order models) the coefficients of these models are obtained using particle swarm optimization. Then, the model predictive control is used based on these models.

6.3.11 Backstepping control

Back-stepping strategy is generally utilized for underactuated systems. For overhead cranes, in this strategy, the trolley velocity is firstly considered as a virtual input to control the payload sway. Subsequently, the input force applied to the trolley is designed such that the trolley tracks the velocity reference which was calculated in the first step.

In [d'Andréa Novel and Coron, 2002], considering the flexibility of the cable with variable length, a PDE-ODE model as done in Section 3.5.2, a boundary feedback law is proposed to stabilize the system. Because of the cascade structure, the backstepping control scheme can be utilized for the system [d'Andréa Novel and Coron, 2002]. See also [d'Andréa Novel et al., 2019] for a fixed-length cable, where a controller is designed so that the solutions to the closed-loop system converge in finite time towards the equilibrium. Back-stepping has also been combined with sliding-mode observers to form output feedback control laws [Chen and Saif, 2008].

6.3.12 Fuzzy control

Fuzzy control can also be considered a model-free control scheme since it is designed based on the behavior of the system rather than the mathematical models. These kinds of control strategies are usually provided without solid stability proof. One of the earliest works on this subject has been done by [Liang and Koh, 1997]. In [Zhao and Gao, 2012], a Takagi-Sugeno (T-S) fuzzy model has been developed for an overhead crane based on obtaining the dynamic equations, and linearization over three different points using three

fuzzy rules. Then, the control rules are developed based on these rules. Input delay and actuator saturation are also considered in the control design.

A terminal sliding-mode control has been designed in [Lin et al., 2012] where the uncertainties are estimated using a type-2 fuzzy system. The parameters of the fuzzy system are also tuned online based on adaptation laws developed in the work using the Lyapunov theory. [Chunshien Li et al., 2004] has proposed a self-organizing neuro-fuzzy system based on the pseudoerror concept. It seems that pseudoerror is utilized as a kind of command-shaping. As usual, there is no stability proof for such a model-free control strategy. An adaptive fuzzy control scheme coupled with H_∞ control is designed in [Wu et al., 2017] for a class of nonlinear MIMO underactuated systems with a combination of dead-zone, hysteresis non-linearity at the input, external disturbance, and time-delays. The application of the control scheme for the cranes is then considered.

A fuzzy controller for a single-pendulum model has been developed in [Yi et al., 2003] which requires full-state feedback. In [Yi et al., 2003], a fuzzy inference system has been used for trajectory planning of the trolley to reduce the sway angle based on the single-pendulum model and full-state feedback (four state variables are required). A fuzzy controller has been developed by [Li et al., 2022] for the double pendulum system in 2D space with variable rope to address input uncertainties, *e.g.*, dead-zone. The parameters (weights) of the fuzzy system are updated adaptively, and the effect of the adaptation has been taken into account for the stability proof using the Lyapunov theorem.

6.3.13 Model predictive control

Model predictive control calculates the control sequences based on the model to minimize some objective functions (e.g., corresponding to energy consumption [Wu et al., 2015]) over a horizon while satisfying some constraints like input saturation. Such a control strategy has been already developed based on the tangent linearized [Chen et al., 2016] and nonlinear models [Schindele and Aschemann, 2011] of a single-pendulum.

6.3.14 Optimal control

Optimal control refers to any control method where the aim is to minimize an objective (cost) function. The Linear quadratic regulator (LQR) is probably the most well-known one in the control community. An LQR controller has been developed by [Yoshida and Kawabe, 1992] for the linearized model of a single-pendulum system while satisfying some constraints on the control input to avoid control saturation (see Sakawa and Shindo [1982] when the cable length is variable and Yoshida and Tabata [2008] for the bang-bang control). This approach was further developed for 3D space by [Al-Garni et al., 1995]. However, LQR controller can ensure the optimality just for linear systems (or locally for nonlinear systems). To solve this drawback, soft computing-based algorithms like particle swarm optimization (PSO) have also been developed for optimal control of nonlinear systems. PSO algorithm has been employed by [Maghsoudi et al., 2016] to tune the parameters of a PID controller such that an objective function indicating the payload tracking and sway is

minimized. This scheme has been integrated with a command-shaping scheme and compared with classic PID controllers. However, these approaches usually lead to offline optimizations which may not be efficient enough when dealing with uncertainties and disturbances.

Optimal controllers can be designed to satisfy some constraints on the state variables and the control input as well. Considering the constraints in the optimization usually leads to boundary value problems (see [Auernig and Troger, 1987] which can be solved by Pontryagin maximum principle). However, [Manson, 1982] has reported that optimal controllers can be sensitive to parameters, and they just can provide a kind of sub-optimality for real online applications. Note that flatness theory is widely used in optimal control to provide a map among inputs and the desired outputs while respecting various constraints, *e.g.*, collision avoidance, and sway reduction [Chen et al., 2016].

6.3.15 Adaptive control

An adaptive controller for the double-pendulum system with constant rope in the 3D space has been developed by [Zhao et al., 2021] where the masses and the friction parameters are estimated, The adaptation laws are obtained based on the Lyapunov theory, and the velocity has been estimated as well instead of direct measurement. The results show that the adaptive controller performs better compared to the LQR and SMC in the case of the sway reduction and the transient response.

6.4 Control methods for other crane structures

Control methods have been developed by [He and Ge, 2016, He et al., 2014] with the assumption that a thruster is installed on the trolley which produces an extra control force for the underactuated dynamic which is not the case for our application. Some studies have also considered overhead cranes with multiple trolleys which can be controlled independently, *e.g.*, [Lu et al., 2020]. Control of offshore container for ship-to-ship transportation [Kim and Hong, 2019]. Anti-swing control of a quadrotor suspended payload system with variable length cable [Yang et al., 2021]. Cable suspended from to a helicopter [Ren et al., 2019].

6.5 Sensor selection and state estimation

[Sano et al., 2010] has proposed using vision-based sensors for sway detection, and an observer has been developed for time delay correction corresponding to such sensors. This kind of sensor has been integrated with the time optimal control by [Yoshida and Tabata, 2008]. Estimation of the mass and the payload sway in the single-pendulum model was the topic of [Hičár and Ritók, 2006] where the estimated linearized model of a crane is obtained using Auto regressive models with exogenous variables (ARX). The state estimator is developed based on the Ackermann formula. [Lee et al., 2014] has developed a new visual feedback method using two cheap handy cameras for trolley position, payload sway, and cable length in 3D space. A study has also been conducted by [Kim et al., 2004] on using an inclinometer to estimate the trolley velocity and the

angular velocity of the payload. It is reported that using the proposed method, an inclinometer can provide the same performance as a vision-based observation which is more expensive. An inertial measurement unit (IMU) is used by [Kim and Hong, 2019] to measure the angles. Note that the differentiators, *e.g.*, arbitrary-order super-twisting differentiator (AO-STD) have been also employed to estimate the velocities without directly measuring them [Chen and Saif, 2008].

6.6 Sway control using passive mechanical elements

Some papers have also studied passive sway control using mechanical elements like dampers which are out of the scope of this project. Some of them are [Balachandran et al., 1999].

6.7 Sway control using cable length manipulation

All the above-mentioned studies try to control the payload sway by manipulating the force applied to the trolley as the only control input. However, there are still other studies [Wei et al., 2017, Hayajneh et al., 2008, Bockstedte and Kreuzer, 2005, Abdel-Rahman and Nayfeh, 2000, Abdel-Rahman et al., 2003, Moustafa, 1994] that the sway is controlled by manipulating the cable length. In other words, the cable length is considered a control input rather than a control output. As has been already mentioned in Remark 2, a coupling exists between the winding velocity and the sway [Abdel-Rahman and Nayfeh, 2000, Abdel-Rahman et al., 2003, Moustafa, 1994]. Hence, cable length manipulation can be used to control the sway. Following [Bockstedte and Kreuzer, 2005], and considering Fig. 13, the force along a massless visco-elastic rope is:

$$F_{\text{rope}} = F_0 + c(l - l_0) + d(\dot{l} - \dot{l}_0), \tag{100}$$

where c and d are the stiffness and damping parameters. The force $F_0 = mg$ and the length l_0 are the rope properties at equilibrium ($l = \dot{l} = 0$).

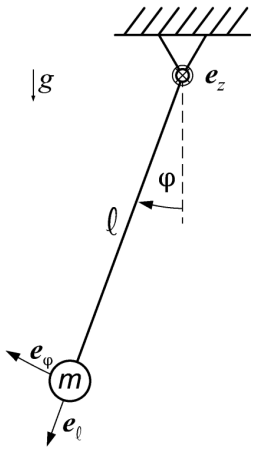

Figure 13: A simple fixed pendulum

Dynamic equations of the system shown in Fig. 13 can be written as follows:

$$\begin{cases} \ddot{\phi} + 2\frac{\dot{\phi}\dot{l}}{l} + \frac{g}{l}\sin\phi = 0 \\ \ddot{l} - \dot{\phi}^2 l + g(1-\cos\phi) + \frac{d}{m}(\dot{l} - \dot{l}_0) + \frac{c}{m}(l - l_0) = 0. \end{cases} \tag{101}$$

According to (101), the hoisting (l) and the sway channels (ϕ) are inherently coupled. Note that this coupling cannot be observed in the linearized equations shown in

$$\begin{cases} \ddot{\phi} + \frac{g}{l}\phi = 0 \\ \ddot{l} + \frac{d}{m}(\dot{l} - \dot{l}_0) + \frac{c}{m}(l - l_0) = 0. \end{cases} \tag{102}$$

According to [Bockstedte and Kreuzer, 2005], the coupling effect among the modes is dominant when the following condition is satisfied:

$$\sum k_i \omega_i \approx 0, \tag{103}$$

where k_i are integers and ω_i are the resonant frequencies of the system. This effect is called *autoparametric* or *internal resonance* [Nayfeh, 2000]. Following [Bockstedte and Kreuzer, 2005], this effect is amplified when the natural freuqncy of the lift (ω_{lift}) is twice the value of the natural frequency of the pendulation ω_{pend} as follows:

$$\omega_{\text{lift}} = 2\omega_{\text{pend}} \tag{104}$$

For the system shown in Fig. 13, these frequencies are as follows:

$$\begin{aligned} \omega_{\text{pend}} &= \sqrt{\frac{g}{l_0}} \\ \omega_{\text{lift}} &= \sqrt{\frac{c}{m} - \frac{d^2}{2m^2}}, \quad D_{\text{lift}} = \frac{1}{2}\frac{d}{\sqrt{mc}} \end{aligned} \tag{105}$$

Using (104) and (105) one has:

$$c = \frac{4m}{1-2D^2}\frac{g}{l_0}, \qquad d = 2\sqrt{mc}D \tag{106}$$

Hence, a closed-loop controller, based on the pole placement, has been designed to emulate a cable with such damping (d) and flexibility (c) parameters. while tracking the desired length (l_0).

Another interesting study has been conducted by [Moustafa, 1994] where a linearized time-varying model is developed where the input length and the trolley position are the inputs and the sway angle is the output.

6.8 Summary of all methods

A summary of all methods used for control purposes are listed in Tables 3 to 10. The nomenclature corresponding to these tables are provided in Table 2.

Table 2: Nomenclature

Feedback (feed)	O: open-loop, C: collocated, N: noncollocated
Scenario (sce.)	R: regulation, T: tracking
Stability (stab.)	GE: global exponential, LE: local exponential, GA: global asymptotic GF: global finite-time, LA: local asymptotic, LF: local finite-time N/A: not available
Validation (val.)	S: simulation, E: experiment, SE: both simulation and experiment
Control (cont.)	x: control trolley in one direction, x, y: control trolley in two direction l: control the cable's length, θ: just sway control
Number of cables (NC)	The indicated number is the number of cables R and F stands for rigid and flexible link

Table 3: Summary of the control methods in 2D space for the lumped single-pendulum

Reference	Feed	Sce.	Stab.	Val.	Cont.	Control method
[Park et al., 2007]	N	T	GE	SE	x	Sliding-mode control
[Chen et al., 2020]	N	T	GA	S	x	Sliding-mode control
[Kuo-Kai Shyu et al., 2005]	N	T	GA	S	x	Sliding-mode control
[Hamdy et al., 2018]	N	T	LA	S	x	Partial feed. lin. + deadbeat
[Fang et al., 2012]	N	T	GA	S	x	Lyapunov der. + adap. frict. comp.
[Lee et al., 1997]	C	R	LA	E	x	PID
[Lee, 2004]	N	T	GA	S	x, l	Sliding-mode control
[Fliess et al., 1991]	N	T	N/A	S	x, l	Flatness
[Lee et al., 2006]	N	T	GA	E	x, l	Sliding-mode control
[Alhazza et al., 2016]	O	-	N/A	SE	x	Input-shaping
[Chen et al., 2016]	N	R	N/A	SE	x	MPC
[He et al., 2014]	N	T	LA	S	x	Feedback lin. + adaptive law
[Sun et al., 2015]	C	R	GA	SE	x, l	Lyapunov derived adaptive law
[Abdullahi et al., 2018]	O	-	N/A	E	x	Input-shaping
[Ngo and Hong, 2012]	N	T	GA	SE	x	Sliding-mode control
[Moon et al., 2013]	N	T	GA	SE	x, l	SMC with parameter estimation
[Park et al., 2014]	N	T	GA	S	x	SMC + fuzzy uncertainty estimation
[Sano et al., 2010]	C	T	N/A	SE	x	Obs.-based time-delay tolerant PI
[Yi et al., 2003]	N	R	LE	S	x	State-feedback + fuzzy traj. generator
[Park et al., 2008]	N	T	GA	SE	x	SMC + fuzzy compensator
[Ohnishi et al., 1981]	N	R	N/A	S	x	Linear state feedback
[Collado et al., 2000]	C	R	GA	S	x	PD control
[Omar, 2003]	N	T	LA	SE	x	PD - fuzzy - time-delayed
[Zhang et al., 2017b]	N	R	Lya.	S	x, l	Flatness control
[Diwold et al., 2022]	N	T	LE	E	x, l	Discrete-time flatness control
[Hong et al., 2003]	O	-	N/A	S	x	Input-shaping
[Singhose et al., 2000]	O	-	N/A	SE	x	Input-shaping with hoisting
[Wu and He, 2015]	N	R	LA	S	x	Lyapunov derived
[Zhang et al., 2017a]	N	R	GA	SE	x	Lyapunov derived
[Moustafa, 1994]	N	T	LA	S	θ	Linear feedback (x, l are inputs)
[Zhang, 2019]	N	T	GF	SE	x	Terminal SMC
[Fliess et al., 1995]	O	-	N/A	S	x	Flatness control
[Kimiaghalam et al., 1999]	N	T	N/A	S	x, l	Linear feedforward + GA generated traj.

Table 4: Summary of the control methods in 2D space for the lumped single-pendulum (continued)

Reference	Feed	Sce.	Stab.	Val.	Cont.	Control method
[Wang et al., 2021a]	N	Sce.	GA	S	x, l	SMC
[Qian and Yi, 2016]	N	R	Asymptotic	S	x	SMC
[Zhang et al., 2020]	N	R	GA	E	x	Lyapunov derived
[Singhose et al., 1997]	O	-	N/A	S	x	Input-shaping
[Zhang et al., 2014]	O	-	N/A	SE	x	Dynamic programming
[Shao et al., 2020]	N	R	LA	S	x	LMI design based on fuzzy model
[Fatehi et al., 2014]	N	T	LA	S	x	Linear state feedback
[Wu et al., 2015]	N	R	N/A	S	x	MPC
[Sun and Fang, 2012]	N	R	GA	SE	x	Lyapunov derived
[Fang et al., 2001]	N	R	GA	S	x	Lyapunov derived
[Yu et al., 1995]	N	T	LA	S	x	Approx. feedback linearization + LQR
[Sun and Fang, 2014]	N	T	GA	SE	x, l	Lyapunov derived
[Piazzi and Visioli, 2002]	C	T	N/A	S	x	Observer-based linear state-feedback
[Wu and Xia, 2014]	O	-	N/A	S	x	Offline trajectory design
[Chen et al., 2016]	N	T	GE	SE	x	Feedback linearization + flatness
[Bartolini et al., 2003]	C	T	N/A	SE	x, l	SMC
[Le et al., 2014]	N	T	GA	SE	x, l	partial feedback linearization + SMC
[Smoczek and Szpytko, 2017]	N	T	N/A	E	x	PSO model identification + MPC
[Aschemann, 2009]	N	T	N/A	E	x, l	Observer-based IDA-PBC
[Chunshien Li et al., 2004]	C	T	N/A	S	x	Neuro-fuzzy system
[Karkoub and Zribi, 2001]	N	R	N/A	S	x, l	SMC, μ synthesis, state-feedback
[Hičár and Ritók, 2006]	C	R	LA	SE	x, l	State-observer based classic linear
[Bartolini et al., 2002]	N	T	GA	S	x, l	SMC
[Singhose et al., 1990]	O	-	N/A	S	x	Input-shaping
[Vyhlídal et al., 2013]	O	-	N/A	S	x	Input-shaping
[Lu et al., 2017]	N	T	GA	SE	x	Disturbance observer based SMC
[Kolonic et al., 2006]	N	R	LA	SE	x	Convex combination of LTI systems
[Auernig and Troger, 1987]	O	-	N/A	S	x, l	Optimal control (Pontryagin's principle)
[Manson, 1982]	O	-	N/A	S	x	Optimal control
[Peng et al., 2012]	C	R	N/A	SE	x	PD control

Table 5: Summary of the control methods in 2D space for the lumped-mass double-pendulum

Reference	Feed	Sce.	Stab.	Val.	Cont.	Control method
[Ouyang et al., 2019]	N	T	GF	SE	x	Sliding-mode control
[Chen et al., 2019]	N	R	GA	E	x	Lyapunov derived
[Wang et al., 2021b]	N	R	GA	S	x	Sliding-mode control
[Zhang et al., 2016]	N	T	GA	E	x	Lyapunov der. + adap. param. estim.
[Vaughan et al., 2010]	O	-	N/A	SE	x	Input-shaping
[Sun et al., 2017]	N	R	GA	E	x	Lyapunov der. output feedback
[Sun et al., 2018]	O	-	N/A	SE	x	Dynamic programming
[Vaughan et al., 2010]	O	-	N/A	SE	x	Input-shaping
[Ouyang et al., 2019a]	C	T	LA	SE	x	PID control + S-shaped trajectory
[Li et al., 2022]	N	R	GA	E	x, l	SMC with Adaptive fuzzy law
[Hong et al., 2003]	O	-	N/A	S	x	Input-shaping
[Tang and Huang, 2016]	O	-	N/A	SE	x	Input-shaping for distributed mass
[Zhao and Gao, 2012]	N	R	N/A	SE	x	Input-shaping for distributed mass
[Qian and Yi, 2016]	N	R	Asymptotic	S	x	SMC
[Singhose et al., 2008]	O	-	N/A	SE	x	Input-shaping
[Sun et al., 2018]	N	R	GA	E	x	Adaptive Lyapunov derived
[Ouyang et al., 2019b]	N	T	GA	E	x	SMC with adaptive pole surface
[Khorshid and Al-Fadhli, 2021]	O	-	N/A	SE	x	Input-shaping for sloshing payload
[Weiping et al., 2004]	C	R	GA	S	x	PD control
[Shi et al., 2022]	C	R	GA	SE	x, l_1	PBC
[Tuan and Lee, 2013]	N	R	GA	S	x	SMC
[Sun et al., 2019]	N	R	GA	E	x	Quasi-PID

Table 6: Summary of the control methods in 2D space for flexible single-pendulum model

Reference	Feed	Sce.	Stab.	Val.	Cont.	Control method
[d' Andréa-Novel and Coron, 2000]	N	R	LE	S	x	Lyapunov derived
[d'Andréa Novel et al., 1994]	N	R	LA	S	x	Lyapunov derived
[d'Andréa Novel et al., 2019]	N	R	LF	S	x	Lyapunov derived
[Shen and Caverly, 2020]	N	R	LA	E	x, l	PBC with Ritz discretization
[Sun et al., 2019]	C	R	GA	E	x	Joint stiffness + Lyapunov derived
[Chentouf and Han, 2020]	N	R	LA	S	x	Lyapunov derived with extra actuators
[Alli and Singh, 1998]	C	T	LA	S	x	PBC
[Shen et al., 2021]	C	R	LA	SE	x, l	Adaptive PBC
[d'Andréa Novel and Coron, 2002]	N	R	LA	S	x, l	Boundary Lyapunov derived controller
[Cui and Zheng, 2019]	N	R	LA	S	x	Lyapunov derived

Table 7: Summary of the control methods in 3D space for the lumped single-pendulum with rigid link

Reference	Feed.	Sce.	Stab.	Val.	Cont.	Control method
[Wu and He, 2017]	N	R	GA	SE	x, y	Lyapunov derived
[Tuan et al., 2014]	N	R	GA	SE	x, y, l	Partial feedback linearization
[Tuan et al., 2012]	N	R	LA	SE	x, y, l	Partial feedback linearization
[Lee et al., 2013]	N	R	LA	S	x, y, l	Partial feedback linearization
[Sun et al., 2013]	N	R	GA	E	x, y	Lyapunov derived
[Chwa, 2009]	N	T	GA	S	x, y	Lyapunov derived
[Wu and He, 2016]	N	T	GA	SE	x, y	Partial feedback linearization
[Chwa, 2017]	N	R	GA	S	x, y	Sliding-mode control
[Knierim et al., 2010]	N	T	GA	E	x, y, l	Flatness
[Lee and Cho, 2001]	C	T	N/A	E	x, y, l	Fuzzy
[Yang and Yang, 2006]	C	R	GA	E	x, y	Lyapunov derived adap. param. est.
[Zhang et al., 2018]	N	T	GA	SE	x, y	Lyapunov derived.
[Maghsoudi et al., 2017]	O	-	N/A	SE	x, y	PSO optimized input-shaping
[Maghsoudi et al., 2016]	C	R	N/A	SE	x, y	optimized PID with PSO
[Toxqui et al., 2006]	N	R	LA	E	x, y	PID + neural compensator
[Garrido et al., 2008]	C	R	N/A	E	x, y	PID + command-shaping
[Xi and Hesketh, 2010]	C	R	LA	SE	x, y	Discrete-time integral SMC
[Chen et al., 2005]	N	T	GA	S	x, y, l	Partial feedback linearization
[Hong and Ngo, 2012]	-	-	N/A	SE	-	Kinematic of ship-mounted cranes
[Lee et al., 2014]	N	T	N/A	E	x, y	adaptive fuzzy SMC + visual feedback
[Ebeid et al., 1992]	N	T	LE	S	x, y, l	Classic linear control + motor dynamics
[Schindele and Aschemann, 2011]	N	T	N/A	E	x, y	MPC
[Bartolini et al., 2000]	N	T	LA	E	x, y	SMC
Lee [1998]	C	T	LA	E	x, y, l	Classic linear control
[Fang et al., 2003]	N	R	GA	S	x, y	Lyapunov derived
[Fang et al., 2001]	N	R	GA	SE	x, y	Lyapunov derived
[Al-Garni et al., 1995]	N	T	N/A	S	x, y, l	Linear state feedback
[Chen and Saif, 2008]	N	T	GA	E	x, y, l	Back-stepping + exact differentiators
[Vázquez et al., 2014]	N	T	GA	SE	x, y, l	SMC (coupling as disturbance)
[Chang and Chiang, 2008]	N	R	N/A	E	x, y	Fuzzy control
[Lin et al., 2012]	N	T	GA	E	x, y	TSMC + adaptive fuzzy tuning
[Yoshida and Tabata, 2008]	N	R	N/A	E	x, y	Optimal control

Table 8: Summary of the control methods in 3D space for the lumped double-pendulum with rigid link

Reference	Feed.	Sce.	Stab.	Val.	Cont.	Control method
[Zhao et al., 2021]	N	T	GA	E	x, y, l	Adaptive Lyapunov derived
[Ouyang et al., 2021]	N	R	GA	SE	x, y	Lyapunov derived

Table 9: Summary of the control methods in 2D space for multi-cable models

Reference	Feed	Sce.	Stab.	Val.	NC	Cont.	Control method
[Kim et al., 2004]	N	R	LE	E	4R	x	Linear state-feedback
[Yoon et al., 2014]	O	-	N/A	SE	2F	x	Input-shaping
[Yoon et al., 2010]	O	-	N/A	SE	2F	x	Input-shaping
[Nayfeh et al., 2005]	C	T	N/A	S	2R	x	LQR time-delayed and classic linear
[Nayfeh and Baumann, 2008]	N	R	LE	S	2R	θ	Control θ when x is input
[Lu et al., 2018]	N	R	GA	E	2R	x	Lyapunov derived

Table 10: Summary of the control methods in 3D space for multi-cable models

Reference	Feed	Sce.	Stab.	Val.	NC	Cont.	Control method
[Klaassens et al., 1999]	C	R	N/A	S	4R	x, l	classic linear
[Arena et al., 2015]	-	-	N/A	SE	4RF	-	kinematic modeling
[Morrish et al., 1997]	-	-	N/A	S	4R	-	kinematic modeling
[Ngo et al., 2008]	C	R	N/A	S	4R	x	Kinematic + skew control
[Ngo and Hong, 2012]	N	T	GA	S	6R	x	SMC
[Arena et al., 2013]	-	-	N/A	S	4RF	-	kinematic modeling

Table 11: A list of the review papers in the literature

[Ramli et al., 2017]	Review of several control methods for single and double-pendulum systems in 2D space
[Hong and Shah, 2019]	Review of control methods for several models in 2D and 3D spaces
[Bonnabel and Claeys, 2020]	Survey on flatness control

7 Comparisons of the controllers implemented for 2D space (trolley moves on a line)

Some numerical simulations have been conducted to investigate the general behavior of the controllers in 2D and 3D operating spaces. The specifications of the controllers as well as the nominal parameters of the overhead crane are summarized in Tables 12 and 13, respectively.

Table 12: Overview of the controllers. (S: single-pendulum, D: double-pendulum, I:infinite dimensional)

Controller	Feedback	Number of parameters	scenario	Required sensors
Unshaped input	open-loop	-	-	-
ZV	open-loop	-	-	-
ZVD	open-loop	-	-	-
Collocated PD	collocated	2	regulation	2
Noncollocated Quasi-PID	noncollocated (D)	4	regulation	4
Noncollocated PD	noncollocated (S)	3	regulation	4
Collocated PD tracking	noncollocated (D)	5	tracking	2
PD-PD	noncollocated (I)	3	regulation	4
SMC single-pendulum	noncollocated (S)	6	regulation	4
SMC double-pendulum	noncollocated (D)	5	regulation	6
PD energy	noncollocated (S)	6	regulation	5
Coupling tracking	noncollocated (S)	3	tracking	3

Table 13: Parameters of the simulation

number of cables	8
cart mass	10T
hook mass	13.6T
maximum payload mass	40T
distance between the hook and the payload	1
number of pendulum (including the hook and the payload)	20
damping coefficient for the joints	0.2×8 (NM/(deg/s))
joint flexibility	0.1×8 NM/deg
Maximum distance between the trolley and the payload	10m
controller sampling time	50ms
simulation time	100s
measurement delay	100ms

Some objective functions are defined for the ease of comparison as shown in Table 14.

Table 14: Objective functions

$e_p = x_p - x_d$	Payload position error
$e_c = x_c - x_d$	Cart position error
$\tilde{L}_2(X) = 10^3 L_2(X)/\text{length}(X)$	$\tilde{L}_2$ norm
$\bar{L}_2(X) = 10^5 L_2(X)/\text{length}(X)$	$\bar{L}_2$ norm
$\tilde{L}_\infty(X) = 10^3 L_\infty(X)$	$\tilde{L}_\infty$ norm
$e_a(t) = \sum_{i=1}^{n} \lvert\theta_i(t)\rvert$	Summation of sway angles
t_s	For all $t > t_s$ one has $\lvert\theta_1(t)\rvert + \lvert\theta_n(t)\rvert < 0.1°$
t_{cs}	For all $t > t_{cs}$ one has $\lvert\theta_1(t)\rvert + \lvert\theta_n(t)\rvert < 0.1°$, $\lvert\dot{x}(t)\rvert < 3.5 \times 0.02$ and $\lvert x(t) - x_d\rvert < 0.1$. Note that for all $t > t_{cs}$, $u(t) = 0$ and breaks stop the trolley and the hoisting mechanism.

Note that $\theta_n(t)$ is the last angle (payload sway).

7.1 The studied control strategies

The control methods used in the numerical simulations are briefly introduced below:

7.1.1 Input-shaping strategy (unshaped input, ZV, ZVD)

Input-shaping is an open-loop method where the control signal is generated in an offline manner to reduce the sway angle. Assuming that the desired acceleration of the payload is $a_d(t)$, considering the whole crane as a point mass system, the nominal required force applied to the trolley can be calculated using the Newton's formula as follows:

$$F(t) = m_t a_d(t) \tag{107}$$

where $F(t)$ is the control force applied to the trolley, and m_t is the total mass of the system including the trolley, cables, the hook and the payload. Since this force has been calculated without considering the load sway, it can lead to severe load oscillations. To solve this problem, several types of input-shaping methods has been developed in the literature. Among them, ZV (zero vibration) and ZVD (zero vibration derivative) approaches are probably the most well-know ones. In these methods, instead of applying the control force (107) directly, its integral convolution with a few number of impulses A_i at time steps t_i, $i = 0, 1, \ldots, n$ is calculated and applied to the trolley, where for ZV and ZVD one has $n = 1$, $n = 2$, respectively. These impulses can be calculated for ZV and ZVD using (108) and (109), respectively, as follows [Hong and Shah, 2019]:

$$\begin{bmatrix} A_1 & A_2 \\ t_1 & t_2 \end{bmatrix} = \begin{bmatrix} \frac{1}{k+1} & \frac{k}{k+1} \\ 0 & \frac{\pi}{\omega_d} \end{bmatrix} \tag{108}$$

$$\begin{bmatrix} A_1 & A_2 & A_3 \\ t_1 & t_2 & t_3 \end{bmatrix} = \begin{bmatrix} \frac{1}{(k+1)^2} & \frac{2k}{(k+1)^2} & \frac{k^2}{(k+1)^2} \\ 0 & \frac{\pi}{\omega_d} & \frac{2\pi}{\omega_d} \end{bmatrix} \tag{109}$$

where ω_d is the damping frequency and can be calculated by modeling of the whole system as an LTI second-order dynamical system which may not be realistic enough. In this study, ω_d is considered as a design parameter which is obtained based on trial and error such that the steady-state load oscillations are minimized.

7.1.2 Collocated PD - regulation

This is a well-known control strategy which has been analyzed in several references (see for example [Sun and Fang, 2012, Chen et al., 2019] for the stability proof). In this scheme, the control force is calculated as follows:

$$u(t) = k_p e_x(t) + k_d e_v(t) \tag{110}$$

where $e_x = x(t) - x_d$ and $e_v = v(t) - v_d$, respectively. This controller has two parameters $k_p \in \mathbb{R}^+$ and $k_d \in \mathbb{R}^+$.

The control law is obtained for the single-pendulum system based on the following energy function:

$$E = \frac{1}{2}\dot{q}^\intercal M \dot{q} + mgl(1 - \cos). \tag{111}$$

where q is the vector of generalized coordinates, M is the mass matrix, θ is the sway angle, and l is the length of the link. Note that (111) is composed of the kinetic $\frac{1}{2}\dot{q}^\intercal M \dot{q}$ and potential $mgl(1-\cos)$ energies of the single-pendulum system. Time derivative of (111) gives:

$$\dot{E} = \dot{x}F \tag{112}$$

7.1.3 Noncollocated quasi-PID - regulation

This controller has been borrowed from [Sun et al., 2019]. The control law is calculated as follows:

$$\begin{aligned} F = &-k_p \tanh(e_x) - k_d \tanh(e_v) - k_{\phi 1} \tanh^2(\dot{\theta}_1) \tanh(e_v) - k_{\phi 2} \tanh^2(\dot{\theta}_2) \tanh(e_v) - \\ &k_i \tanh\left(\lambda^2 e_x + \lambda \textstyle\int_0^t \tanh(e_x) dt\right), \end{aligned} \tag{113}$$

where $e_x(t) = x(t) - x_d$, and $e_v(t) = v(t) - v_d$ and k_p, k_d, k_i, $k_{\phi 1}$, $k_{\phi 2}$, λ are six positive real parameters of this controller which are designed as following inequalities:

$$\begin{aligned}
&k_p + k_d + k_{\phi 1} + k_{\phi 2} + k_i \leq u_M \\
&k_p - \tfrac{k_d d_x + (k_{\phi 1} + k_{\phi 2} + d_x)^2}{\lambda d_x} > 0 \\
&\lambda > \max \left\{ \begin{array}{c} \frac{d_2}{\underline{m}_2 g \underline{l}_2}, \\ \frac{d_1}{(\underline{m}_1 + \underline{m}_2) g \underline{l}_1}, \\ \frac{\gamma_m}{\sqrt{2\gamma_m \alpha}}, \\ \frac{4\gamma_m + 2(\overline{m}_1 + \overline{m}_2)\bar{l}_1 + 2\overline{m}_2 \bar{l}_2}{3 d_x}, \\ \frac{4\gamma_m + \overline{m}_2 \bar{l}_2 + 2\sqrt{2\overline{m}_2 \bar{l}_1 \bar{l}_2}}{3 d_2}, \\ \frac{4\gamma_m + (\overline{m}_1 + \overline{m}_2)\bar{l}_1 + 2\sqrt{2\overline{m}_2 \bar{l}_1 \bar{l}_2}}{3 d_1} \end{array} \right\}
\end{aligned} \tag{114}$$

where $\alpha \triangleq \min\{(\underline{m}_1 + \underline{m}_2) g \underline{l}_1, \underline{m}_2 g \underline{l}_2, (1/2) k_p\}$, $|u| \leq u_M$, u_M is the control saturation constant, $\overline{(\cdot)}$ and $\underline{(\cdot)}$ indicate maximum and minimum values of the uncertain parameter $(\cdot)$, d_x, d_1 and d_2 indicate the frictions (damping) on the trolley, first and second joints. Moreover, γ_m and γ_M satisfy the following inequality:

$$\gamma_m ||\dot{q}||^2 \leq \dot{q}^\intercal M(q) \dot{q} \leq \gamma_M ||\dot{q}||^2, \tag{115}$$

where $M(q)$ is the mass matrix and q is the vector of generalized coordinates.

The following energy function is considered to design this controller for the double-pendulum system:

$$\begin{aligned}
&E = \tfrac{1}{2} \dot{q}^\intercal M(q) \dot{q} + (m_1 + m_2) g L_1 (1 - \cos(\theta_1)) + m_2 g L_2 (1 - \cos(\theta_2)) + k_p \ln[\cosh(e)] + \tfrac{1}{\lambda} \nu^\intercal M(q) \dot{q} \\
&+ \frac{1}{\lambda^2} \int_0^\delta k_i \tau \cosh^2(\zeta) d\tau \\
&\zeta = \lambda^2 e + \lambda \int_0^t \tanh(e) d\tau \\
&\delta = \tanh(\zeta) \\
&\nu = \begin{bmatrix} \tanh(e) & \sin(\theta_1/2) & \sin(\theta_2/2) \end{bmatrix}^\intercal
\end{aligned} \tag{116}$$

7.1.4 Noncollocated PD regulation

This method is basically designed for the single-pendulum system [Sun and Fang, 2012]. The control law can be synthesized as follows:

$$F(t) = -k_p \big(e_x(t) - k_a \sin(\theta(t))\big) - k_d \big(e_v(t) - k_a \dot{\theta}(t) \cos(\theta)\big) \tag{117}$$

where $k_p \in \mathbb{R}^+$, $k_d \in \mathbb{R}^+$, $k_a \in \mathbb{R}^+$ are three parameters (See [Sun and Fang, 2012] for the stability proof). To implement this controller on multiple-pendulum systems, the first and the last sway angles are fed as the feedback (θ) in two different implementations. This controller has been designed for the single-pendulum

syystem using the following energy function:

$$
\begin{aligned}
&E(t) = \tfrac{1}{2}\dot{q}^{\intercal} H(q)\dot{q} + \big(m_1 l + k_a(m+m_1)\big)g(1-\cos(\theta)) \\
&H = \begin{bmatrix} m+m_1 & m_1 l\cos(\theta) \\ m_1 l\cos(\theta) & k_a(m+m_1\sin^2(\theta))l + m_1 l^2 \end{bmatrix}
\end{aligned} \tag{118}
$$

7.1.5 Collocated PD tracking

This controller was proposed in [Sun and Fang, 2014] as follows:

$$
F(t) = -k_p e_x(t) - \frac{2\lambda\xi^2}{\xi^2 - e_x^2(t)} e_x(t) - k_d e_v(t) + (m+m_1)a_d - \phi\,\mathrm{sgn}(e_v(t)), \tag{119}
$$

where k_p, k_d, λ, ξ, ϕ are positive real parameters. Note that in this controller one has $|e_x(t)| < \phi$. Compared to the regulation controllers, the acceleration reference profile has been appeared in the control law. Moreover, it can be seen from (119) that for $e_x = \pm\xi$ the control might be singular. Note that this controller has been designed for the single-pendulum system with variable length link using the following energy function:

$$
\begin{aligned}
&E = E_e + E_\omega \\
&E_e = \tfrac{1}{2}\dot{e}^{\intercal} M_c(q)\dot{e} + \tfrac{1}{2}k_{px}e_x^2 + \tfrac{1}{2}k_{pl}e_l^2 + mgl(1-\cos(\theta)) \\
&E_\omega = \lambda_{\omega x}\frac{e_x^2}{\zeta_x^2 + e_x^2} + \lambda_{\omega l}\frac{e_l^2}{\zeta_l^2 + e_l^2} \\
&M_c = \begin{bmatrix} m+m_1 & m_1\sin(\theta) & m_1 l\cos(\theta) \\ m_1\sin(\theta) & m_1 & 0 \\ m_1 l\cos(\theta) & 0 & m_1 l^2 \end{bmatrix}
\end{aligned} \tag{120}
$$

In fact, in this method, the system has been considered as a multiple-input multiple-output plant with actuation on the trolley and the winch. The notation is the same as the ones defined for the (119) and Subscripts x and l correspond to the channels of the trolley position and the cable length. For the control law (119) the parameters have been used without subscripts x and the notation l for the winch has been neglected.

7.1.6 PD-PD

The original form of this controller has been introduced as follows [d'Andréa Novel et al., 2019]:

$$
F(t) = -K^{-1}\big(\dot{\theta}(t) + k_1 e_v(t)\big) - \mu\Big(e_v(t) + K^{-1}\big(\theta(t) + k_1 e_x(t)\big)\Big), \tag{121}
$$

where $k_1 \in \mathbb{R}^+$, $K \in \mathbb{R}^+$ and $\mu > K/2$ are the parameters. To make the tuning procedure more convenient, (121) is rewritten as follows:

$$
F(t) = -K^{-1}\dot{\theta}(t) - K^{-1}k_1 e_v(t) - \mu e_v(t) - \mu K^{-1}\theta(t) - \mu k_1 K^{-1} e_x(t). \tag{122}
$$

Hence,

$$F(t) = -\mu k_1 K^{-1} e_x(t) - (K^{-1}k_1 + \mu)e_v(t) - \mu K^{-1}\theta(t) - K^{-1}\dot{\theta}(t). \tag{123}$$

Equation (123) is rewritten as follows:

$$F(t) = -\alpha_1 e_x(t) - \alpha_2 e_v(t) - \alpha_3 \theta(t) - \alpha_4 \dot{\theta}(t). \tag{124}$$

In this form, this controller has three tuning parameters $\alpha_1, \alpha_2, \alpha_3$. Subsequently, α_4 can be calculated as $\alpha_4 = \dfrac{\alpha_2\alpha_3 - \alpha_3\left(\dfrac{\alpha_2}{2} + \dfrac{\sqrt{\alpha_2^2 + 4\alpha_1}}{2}\right)}{\alpha_1}$. Since the optimization algorithms may not be able to handle the constraints, it is assumed that $\alpha_1, \alpha_2, \alpha_3$ are positive real parameters.

Since the control law has been obtained based on the linearized model, a Lyapunov function has not been explicitly defined and stability tools derived from the Lyapunov theory for the linearized systems have been used for the stability proof.

7.1.7 Sliding-mode control

The sliding-mode controllers implemented in this project has been obtained from [Qian and Yi, 2016, Tuan and Lee, 2013] where the SMCs have been developed for the single [Qian and Yi, 2016] and double [Tuan and Lee, 2013] pendulum systems. Following [Qian and Yi, 2016], the dynamic model of the single-pendulum system can be rewritten as follows:

$$\begin{cases} \dot{x}_1 = x_2 \\ \dot{x}_2 = f_1(x) + b_1(x)u \\ \dot{x}_3 = x_4 \\ \dot{x}_4 = f_2(x) + b_2(x)u \end{cases} \tag{125}$$

where $x = [x_1, x_2, x_3, x_4]^\intercal$, $x_1 = x$, $x_2 = \dot{x}$, $x_3 = \theta_1$, $x_4 = \dot{\theta}_1$. Moreover,

$$\begin{aligned} f_1(x) &= \frac{mLx_4^2 \sin(x_3) + m_1 g \sin(x_3)\cos(x_3)}{m + m_1 \sin^2(x_3)} \\ b_1(x) &= \frac{1}{m + m_1 \sin^2(x_3)} \\ f_2(x) &= \frac{(m+m_1)g\sin(x_3) + m_1 L x_4^2 \sin(x_3)\cos(x_4)}{(m + m_1\sin^2(x_3))L} \\ b_2(x) &= \frac{\cos(x_3)}{(m + m_1\sin^2(x_3))L}, \end{aligned} \tag{126}$$

where m and m_1 are the masses of the trolley and the payload, respectively, and L is the cable's length.

The double pendulum system can be rewritten as follows:

$$\begin{cases} \dot{x}_1 = x_2 \\ \dot{x}_2 = f_1(x) + b_1(x)u \\ \dot{x}_3 = x_4 \\ \dot{x}_4 = f_2(x) + b_2(x)u \\ \dot{x}_5 = x_6 \\ \dot{x}_6 = f_3(x) + b_3(x)u \end{cases} \tag{127}$$

where $x = [x_1, x_2, x_3, x_4, x_5, x_6]^\intercal$, $x_1 = x$, $x_2 = \dot{x}$, $x_3 = \theta_1$, $x_4 = \dot{\theta}_1$, $x_5 = \theta_2$, and $x_6 = \dot{\theta}_2$. Moreover, $f_i(x) = \Gamma_i/\Delta$ and $b_i(x) = T_i/\Delta$, and

$$\begin{aligned}
&\Delta = (m_1+m_2)m_2 l_1^2 l_2^2\big[(m_0+m_1+m_2) - (m_1+m_2)\cos^2(x_3)\big] \\
&-m_2^2 l_1^2 l_2^2\big[(m_1+m_2)\cos^2(x_5) + (m_0+m_1+m_2)\cos^2(x_3-x_5) - 2(m_1+m_2)\cos(x_3)\cos(x_5)\cos(x_3-x_5)\big] \\
&\\
&\Gamma_1 = \big[(m_1+m_2)m_2 l_1^2 l_2^2 - m_2^2 l_1^2 l_2^2\cos^2(x_3-x_5)\big]\big[(m_1+m_2)l_1 x_4^2\sin(x_3) + m_2 l_2 x_6^2\sin(x_5)\big] + \\
&\big[(m_1+m_2)m_2 l_1 l_2^2\cos(x_3) - m_2^2 l_1 l_2^2\cos(x_5)\cos(x_3-x_5)\big]\big[m_2 l_1 l_2 x_6^2\sin(x_3-x_5) + (m_1+m_2)g l_1\sin(x_3)\big] + \\
&\big[(m_1+m_2)m_2 l_1^2 l_2\cos(x_5) - m_2 l_1^2 l_2\cos(x_3)\cos(x_3-x_5)\big]\big[-m_2 l_1 l_2 x_4^2\sin(x_3-x_5) + m_2 g l_2\sin(x_5)\big] \\
&\\
&T_1 = (m_1+m_2)m_2 l_1^2 l_2^2 - m_2^2 l_1^2 l_2^2\cos^2(x_3-x_5) \\
&\\
&\Gamma_2 = \big[m_2^2 l_1 l_2^2\cos(x_3-x_5) - (m_1+m_2)m_2 l_1 l_2^2\cos(x_3)\big]\big[(m_1+m_2)l_1 x_4^2\sin(x_3) + m_2 l_2 x_6^2\sin(x_5)\big] + \\
&\big[m_2^2 l_2^2\cos^2(x_5) - (m_0+m_1+m_2)m_2 l_2^2\big]\big[m_2 l_1 l_2 x_6^2\sin(x_3-x_5) + (m_1+m_2)g l_1\sin(x_3)\big] + \\
&\big[(m_0+m_1+m_2)m_2 l_1 l_2\cos(x_3-x_5) - (m_1+m_2)m_2 l_1 l_2\cos(x_3)\cos(x_5)\big]\big[-m_2 l_1 l_2 x_4^2\sin(x_3-x_5) + \\
&m_2 g l_2\sin(x_5)\big] \\
&\\
&T_2 = m_2^2 l_1^2 l_2^2\cos(x_5)\cos(x_3-x_5) - (m_1+m_2)m_2 l_1 l_2^2\cos(x_3) \\
&\\
&\Gamma_3 = \big\{(m_1+m_2)m_2 l_1^2 l_2\big[\cos(x_3)\cos(x_3-x_5) - \cos(x_5)\big]\big\}\big[(m_1+m_2)l_1 x_4^2\sin(x_3) \\
&+m_2 l_2 x_6^2\sin(x_5)\big] + \big[(m_0+m_1+m_2)m_2 l_1 l_2\cos(x_3-x_5) \\
&-(m_1+m_2)m_2 l_1 l_2\cos(x_3)\cos(x_5)\big]\big[m_2 l_1 l_2 x_6^2\sin(x_3-x_5) + (m_1+m_2)g l_1\sin(x_3)\big] \\
&+\big[(m_1+m_2)^2 l_1^2\cos^2(x_3) - (m_0+m_1+m_2)(m_1+m_2)l_1^2\big] \\
&\times[-m_2 l_1 l_2 x_4^2\sin(x_3-x_5) + m_2 g l_2\sin(x_5)] \\
&\\
&T_3 = (m_1+m_2)m_2 l_1^2 l_2\cos(x_3)\cos(x_3-x_5) - (m_1+m_2)m_2 l_1^2 l_2\cos(x_5),
\end{aligned} \tag{128}$$

where m_0, m_1, and m_2 are the masses of the trolley, hook and payload, respectively, l_1 and l_2 are the lengths of the first and second links, respectively.

Following [Qian and Yi, 2016], the control signal for the single-pendulum system is as follows:

$$\begin{cases} s = c_1(x_1 - x_d) + c_2(x_2 - v_d) + c_3 x_3 + c_4 x_4 \\ u_{eq} = -\dfrac{c_1(x_2 - v_d) + c_3 x_4 + c_2 f_1(x) + c_4 f_2(x)}{c_2 b_1(x) + c_4 b_2(x)} \\ u_{sw} = -\dfrac{\kappa s + \eta \operatorname{sgn}(s)}{c_2 b_1(x) + c_4 b_2(x)} \\ u = u_{eq} + u_{sw}. \end{cases} \tag{129}$$

Equation (129) may be implemented either using explicit or implicit discretization schemes. The explicit discretization is straightforward and is implemented as follows:

$$\begin{cases} s_k = c_1(x_{1,k} - x_d) + c_2(x_{2,k} - v_d) + c_3 x_{3,k} + c_4 x_{4,k} \\ u_{eq,k} = -\dfrac{c_1(x_{2,k} - v_d) + c_3 x_{4,k} + c_2 f_1(x_k) + c_4 f_2(x_k)}{c_2 b_1(x_k) + c_4 b_2(x_k)} \\ u_{sw,k} = -\dfrac{\kappa s_k + \eta \operatorname{sgn}(s_k)}{c_2 b_1(x_k) + c_4 b_2(x_k)} \\ u_k = u_{eq,k} + u_{sw,k}. \end{cases} \tag{130}$$

On the other hand, the implicit discretization may be used as follows:

$$\begin{cases} s_k = c_1(x_{1,k} - x_d) + c_2(x_{2,k} - v_d) + c_3 x_{3,k} + c_4 x_{4,k} \\ u_{eq,k} = -\dfrac{c_1(x_{2,k} - v_d) + c_3 x_{4,k} + c_2 f_1(x_k) + c_4 f_2(x_k)}{c_2 b_1(x_k) + c_4 b_2(x_k)} \\ u_{sw,k} \in -\dfrac{\kappa s_{k+1} + \eta \operatorname{sgn}(s_{k+1})}{c_2 b_1(x_k) + c_4 b_2(x_k)} \\ u_k = u_{eq,k} + u_{sw,k}. \end{cases} \tag{131}$$

As can be seen from (130), $u_{sw,k}$ depends on s_{k+1}. To calculate this variable at time-step k, one has:

$$\dot{s} \in -\kappa s - \eta \operatorname{sgn}(s) \tag{132}$$

For the implicit discretization:

$$\begin{aligned} & s_{k+1} \in -h\kappa s_{k+1} - h\eta \operatorname{sgn}(s_{k+1}) + s_k \rightarrow \\ & (1 + h\kappa) s_{k+1} \in -h\eta \operatorname{sgn}(s_{k+1}) + s_k \rightarrow \\ & s_{k+1} + b_k \in -\frac{h\eta}{1 + h\kappa} \operatorname{sgn}(s_{k+1}) \end{aligned} \tag{133}$$

$b_k = -\dfrac{s_k}{1 + h\kappa}$.

- **Case 1:** $b_k < -\dfrac{h\eta}{1+h\kappa}$:

  In this case, $\mathrm{sgn}(s_{k+1}) > 0$ and $s_{k+1} = -\dfrac{h\eta}{1+h\kappa} - b_k$.

- **Case 2:** $b_k \in [-\dfrac{h\eta}{1+h\kappa}, \dfrac{h\eta}{1+h\kappa}]$

  $\mathrm{s}_{k+1} = 0$ is obtained for this case. Therefore,

$$\begin{aligned} & b_k \in -\frac{h\eta}{1+h\kappa}\mathrm{sgn}(0) = -\frac{h\eta}{1+h\kappa}[-1,1] && \Leftrightarrow \\ & b_k = -\frac{h\eta}{1+h\kappa}\xi \qquad \text{for some } \xi \in [-1,1] && \Rightarrow \\ & \xi = -\frac{b_k(1+h\kappa)}{h\eta} = \frac{s_k}{h\eta}, \end{aligned} \tag{134}$$

  where ξ is called a selection of the set-valued signum function at zero. Substituting (134) into (131) one has

$$u_{sw,k} = \frac{s_k}{h(c_2 b_1(x_k) + c_4 b_2(x_k))} \tag{135}$$

  As can be seen, in this case, the parameters κ and η do not appear in the control law. This indicates the gain insensitivity of the implicit controller.

- **Case 3:** $b_k > \dfrac{h\eta}{1+h\kappa}$:

  In this case, $\mathrm{sgn}(s_{k+1}) < 0$ and $s_{k+1} = \dfrac{h\eta}{1+h\kappa} - b_k$.

For the double pendulum system the SMC is as follows:

$$\begin{aligned} & s = \dot{e} + \lambda e + \alpha x_3 + \beta x_5 \\ & u_{eq} = -(m_1+m_2) l_1 \cos(x_3)\dot{x_4} - m_2 l_2 \cos(x_5)\dot{x}_6 + (m_1+m_2) l_1 \sin(x_3) x_4^2 + m_2 l_2 \sin(x_5) x_6^2 \\ & -(m_0+m_1+m_2)(\lambda(x_2 - v_d) + \alpha x_4 + \beta x_6) \\ & u_{sw} = -k\,\mathrm{sgn}(s) \\ & u = u_{eq} + u_{sw}. \end{aligned} \tag{136}$$

where $e = x_1 - x_d$ and $\dot{e} = x_2$. For the stability proof of the continuous-time form one may refer to [Qian and Yi, 2016].

The explicit discretization of (136) is straightforward and is not addressed here. The implicit one can be

employed as follows:

$$
\begin{aligned}
&s_k = (v_k - v_d) + \lambda(x_k - x_d) + \alpha\theta_{1,k} + \beta\theta_{2,k}\\
&u_{eq,k} = -(m_1+m_2)l_1\cos(\theta_{1,k})\ddot{\theta}_{1,k} - m_2 l_2\cos(\theta_{2,k})\ddot{\theta}_{2,k} + (m_1+m_2)l_1\sin(\theta_{1,k})\dot{\theta}_{1,k}^2 + m_2 l_2\sin(\theta_{2,k})\dot{\theta}_{2,k}^2\\
&-(m_0+m_1+m_2)(\lambda(v_k - v_d) + \alpha\dot{\theta}_{1,k} + \beta\dot{\theta}_{2,k})\\
&u_{sw,k} \in -k\,\mathrm{sgn}(s_{k+1})\\
&u_k = u_{eq,k} + u_{sw,k}.
\end{aligned}
\tag{137}
$$

Note that $\dot{\theta}_{1,k}$ and $\dot{\theta}_{2,k}$ are the angular velocities of $\theta_{1,k}$ and $\theta_{2,k}$, respectively, which are assumed to be measurable. Furthermore, $\ddot{\theta}_{1,k}$ and $\ddot{\theta}_{2,k}$ are the time derivatives of $\dot{\theta}_{1,k}$ and $\dot{\theta}_{2,k}$, respectively which are calculated by a first-order linear differentiator as follows:

$$z_k = \frac{z_{k-1} + c(f_k - f_{k-1})}{1 + hc}, \tag{138}$$

where z_k is the differentiation of the input f_k, c is the pole of the filter, and h is the sampling time. The implicit discretization (137) gives:

$$s_{k+1} \in -\frac{hk}{m_0+m_1+m_2}\,\mathrm{sgn}(s_{k+1}) + s_k \tag{139}$$

This GE can be solved as follows with $b_k = -s_k$ and $a = \dfrac{hk}{m_0+m_1+m_2}$:

- **Case 1:** $b_k < -a$:

  In this case, $\mathrm{sgn}(s_{k+1}) > 0$ and $s_{k+1} = -a - b_k$.

- **Case 2:** $b_k \in [-a, a]$

  $\mathrm{s}_{k+1} = 0$ is obtained for this case. Therefore,

$$
\begin{aligned}
&b_k \in -a\mathrm{sgn}(0) = -a[-1,1] \qquad \Leftrightarrow\\
&b_k = -a\xi \qquad \text{for some } \xi \in [-1,1] \qquad \Rightarrow\\
&\xi = -\frac{b_k}{a},
\end{aligned}
\tag{140}
$$

  where ξ is called a selection of the set-valued signum function at zero. Substituting ξ in this case into $u_{sw,k}$ gives:

$$u_{sw,k} = \frac{(m_0+m_1+m_2)s_k}{h} \tag{141}$$

- **Case 3:** $b_k > a$:

  In this case, $\mathrm{sgn}(s_{k+1}) < 0$ and $s_{k+1} = a - b_k$.

Note that the energy function $E = \frac{1}{2}s^2$ has been used to obtain the SMC laws for both single and double pendulum systems.

7.1.8 PD energy

This controller has been borrowed from [Zhang et al., 2020] and is as follows:

$$\begin{cases} e_x = x - x_d \\ e_v = v - v_d \\ \chi = e_x + \lambda \sin(\theta) \\ \dot{\chi} = e_v + \lambda \cos(\theta)\dot{\theta} \\ \varepsilon = x + \lambda \sin(\theta) \\ u(t) = -k_d\dot{\chi} - k_p \tanh(\chi) - k_q \dfrac{(x_d+\zeta)^2 - \varepsilon^2 + \chi\varepsilon}{((x_d+\zeta)^2 - \varepsilon^2)^2}\chi. \end{cases} \tag{142}$$

This controller has five parameters $k_p, k_d, k_q, \lambda, \zeta$ that need to be tuned.

The following energy function has been considered to obtain the control law for the single-pendulum system:

$$\begin{aligned} E &= E + E_a + E_p \\ E_a &= \tfrac{1}{2}\lambda m_1 l(\cos(\theta)\dot{\theta})^2 - \tfrac{1}{2}\lambda(m+m_1)l\dot{\theta}^2 - \lambda(m+m_1)g(1-\cos(\theta)) \\ E_p &= k_p \ln(\cosh\chi) + \frac{k_q\chi^2}{2((x_d+\zeta)^2 - \varepsilon^2)} \end{aligned} \tag{143}$$

where E is the mechanical energy of the system.

7.1.9 Coupling tracking

This controller was introduced by [Zhang et al., 2018] for 3D space and constant length cable as follows:

$$\begin{cases} e_v = (v - v_d) \\ \zeta = e_v - \lambda \sin(\theta) \\ F = -k_d\zeta - k_p \int_0^t \zeta dt + m_t a_d + \lambda m_t \cos(\theta)\dot{\theta} \end{cases} \tag{144}$$

where m_t is the total mass of the system including, cart, cable, hook and the payload, and a_d is the reference acceleration. This controller has three tuning parameters k_p, k_d, λ. This controller has been designed for the 3D space using the following energy function:

$$E = \tfrac{1}{2}\zeta^\intercal M(q)\zeta + m_1 g l(1 - \cos(\theta_x)\cos(\theta_y)) + \tfrac{1}{2}k_{p1}(\int_0^t \zeta_x dt)^2 + \tfrac{1}{2}k_{p2}(\int_0^t \zeta_y dt)^2 \tag{145}$$

where the subscripts x and y corresponds to the x and y channels, which are neglected in (144).

7.1.10 Comparison of the controllers

Table 15: Structure of the controllers

Controller	feed-forward terms	proportional terms	derivative terms	integration terms	stability
Unshaped input	$+m_t a_d$	—	—	—	no proof
ZV	$+\text{conv}(m_t a_d, P_1)$	—	—	—	no proof
ZVD	$+\text{conv}(m_t a_d, P_2)$	—	—	—	no proof
Collocated PD	—	$+k_p e_x(t)$	$+k_d e_v(t)$	—	GA1 & GA2
Noncollocated Quasi-PID	—	$-k_p \tanh(e_x)$	$-k_d \tanh(e_v)$ $-k_{\phi 1} \tanh^2(\dot\theta_1) \tanh(e_v)$ $-k_{\phi 2} \tanh^2(\dot\theta_2) \tanh(e_v)$	$-k_i \tanh\left(\lambda^2 e_x + \lambda \int_0^t \tanh(e_x) dt\right)$	GA2
Noncollocated PD regulation	—	$-k_p\big(e_x(t) -k_a \sin(\theta(t))\big)$	$-k_d\big(e_v(t) -k_a \dot\theta(t) \cos(\theta)\big)$	—	GA1
Collocated PD tracking	$+m_t a_d$	$-k_p e_x(t)$ $-\dfrac{2\lambda\xi^2}{\xi^2 - e_x^2(t)} e_x(t)$	$-k_d e_v(t)$ $-\phi\, \text{sgn}(e_v(t))$	—	GA1
PD-PD	—	$-\alpha_1 e_x(t)$ $-\alpha_3 \theta(t)$	$-\alpha_2 e_v(t)$ $-\alpha_4 \dot\theta(t)$	—	LI
SMC single-pendulum	—	discontinuous combination of			GA1 & RM
SMC double-pendulum	—	proportional and derivative terms			GA2 & RM
PD energy	—	$-k_p \tanh(\chi) - k_q \chi \times \dfrac{(x_d+\zeta)^2 - \varepsilon^2 + \chi\varepsilon}{((x_d+\zeta)^2 - \varepsilon^2)^2}$	$-k_d \dot\chi$	—	GA1
Coupling tracking	$+m_t a_d$	$-k_p \int_0^t \zeta dt$	$-k_d \zeta + \lambda m_t \cos(\theta)\dot\theta$	—	GA1

GA1 and GA2 denote GA stability for the single- and double-pendulum systems, respectively.
LI indicates local stability based on the infinite dimensional model, and RM denotes robustness to matched uncertainties.

7.2 Trajectory profile

Two different trajectories have been employed to evaluate the performances of the controllers under regulation and tracking conditions as shown in Fig. 14. The regulation trajectory is calculated as follows:

$$\begin{cases} x_d(t) = 3.5t^2/8 + 1 & 0 \le t \le 4 \\ x_d(t) = 3.5t - 6 & 4 < t < 8 \\ x_d(t) = -3.5t^2/8 + 10.5t - 34 & 8 \le t \le 12 \\ x_d(t) = 29 & t > 12 \end{cases} \tag{146}$$

One can see that the regulation profile is composed of three constants values for the acceleration. Moreover, this the target position is constant for $t > 12$s is constant. On the other hand, the tracking trajectory is $x_d(t) = 5\sin(\omega t)$ with $\omega = 0.2$ rad/s as the default value.

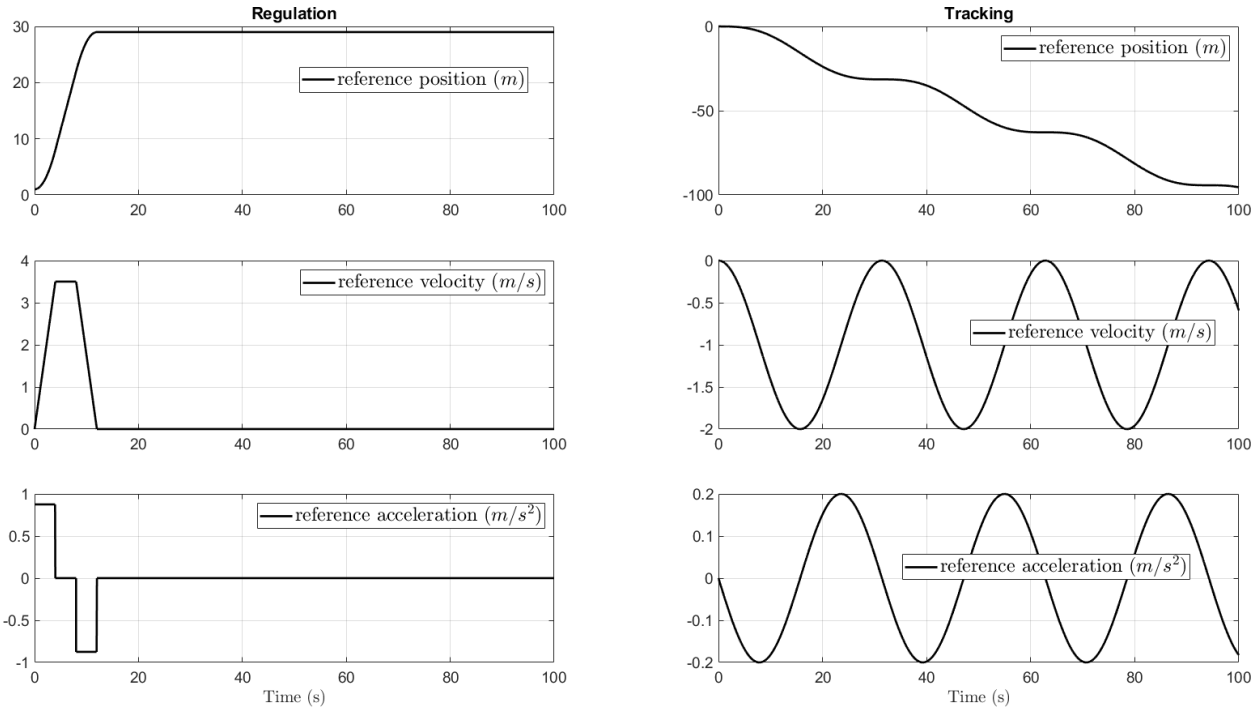

Figure 14: Trajectories used in the simulations

7.3 Optimization algorithms

As can be seen from Table 12, the closed-loop controllers have some parameters that have to be tuned. The formulation of the optimization problem and solving it using classical schemes is not straightforward due to the complexity of the problem. Hence, heuristic algorithms, *i.e.*, PARTICLE SWARM OPTIMIZATION, FMINUNC AND PATTERNSEARCH, exist in Matlab, are used to minimize (147). The diagrams corresponding to the optimizations are provided in Figs. 15 and 16.

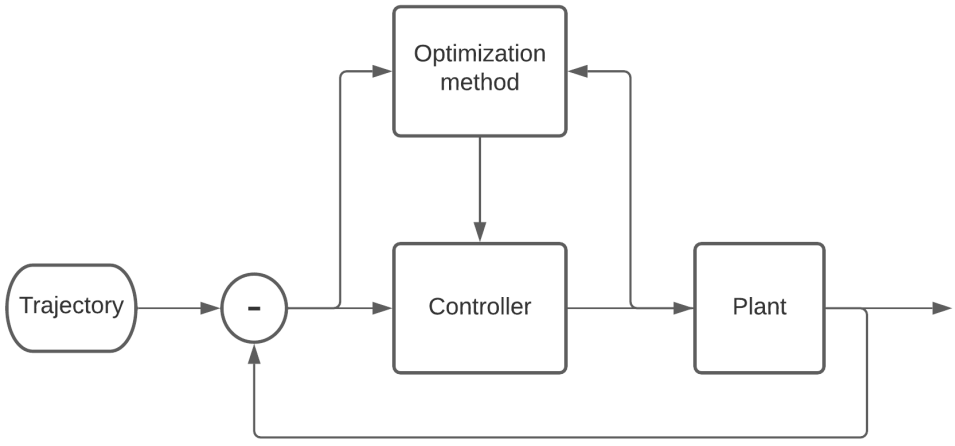

Figure 15: Optimization diagram in the control loop

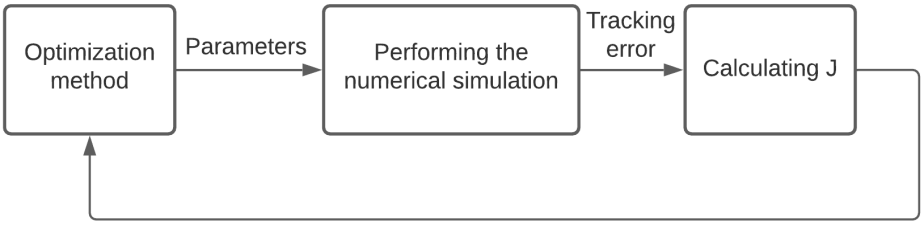

Figure 16: Optimization diagram (overview)

The parameters are optimized for a double-pendulum system in the worst case (SNR=20dB, initial zigzag sway with 15 degrees sway on all links, trolley damping=1000, and the piecewise trajectory explained before)

the objective function for the tuning is selected as follows:

$$\begin{aligned} J = &||e_p(t)||_{2,t\in[0,100]s} + 60||e_p(t)||_{2,t\in[16,100]s} + 300||e_p(t)||_{2,t\in[33,100]s} + \\ &600||e_p(t)||_{\infty} + 0.05\sum_{k=0}^{t_f/h}|u(kh) - u((k-1)h)| \end{aligned} \tag{147}$$

where e_p is the payload position error and $u(k)$ is the control signal at the step k, $t = kh$, and h is the sampling time.

7.3.1 Results of the optimization

Since the optimization algorithms used in this study work base on the initial random conditions, the results of the optimization may not be unique and may lead to different results for different executions. As it will be shown, these algorithms may not lead to globally optimal solutions. The controllers have been tuned for the worst case (see Table 16) and the obtained parameters corresponding to each controller are listed in a single table, as can be seen in Tables 17 to 32

Table 16: Conditions of the first optimization

Parameter	Value
Trajectory type	piecewise
Load type	heavy load
Initial sway type	15 degrees on all angles
Joints damping coefficient	1.6000 N*M/(deg/s)
Joints stiffness coefficient	0.8000 N*M/deg
Cart mass	10000.0000 kg
SNR value	90.0000 db
trolley damping	1000.0000 N*M/(m/s)
Disturbance condition	dis. on cart

Table 17: Collocated PD regulation control

Optimization method	Parameters	Cost	F-count
PSO	k_p=8e+02, k_d=3e+04	19161	2940
fmincon	k_p=1e+04, k_d=4e+04	26400	188
patternsearch	k_p=1e+04, k_d=4e+04	26400	241

Table 18: Quasi PID control

Optimization method	Parameters	Cost	F-count
PSO	k_p=1e+04, k_d=6e+04, k_i=1e+00, $k_{\phi 1}$=0e+00, $k_{\phi 2}$=4e-04, $\lambda = 5e+04$	18601	5400
fmincon	k_p=1e+03, k_d=3e+04, k_i=3e+03, $k_{\phi 1}$=1e+01, $k_{\phi 2}$=4e+02, $\lambda = 2e+01$	68434	2103
patternsearch	k_p=1e+04, k_d=6e+04, k_i=0e+00, $k_{\phi 1}$=0e+00, $k_{\phi 2}$=0e+00, $\lambda = 0e+00$	18602	1450

Table 19: noncollocated PD control (first angle)

Optimization method	Parameters	Cost	F-count
PSO	k_p=8e+02, k_d=3e+04, k_a=0e+00	19134	5850
fmincon	k_p=1e+04, k_d=4e+04, k_a=2e-11	26400	243
patternsearch	k_p=1e+04, k_d=4e+04, k_a=0e+00	26400	404

Table 20: noncollocated PD control (last angle)

Optimization method	Parameters	Cost	F-count
PSO	k_p=1e+04, k_d=4e+04, k_a=0e+00	26400	1410
fmincon	k_p=1e+04, k_d=4e+04, k_a=2e-09	26400	162
patternsearch	k_p=1e+04, k_d=4e+04, k_a=0e+00	26400	404

Table 21: Collocated PD tracking control

Optimization method	Parameters	Cost	F-count
PSO	k_p=2e+02, k_d=2e+04, L_0=3e+03, Z=3e+03, ϕ=0e+00	31548	2150
fmincon	k_p=2e+04, k_d=7e+03, L_0=3e+01, Z=1e+00, ϕ=2e+03	92737	147
patternsearch	k_p=6e+03, k_d=2e+04, L_0=0e+00, Z=0e+00, ϕ=0e+00	31548	446

Table 22: PD-PD

Optimization method	Parameters	Cost	F-count
PSO	α_1=1e+04, α_2=4e+04, α_3=3e+04, α_4=-9e-01	26022	1710
fmincon	α_1=1e+04, α_2=4e+04, α_3=3e+04, α_4=-8e-01	26024	357
patternsearch	α_1=1e+04, α_2=4e+04, α_3=3e+04, α_4=-8e-01	26023	855

Table 23: SMC Single-pendulum-first-angle (explicit)

Optimization method	Parameters	Cost	F-count
PSO	c_1=8e+03, c_2=2e+04, c_3 =1e+00 , c_4 =0e+00 , k=9e+00 , η =2e+02	49901	14880
fmincon	c_1=1e+00, c_2=1e+00, c_3 =1e+00 , c_4 =1e+00 , k=1e+00 , η =1e+00	2969696	122
patternsearch	c_1=4e-02, c_2=0e+00, c_3 =4e-02 , c_4 =0e+00 , k=3e-01 , η =2e-05	25723	1054

Table 24: SMC Single-pendulum-first-angle (implicit)

Optimization method	Parameters	Cost	F-count
PSO	c_1=3e+03, c_2=7e+03, c_3 =4e-02 , c_4 =2e-01 , k=1e+01 , η =1e+04	48033	6900
fmincon	c_1=1e+05, c_2=2e+04, c_3 =4e+04 , c_4 =2e-01 , k=9e-01 , η =2e-02	435338	522
patternsearch	c_1=4e-02, c_2=0e+00, c_3 =4e-02 , c_4 =0e+00 , k=3e-01 , η =2e-05	25720	940

Table 25: SMC Single-pendulum-last-angle (explicit)

Optimization method	Parameters	Cost	F-count
PSO	c_1=2e+04, c_2=2e+04, c_3 =1e-01 , c_4 =3e-03 , k=8e+00 , η =3e+02	157545	9780
fmincon	c_1=7e+02, c_2=8e+02, c_3 =1e-03 , c_4 =3e-03 , k=1e+01 , η =4e+00	162294	1918
patternsearch	c_1=4e-02, c_2=0e+00, c_3 =0e+00 , c_4 =0e+00 , k=3e-01 , η =1e-05	26382	786

Table 26: SMC Single-pendulum-last-angle (implicit)

Optimization method	Parameters	Cost	F-count
PSO	c_1=7e+03, c_2=1e+04, c_3 =5e+03 , c_4 =4e-03 , k=9e+00 , η =4e+04	150275	10260
fmincon	c_1=5e+02, c_2=8e+02, c_3 =4e+02 , c_4 =1e-03 , k=5e+01 , η =1e+00	176049	1114
patternsearch	c_1=4e-02, c_2=0e+00, c_3 =0e+00 , c_4 =0e+00 , k=3e-01 , η =2e-05	26384	576

Table 27: SMC Double-pendulum-first-angle (explicit)

Optimization method	Parameters	Cost	F-count
PSO	λ=2e+01, α=3e+00, β=1e+02 , K =6e+03 , c=9e+03	3072729	4650
fmincon	λ=1e+01, α=2e-08, β=6e+01 , K =4e-05 , c=2e+00	5780687	274
patternsearch	λ=4e+00, α=0e+00, β=2e+01 , K =9e+03 , c=0e+00	7565164	2639

Table 28: SMC Double-pendulum-last-angle (implicit)

Optimization method	Parameters	Cost	F-count
PSO	λ=1e+00, α=4e+00, β=0e+00 , K =3e-01 , c=0e+00	73481	2650
fmincon	λ=2e+00, α=4e+00, β=3e-08 , K =3e+00 , c=4e-01	46587	353
patternsearch	λ=1e+00, α=4e+00, β=0e+00 , K =0e+00 , c=0e+00	73481	1758

Table 29: PD energy - first

Optimization method	Parameters	Cost	F-count
PSO	k_p=4e+03, k_d=3e+04, k_q=0e+00 , λ =0e+00 , ζ=2e+04	19424	2050
fmincon	k_p=1e+03, k_d=3e+04, k_q=1e+05 , λ =1e+00 , ζ=4e+00	18806	1071
patternsearch	k_p=3e+03, k_d=3e+04, k_q=8e+04 , λ =1e+00 , ζ=2e+09	18884	1649

Table 30: PD energy - last

Optimization method	Parameters	Cost	F-count
PSO	k_p=4e+03, k_d=3e+04, k_q=1e+02 , λ =0e+00 , ζ=2e+04	19424	2100
fmincon	k_p=4e+03, k_d=3e+04, k_q=2e+03 , λ =1e-02 , ζ=3e+00	19423	482
patternsearch	k_p=4e+03, k_d=3e+04, k_q=3e+04 , λ =1e-02 , ζ=2e+07	19420	2111

Table 31: Coupling tracking - first

Optimization method	Parameters	Cost	F-count
PSO	k_p=6e+03, k_d=1e+04, λ=0e+00	123504	1350
fmincon	k_p=5e+03, k_d=7e+03, λ=6e-01	122748	464
patternsearch	k_p=5e+03, k_d=7e+03, λ=6e-01	122750	1053

Table 32: Coupling tracking - last

Optimization method	Parameters	Cost	F-count
PSO	k_p=6e+03, k_d=1e+04, λ=0e+00	123504	1140
fmincon	k_p=6e+03, k_d=1e+04, λ=4e-08	123504	146
patternsearch	k_p=6e+03, k_d=1e+04, λ=0e+00	123504	353

Table 33: Optimum parameters (reference trajectory: piecewise, heavy load, 15 degrees on all angles, damping coefficient=1.6 NM/(deg/s), joint stiffness=0.8 NM/deg, cart mass=1e+04, SNR=9e+01, cart damping=1e+03, , matched dis. on cart). First execution.

Method	Parameters	Cost	F-count
C PD reg.	k_p=8e+02, k_d=3e+04	19161	2940
Quasi-PID	k_p=1e+04, k_d=6e+04, k_i=1e+00, $k_{\phi 1}$=0e+00, $k_{\phi 2}$=4e-04, $\lambda = 5e+04$	18601	5400
Non.Col.PD.Reg first	k_p=1e+04, k_d=4e+04, k_a=0e+00	26400	1320
Non.Col.PD.Reg last	k_p=1e+03, k_d=3e+04, k_a=0e+00	20078	1500
Col.PD.Track	k_p=2e+02, k_d=2e+04, L_0=3e+03, Z=3e+03, ϕ=0e+00	31548	2150
PD-PD	α_1=1e+04, α_2=4e+04, α_3 =3e+04 , α_4 =-9e-01,	26022	1710
SMC-single-exp. (first)	c_1=4e-02, c_2=0e+00, c_3 =4e-02 , c_4 =0e+00 , k=3e-01 , η =2e-05	25723	1054
SMC-single-imp. (first)	c_1=4e-02, c_2=0e+00, c_3 =4e-02 , c_4 =0e+00 , k=3e-01 , η =2e-05	25720	940
SMC-single-exp. (last)	c_1=4e-02, c_2=0e+00, c_3 =0e+00 , c_4 =0e+00 , k=3e-01 , η =1e-05	26382	786
SMC-single-imp. (last)	c_1=4e-02, c_2=0e+00, c_3 =0e+00 , c_4 =0e+00 , k=3e-01 , η =2e-05	26384	576
SMC-double-exp.	λ=2e+01, α=3e+00, β=1e+02 , K =6e+03 , c=9e+03	3072729	4650
SMC-double-imp.	λ=2e+00, α=4e+00, β=3e-08 , K =3e+00 , c=4e-01	46587	353
PD energy (first)	k_p=1e+03, k_d=3e+04, k_q=1e+05 , λ =1e+00 , ζ=4e+00	18806	1071
PD energy (last)	k_p=4e+03, k_d=3e+04, k_q=3e+04 , λ =1e-02 , ζ=2e+07	19420	2111
Coupling tracking (first)	k_p=5e+03, k_d=7e+03, λ=6e-01	122748	464
Coupling tracking (last)	k_p=6e+03, k_d=1e+04, λ=0e+00	123504	353

The optimal parameters of all controllers and the corresponding cost value are listed in Table 33. From this table, one may see that the optimization algorithms do not necessarily lead to the optimal solutions, For instance, one may see that Non.Col.PD.Reg for the first and the last angle always lead to a larger cost compared to the Col. PD reg. However, all these three controllers lead to exactly the same structure since k_a is always zero. Therefore, k_p and k_d corresponding to the Col. PD reg. should also be selected for the other two controllers which is not the case here. As the result, a larger cost has been obtained for these two noncollocated controllers. It indicates that these optimization algorithms do not necessarily lead to optimal solutions.

To study the effect of the conditions on the gain tuning, the gains have been tuned for the unperturbed case, *i.e.*, condition without any noise, disturbance, and initial sway. The results are provided in Table 34.

Comparing the new results with Table 33, one can see that the parameters has not been changed significantly. It indicates the parameter tuning scheme can be considered reliable and robust to the condition. The parameters in Table 33 have been used for the numerical simulations in the next sections.

Table 34: Optimum parameters (reference trajectory: piecewise, heavy load, no initial sway, damping coefficient=1.6 NM/(deg/s), joint stiffness=0.8 NM/deg, cart mass=1e+04, SNR=Inf, cart damping=0e+00, no dis.).

Method	Parameters	Cost	F-count
Col. PD reg.	k_p=9e+02, k_d=4e+04	17251	1220
Quasi-PID	k_p=2e+03, k_d=5e+04, k_i=5e+01, $k_{\phi 1}$=1e+00, $k_{\phi 2}$=2e+06, $\lambda = 2e+05$	12273	12540
Non.Col.PD.Reg first	k_p=4e+02, k_d=3e+04, k_a=0e+00	16241	6990
Non.Col.PD.Reg last	k_p=4e+02, k_d=3e+04, k_a=0e+00	16243	2070
Col.PD.Track	k_p=0e+00, k_d=3e+04, L_0=2e+03, Z=3e+03, ϕ=0e+00	25806	1700
PD-PD	α_1=4e+02, α_2=3e+04, α_3 =5e-01 , α_4 =-2e-05,	16246	4140
SMC-single-exp. (first)	c_1=5e-02, c_2=0e+00, c_3 =0e+00 , c_4 =0e+00 , k=3e-01 , η =2e-05	20980	515
SMC-single-imp. (first)	c_1=5e-02, c_2=0e+00, c_3 =0e+00 , c_4 =0e+00 , k=3e-01 , η =2e-05	20980	509
SMC-single-exp. (last)	c_1=5e-02, c_2=0e+00, c_3 =0e+00 , c_4 =0e+00 , k=3e-01 , η =2e-05	20980	515
SMC-single-imp. (last)	c_1=5e-02, c_2=0e+00, c_3 =0e+00 , c_4 =0e+00 , k=3e-01 , η =2e-05	20980	509
SMC-double-exp.	λ=0e+00, α=9e+02, β=2e+03 , K =0e+00 , c=0e+00	2774879	1100
SMC-double-imp.	λ=4e-01, α=5e-01, β=2e-01 , K =1e+02 , c=8e-02	110379	1105
PD energy (first)	k_p=2e+03, k_d=3e+04, k_q=8e+03 , λ =0e+00 , ζ=5e+03	16225	2750
PD energy (last)	k_p=2e+03, k_d=3e+04, k_q=2e+04 , λ =0e+00 , ζ=4e+03	16225	2500
Coupling tracking (first)	k_p=4e+03, k_d=7e+03, λ=8e-01	117197	618
Coupling tracking (last)	k_p=5e+02, k_d=1e+02, λ=3e+00	53599	447

7.4 Regulation in nominal condition

The conditions of this simulation are shown in Table 35. As can be seen from this table, the aim of this simulation is to investigate the behavior of the controllers for the regulation and under nominal condition without any noise, disturbance and uncertainty.

Table 35: Conditions of the simulations

Parameter	Value
Trajectory type	piecewise
Load type	heavy load
Initial sway type	no initial sway
Damping coefficient	1.6000 N*M/(deg/s)
Joint stiffness	0.8000 N*M/deg
Cart mass	10000.0000 kg
SNR value	Inf db
trolley damping	0.0000 N*M/(m/s)
Disturbance condition	no dis.

The performances of all controllers under the specified conditions are summarized in Table 36. Since the system is not disturbed, even the performances of the open-loop methods are comparable with the closed-loop ones. Considering Table 36, one can see that the unshaped control shows the smallest amount of $\tilde{L}_2(e_p)$ after the collocated PD tracking controller. However, this method is not successful in minimizing the total sway $\bar{L}_2(e_a)$. According to this simulation, the collocated PD tracking controller looks to be the best in minimizing the payload position error under this unperturbed condition. Another observation is that the SMC designed for the double-pendulum system shows the worst responses. Another observation from Table 36 is that the open-loop control methods use the smallest amount of control energy since they do not inject virtual damping to the system.

Table 36: Comparing the methods (reference trajectory: piecewise, heavy load, no initial sway, damping coefficient=1.6 NM/(deg/s), joint stiffness=0.8 NM/deg, cart mass=10000, SNR=Inf, cart damping=0, no dis.).

Method	$\tilde{L}_2(e_p)$	$\tilde{L}_2(e_c)$	$\bar{L}_2(e_a)$	$\tilde{L}_2(F)$	t_s	t_{cs}
Unshaped input	1.08	1.20	7.08	15795	100.00	100.00
ZV	2.14	2.18	5.59	12611	100.00	100.00
ZVD	3.13	3.12	4.71	11020	100.00	100.00
Collocated PD	2.12	2.07	2.22	12924	21.04	97.98
quasi-PID	1.38	1.27	2.84	15360	31.90	41.28
Non.CO.PD.Reg. (first)	2.14	2.09	2.21	12857	21.06	98.78
Non.CO.PD.Reg. (last)	1.37	1.09	3.77	20516	87.41	95.53
Col.PD.Track	0.55	0.35	4.28	18035	100.00	100.00
PD-PD	1.40	1.11	3.74	20745	76.43	84.58
SMC-single-first (explicit)	1.39	1.10	3.77	20787	100.00	100.00
SMC-single-first (implicit)	1.39	1.10	3.77	20787	99.99	100.00
SMC-single-last (explicit)	1.37	1.09	3.78	20499	99.97	100.00
SMC-single-last (implicit)	1.37	1.09	3.79	20523	99.98	100.00
SMC-double (explicit)	21.65	21.64	15.25	99533	100.00	100.00
SMC-double (implicit)	1.86	1.84	14.10	94108	100.00	100.00
PD energy (first)	2.00	1.96	2.23	12398	98.19	100.00
PD energy (last)	2.14	2.10	2.14	12303	36.97	45.08
Coupling tracking (first)	1.17	1.14	3.96	16161	100.00	100.00
Coupling tracking (last)	1.11	1.07	4.04	16755	100.00	100.00

7.5 Tracking under nominal condition

The condition of this simulation is shown in Table 37. It can be seen that a sinusoidal trajectory has been considered in this case to evaluate the trajectory tracking performances under noise-free condition.

Table 37: Conditions of the simulations

Parameter	Value
Trajectory type	sinusoidal with initial error
Load type	heavy load
Initial sway type	no initial sway
Damping coefficient	1.6000 N*M/(deg/s)
Joint stiffness	0.8000 N*M/deg
Cart mass	10000.0000 kg
SNR value	Inf db
trolley damping	0.0000 N*M/(m/s)
Disturbance condition	no dis.

The summarized results for the tracking problem are shown in Table 38. The first observation is that the tracking controllers, *i.e.*, collocated PD tracking and the coupling tracking achieve the best results. It is also can be seen that for the noncollocated tracking one, *i.e.*, coupling tracking it is better to sense the last sway angle rather than the first one. However, comparing, for example, the feedback sensing from the first and the last angles, one can see that the first feedback sway sensing leads to a smaller total sway $\bar{L}_2$ as well as control energy $\tilde{F}$. Moreover, non-collocation feedback may not provide any advantages for this scenario since the best results have been achieved for the collocated PD tracking controller.

According to Table 38 it can be seen that the open-loop methods are the worst in case of tracking for both trolley and the payload. On the other hand, it can be seen again that the open-loop methods are the best in case of the control energy and the sway reduction. The reason is that the open-loop methods do not inject any virtual damping to the system. Similar to the previous case, the SMC designed for the double-pendulum as well as the PD energy with the first angle sensing have achieved the worst results in terms of tracking for both trolley and the payload as well as the control energy and the sway angles. However, as can be seen, the PD energy can achieve better responses with a sway sensor on the last angle.

Table 38: Comparing the methods (reference trajectory: sinusoidal with initial error, heavy load, no initial sway, damping coefficient=1.6 NM/(deg/s), joint stiffness=0.8 NM/deg, cart mass=10000, SNR=Inf, cart damping=0, no dis.). $\omega = 0.2$ rad/s

Method	$\tilde{L}_2(e_p)$	$\tilde{L}_2(e_c)$	$\bar{L}_2(e_a)$	$\tilde{L}_2(F)$	t_s	t_{cs}
Unshaped input	57.51	57.51	1.46	8932	100.00	100.00
ZV	56.48	56.47	1.39	8495	100.00	100.00
ZVD	55.35	55.34	1.33	8106	100.00	100.00
Collocated PD	1.64	1.60	1.98	9418	100.00	100.00
quasi-PID	0.84	0.71	2.54	11523	100.00	100.00
Non.CO.PD.Reg. (first)	1.66	1.61	1.97	9392	100.00	100.00
Non.CO.PD.Reg. (last)	0.91	0.73	2.71	12063	100.00	100.00
Col.PD.Track	0.49	0.42	2.00	10024	100.00	100.00
PD-PD	0.92	0.74	2.59	12064	100.00	100.00
SMC-single-first (explicit)	0.91	0.73	2.61	12053	100.00	100.00
SMC-single-first (implicit)	0.91	0.73	2.61	12053	100.00	100.00
SMC-single-last (explicit)	0.91	0.73	2.72	12062	100.00	100.00
SMC-single-last (implicit)	0.91	0.73	2.72	12063	100.00	100.00
SMC-double (explicit)	3.34	3.35	14.05	99541	100.00	100.00
SMC-double (implicit)	2.62	2.60	21.65	92152	100.00	100.00
PD energy (first)	2.70	2.48	6.12	24375	100.00	100.00
PD energy (last)	1.81	1.74	2.07	10165	100.00	100.00
Coupling tracking (first)	0.96	0.86	1.81	10612	100.00	100.00
Coupling tracking (last)	0.67	0.59	1.84	10197	100.00	100.00

The tracking performances of the controllers for the position trajectory $x_d = \sin(\omega t)$ and different ω are illustrated in Fig. 17. From this figure, one can see that the open-loop methods are too sensitive to the frequency of the trajectory. Moreover, the tracking controllers show the smallest position tracking errors.

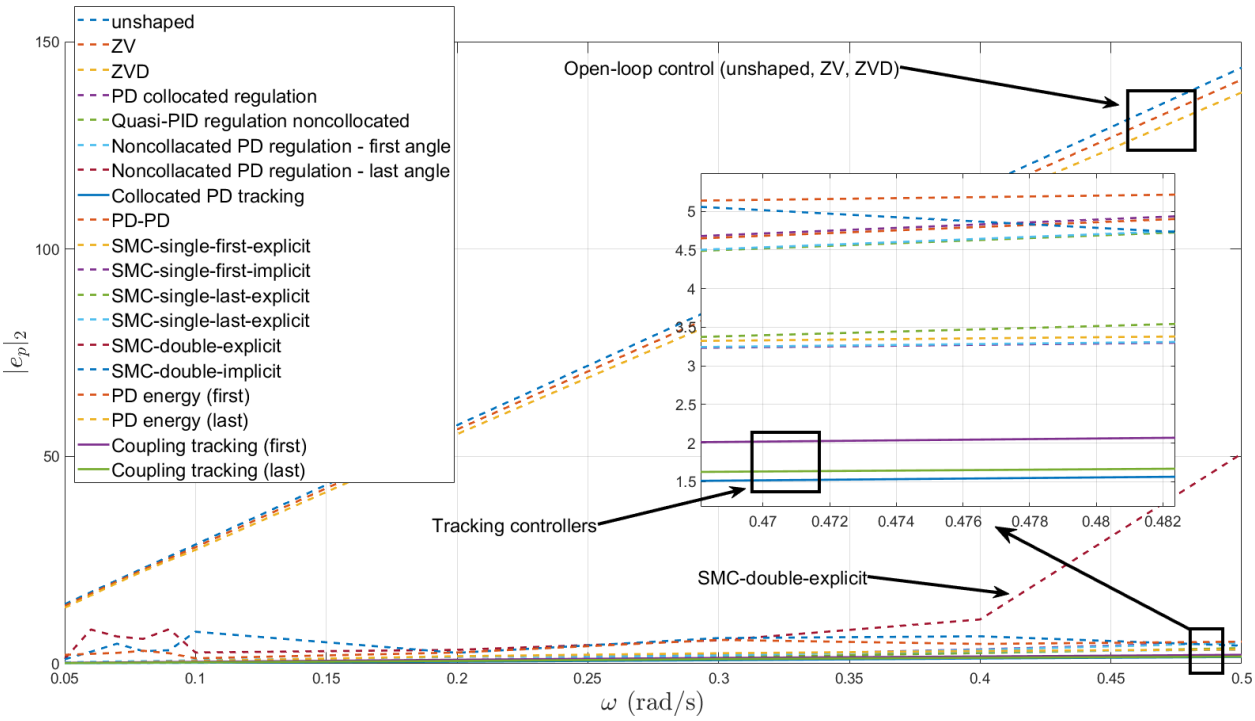

Figure 17: L_2 norms of the payload position tracking error for the trajectory $x_d(t) = 5\sin(\omega t)$ under parameters listed in Table 37

7.6 Initial sway control

Two sets of simulations have been conducted to study the controllers in the presence of initial sway with the conditions shown in Tables 39 and 41, respectively, and the results corresponding to these cases are listed in Tables 40 and 42, respectively. As before, the open-loop methods show the largest total sway $\bar{L}_2(e_a)$ withe the smallest control energy. Double-pendulum SMC is also one of the worst as before. On the other hand, collocated PD tracking shows one of the best tracking performances. Moreover, the Quasi-PID has the smallest t_s and t_{cs} among the methods.

Table 39: Conditions of the simulations

Parameter	Value
Trajectory type	piecewise
Load type	heavy load
Initial sway type	15 degrees on all angles
Damping coefficient	1.6000 N*M/(deg/s)
Joint stiffness	0.8000 N*M/deg
Cart mass	10000.0000 kg
SNR value	Inf db
Trolley damping	0.0000 N*M/(m/s)
Disturbance condition	no dis.

Table 40: Comparing the methods (reference trajectory: piecewise, heavy load, 30 degrees on the first angle, damping coefficient=1.6 NM/(deg/s), joint stiffness=0.8 NM/deg, cart mass=10000, SNR=Inf, cart damping=0, no dis.).

Method	$\tilde{L}_2(e_p)$	$\tilde{L}_2(e_c)$	$\bar{L}_2(e_a)$	$\tilde{L}_2(F)$	t_s	t_{cs}
Unshaped input	3.55	4.84	47.37	15795	100.00	100.00
ZV	5.23	5.99	44.22	12611	100.00	100.00
ZVD	5.32	5.93	40.19	11020	100.00	100.00
Collocated PD	2.03	1.96	7.32	19825	100.00	100.00
quasi-PID	2.81	2.77	8.61	19244	45.04	53.18
Non.CO.PD.Reg. (first)	2.04	1.98	7.31	19741	100.00	100.00
Non.CO.PD.Reg. (last)	1.68	1.35	8.59	28315	100.00	100.00
Col.PD.Track	0.90	0.90	9.70	21457	100.00	100.00
PD-PD	1.71	1.36	8.53	28566	99.95	100.00
SMC-single-first (explicit)	1.70	1.35	8.74	28535	100.00	100.00
SMC-single-first (implicit)	1.70	1.35	8.73	28538	100.00	100.00
SMC-single-last (explicit)	1.68	1.35	8.60	28293	100.00	100.00
SMC-single-last (implicit)	1.68	1.35	8.60	28331	100.00	100.00
SMC-double (explicit)	35.33	35.33	18.00	99712	100.00	100.00
SMC-double (implicit)	17.18	17.17	19.52	97983	100.00	100.00
PD energy (first)	4.44	4.41	10.04	22239	100.00	100.00
PD energy (last)	2.04	1.99	7.25	19307	100.00	100.00
Coupling tracking (first)	1.74	1.81	10.64	17070	100.00	100.00
Coupling tracking (last)	1.44	1.52	10.52	18250	100.00	100.00

Table 41: Conditions of the simulations

Parameter	Value
Trajectory type	piecewise
Load type	heavy load
Initial sway type	15 degrees on all angles
Damping coefficient	1.6000 N*M/(deg/s)
Joint stiffness	0.8000 N*M/deg
Cart mass	10000.0000 kg
SNR value	Inf db
Trolley damping	0.0000 N*M/(m/s)
Disturbance condition	no dis.

Table 42: Comparing the methods (reference trajectory: piecewise, heavy load, 15 degrees on all angles, damping coefficient=1.6 NM/(deg/s), joint stiffness=0.8 NM/deg, cart mass=10000, SNR=Inf, cart damping=0, no dis.).

Method	$\tilde{L}_2(e_p)$	$\tilde{L}_2(e_c)$	$\bar{L}_2(e_a)$	$\tilde{L}_2(F)$	t_s	t_{cs}
Unshaped input	0.53	1.85	54.07	15797	100.00	100.00
ZV	2.53	3.07	52.27	12612	100.00	100.00
ZVD	3.23	3.51	48.14	11020	100.00	100.00
Collocated PD	2.11	2.05	35.26	14537	100.00	100.00
quasi-PID	1.50	1.40	32.95	17825	66.19	73.83
Non.CO.PD.Reg. (first)	2.13	2.07	35.22	14446	100.00	100.00
Non.CO.PD.Reg. (last)	1.43	1.13	34.98	23327	100.00	100.00
Col.PD.Track	0.50	0.37	37.78	18703	100.00	100.00
PD-PD	1.43	1.13	34.18	23071	100.00	100.00
SMC-single-first (explicit)	1.50	1.19	32.98	24853	100.00	100.00
SMC-single-first (implicit)	1.50	1.19	32.97	24858	100.00	100.00
SMC-single-last (explicit)	1.42	1.13	34.98	23316	100.00	100.00
SMC-single-last (implicit)	1.42	1.12	34.91	23284	100.00	100.00
SMC-double (explicit)	6.46	6.47	32.75	99781	100.00	100.00
SMC-double (implicit)	3.23	3.22	35.13	93795	100.00	100.00
PD energy (first)	2.07	2.02	34.26	24120	100.00	100.00
PD energy (last)	2.14	2.09	35.12	13944	100.00	100.00
Coupling tracking (first)	1.55	1.52	64.87	52279	100.00	100.00
Coupling tracking (last)	1.05	1.05	38.12	16492	100.00	100.00

7.7 Robustness to matched uncertainties

A pulse forces with period 20s and amplitude ±19600N is applied directly to the cart toward the x-axis to investigate the robustness against the matched disturbance, and the results are summarized in Table 44.

Table 43: Conditions of the simulations

Parameter	Value
Trajectory type	piecewise
Load type	heavy load
Initial sway type	no initial sway
Damping coefficient	1.6000 N*M/(deg/s)
Joint stiffness	0.8000 N*M/deg
Cart mass	10000.0000 kg
SNR value	Inf db
trolley damping	0.0000 N*M/(m/s)
Disturbance condition	dis. on cart

Table 44: Comparing the methods (reference trajectory: piecewise, heavy load, no initial sway, damping coefficient=1.6 NM/(deg/s), joint stiffness=0.8 NM/deg, cart mass=10000, SNR=Inf, cart damping=0, dis. on cart).

Method	$\tilde{L}_2(e_p)$	$\tilde{L}_2(e_c)$	$\bar{L}_2(e_a)$	$\tilde{L}_2(F)$	t_s	t_{cs}
Unshaped input	88.00	87.97	27.98	15795	100.00	100.00
ZV	89.99	89.96	27.90	12611	100.00	100.00
ZVD	89.91	89.88	27.70	11020	100.00	100.00
Collocated PD	2.56	2.33	4.92	18876	100.00	100.00
quasi-PID	1.65	1.41	6.54	24742	100.00	100.00
Non.CO.PD.Reg. (first)	2.58	2.35	4.91	18775	100.00	100.00
Non.CO.PD.Reg. (last)	1.86	1.51	6.30	29910	100.00	100.00
Col.PD.Track	2.94	2.55	6.81	30727	100.00	100.00
PD-PD	1.96	1.59	6.08	30499	99.99	100.00
SMC-single-first (explicit)	1.97	1.60	5.88	30622	100.00	100.00
SMC-single-first (implicit)	1.97	1.60	5.88	30619	100.00	100.00
SMC-single-last (explicit)	1.86	1.51	6.30	29889	100.00	100.00
SMC-single-last (implicit)	1.86	1.50	6.31	29915	100.00	100.00
SMC-double (explicit)	13.08	13.00	17.13	99500	100.00	100.00
SMC-double (implicit)	9.62	9.50	15.91	96038	100.00	100.00
PD energy (first)	2.51	2.23	5.88	23549	100.00	100.00
PD energy (last)	2.59	2.33	4.93	19054	100.00	100.00
Coupling tracking (first)	7.53	6.72	10.14	43638	100.00	100.00
Coupling tracking (last)	5.03	4.47	8.07	36782	100.00	100.00

7.8 Robustness to mismatched uncertainties

The aim of this simulation is to study the performances under a mismatched disturbance. To this end a pulse forces with period 20s and amplitude ±19600N is applied directly to the payload toward the x-axis, and the results are shown in Table 46.

Table 45: Conditions of the simulations

Parameter	Value
Trajectory type	piecewise
Load type	heavy load
Initial sway type	no initial sway
Damping coefficient	1.6000 N*M/(deg/s)
Joint stiffness	0.8000 N*M/deg
Cart mass	10000.0000 kg
SNR value	Inf db
trolley damping	0.0000 N*M/(m/s)
Disturbance condition	dis. on load

According to Table 46, the open-loop methods show the worst responses with the smallest amount of control energy which is not surprising. In general, the best responses belong to the quasi-PID, non collocated PD regulation, collocated PD tracking, PD-PD and the single-pendulum SMCs.

Table 46: Comparing the methods (reference trajectory: piecewise, heavy load, no initial sway, damping coefficient=1.6 NM/(deg/s), joint stiffness=0.8 NM/deg, cart mass=10000, SNR=Inf, cart damping=0, dis. on load).

Method	$\tilde{L}_2(e_p)$	$\tilde{L}_2(e_c)$	$\bar{L}_2(e_a)$	$\tilde{L}_2(F)$	t_s	t_{cs}
Unshaped input	34.69	34.68	6.97	15795	100.00	100.00
ZV	36.70	36.70	5.58	12611	100.00	100.00
ZVD	36.66	36.66	4.82	11020	100.00	100.00
Collocated PD	1.95	1.90	3.10	13542	100.00	100.00
quasi-PID	1.29	1.16	3.72	17213	100.00	100.00
Non.CO.PD.Reg. (first)	1.97	1.92	3.08	13467	100.00	100.00
Non.CO.PD.Reg. (last)	1.44	1.14	4.62	22094	100.00	100.00
Col.PD.Track	1.42	1.19	5.31	21454	100.00	100.00
PD-PD	1.47	1.16	4.61	22343	100.00	100.00
SMC-single-first (explicit)	1.47	1.15	4.57	22395	100.00	100.00
SMC-single-first (implicit)	1.47	1.15	4.57	22395	100.00	100.00
SMC-single-last (explicit)	1.44	1.14	4.62	22076	100.00	100.00
SMC-single-last (implicit)	1.44	1.14	4.63	22101	100.00	100.00
SMC-double (explicit)	18.32	18.30	14.18	99361	100.00	100.00
SMC-double (implicit)	2.04	2.02	18.87	89766	100.00	100.00
PD energy (first)	1.79	1.74	2.99	13350	100.00	100.00
PD energy (last)	1.91	1.85	3.09	13535	100.00	100.00
Coupling tracking (first)	3.43	3.13	5.72	24782	100.00	100.00
Coupling tracking (last)	2.44	2.20	5.41	22690	100.00	100.00

7.9 Robustness to measurement noise

This simulation mainly evaluate the controllers in the presence of measurement noise. The results in this case are not unexpected since the noise affected more the feedback-based methods. Moreover, the tracking controllers are less affected by noise since they are are also dependent to the feedforward terms rather than the feedback ones.

Table 47: Conditions of the simulations

Parameter	Value
Trajectory type	piecewise
Load type	heavy load
Initial sway type	no initial sway
Damping coefficient	1.6000 N*M/(deg/s)
Joint stiffness	0.8000 N*M/deg
Cart mass	10000.0000 kg
SNR value	90.0000 db
Trolley damping	0.0000 N*M/(m/s)
Disturbance condition	no dis.

Table 48: Comparing the methods (reference trajectory: piecewise, heavy load, no initial sway, damping coefficient=1.6 NM/(deg/s), joint stiffness=0.8 NM/deg, cart mass=10000, SNR=90, cart damping=0, no dis.).

Method	$\tilde{L}_2(e_p)$	$\tilde{L}_2(e_c)$	$\bar{L}_2(e_a)$	$\tilde{L}_2(F)$	t_s	t_{cs}
Unshaped input	1.08	1.20	7.08	15795	100.00	100.00
ZV	2.14	2.18	5.59	12611	100.00	100.00
ZVD	3.13	3.12	4.71	11020	100.00	100.00
Collocated PD	2.12	2.07	2.22	12924	21.04	97.98
quasi-PID	1.38	1.27	2.84	15360	31.90	41.28
Non.CO.PD.Reg. (first)	2.14	2.09	2.21	12857	21.06	98.78
Non.CO.PD.Reg. (last)	1.37	1.09	3.77	20516	87.41	95.53
Col.PD.Track	0.55	0.35	4.28	18035	100.00	100.00
PD-PD	1.40	1.11	3.74	20745	76.44	84.58
SMC-single-first (explicit)	1.39	1.10	3.77	20787	100.00	100.00
SMC-single-first (implicit)	1.39	1.10	3.77	20787	99.99	100.00
SMC-single-last (explicit)	1.37	1.09	3.78	20499	99.97	100.00
SMC-single-last (implicit)	1.37	1.09	3.79	20523	99.98	100.00
SMC-double (explicit)	13.08	13.06	14.01	99417	100.00	100.00
SMC-double (implicit)	3.81	3.80	14.53	94259	100.00	100.00
PD energy (first)	2.00	1.96	2.23	12398	98.19	100.00
PD energy (last)	2.14	2.10	2.14	12303	36.97	45.08
Coupling tracking (first)	1.17	1.14	3.96	16161	100.00	100.00
Coupling tracking (last)	1.11	1.07	4.04	16755	100.00	100.00

7.10 Operation under no load condition

The aim of this simulation is to study the performances under an unperturbed no load condition as indicated in Table 49. In this case, the masses of the hook and the payload are equal to 20 kg.

Table 49: Conditions of the simulations

Parameter	Value
Trajectory type	piecewise
Load type	light load
Initial sway type	no initial sway
Damping coefficient	1.6000 N*M/(deg/s)
Joint stiffness	0.8000 N*M/deg
Cart mass	10000.0000 kg
SNR value	Inf db
trolley damping	0.0000 N*M/(m/s)
Disturbance condition	no dis.

The summarized results for the regulation profile and no payload are provided in Table 50. Double-pendulum SMC has achieved the worst results again. Moreover, it is surprising that the PD-PD method does not achieve good results for this case. In fact, PD-PD is designed based on the PDE of the system and it is expected that it provide some advantages for the string-like systems. In this condition the best results correspond to the collocated PD tracking controller. It seems that this controller is always one of the best for unperturbed systems. The single-pendulum SMC is also one of the best when sensing the last angle.

Table 50: Comparing the methods (reference trajectory: piecewise, light load, no initial sway, damping coefficient=1.6 NM/(deg/s), joint stiffness=0.8 NM/deg, cart mass=10000, SNR=Inf, cart damping=0, no dis.).

Method	$\tilde{L}_2(e_p)$	$\tilde{L}_2(e_c)$	$\bar{L}_2(e_a)$	$\tilde{L}_2(F)$	t_s	t_{cs}
Unshaped input	2.24	1.04	27.39	2553	100.00	100.00
ZV	2.17	2.15	6.50	2038	100.00	100.00
ZVD	3.16	3.12	5.38	1781	97.60	100.00
Collocated PD	1.82	0.60	23.47	2591	100.00	100.00
quasi-PID	1.94	0.29	26.44	2844	100.00	100.00
Non.CO.PD.Reg. (first)	1.81	0.60	23.40	2589	100.00	100.00
Non.CO.PD.Reg. (last)	1.86	0.22	25.74	2848	100.00	100.00
Col.PD.Track	1.78	0.16	26.04	2856	100.00	100.00
PD-PD	6.86	0.51	194.94	7725	100.00	100.00
SMC-single-first (explicit)	6.34	0.55	231.75	11744	100.00	100.00
SMC-single-first (implicit)	6.32	0.55	234.39	11284	100.00	100.00
SMC-single-last (explicit)	1.86	0.23	25.76	2848	100.00	100.00
SMC-single-last (implicit)	1.86	0.22	25.77	2850	100.00	100.00
SMC-double (explicit)	123.33	123.00	3161.24	98813	100.00	100.00
SMC-double (implicit)	4.52	1.60	672.99	26961	100.00	100.00
PD energy (first)	3.78	0.48	138.15	7772	100.00	100.00
PD energy (last)	1.81	0.46	23.63	2640	100.00	100.00
Coupling tracking (first)	1.36	1.02	13.79	2666	100.00	100.00
Coupling tracking (last)	1.94	1.00	23.73	2734	100.00	100.00

7.11 Summarized results under different conditions

The results obtained from the numerical simulations under different conditions are summarized in Table 51. In this table, e_p, e_c, e_a, and F are the contracted forms of $\tilde{L}_2(e_p)$, $\tilde{L}_2(e_c)$, $\bar{L}_2(e_a)$, and $\tilde{L}_2(F)$, respectively, and the colors and show the best and the worst results, respectively. The following general conclusions are achieved according to the according to Table 51:

- The open-loop methods, *i.e.*, unshaped input, ZV and ZVD, always consume the smallest amount of control energy, and their performances are acceptable under unperturbed case and regulation trajectory. However, in the presence of perturbations or for the tracking case, they show the worst results and should be avoided.

- The tracking controllers, *i.e.*, collocated PD tracking and the coupling tracking, show the best responses

for all cases except for the conditions when the system is affected by external disturbances and initial sway. The reason is that, according to Table 15, the tracking controllers contain feedforward terms which decreases their dependency to the feedback. As a result, the tracking controller still show the best responses in the presence of the measurement noise on the feedback path.

- The discretization does not affect the single-pendulum SMC since, according to Table 33, the coefficients corresponding to the discontinuous (set-valued) terms are almost zero.
- Noncollocated feedback does not necessarily provide more advantages over the collocated counterparts.
- The SMCs designed for the double pendulum system show the worst results for almost all conditions, specially under explicit discretization.

Table 51: Summarized results obtained from the numerical simulations (2D case)

Method	Regulation	Track.	Init. sway	Matched	Mismatched	Noise	load-free
Unshaped input	e_p, e_c, e_a	e_p,e_c, e_a,F	e_a, F	e_p, e_c, e_a, F	e_p, e_c, F		F
ZV	F	e_p,e_c, e_a,F	e_a, F	e_p, e_c, e_a, F	e_p, e_c, F		e_a,F
ZVD	F	e_p,e_c, e_a,F	e_a, F	e_p, e_c, e_a, F	e_p, e_c, F		e_a,F
Collocated PD	e_c,e_a,F				e_a		e_p, e_c
quasi-PID	e_p,e_c,e_a			e_p, e_c	e_p, e_c		e_p, e_c
Non.CO.PD.Reg. (first)	e_a,F				e_a		e_p, e_c
Non.CO.PD.Reg. (last)	e_p, e_c			e_c	e_p, e_c		e_p, e_c
Col.PD.Track	e_p, e_c	e_p,e_c	e_p, e_c		e_p,e_c	e_p, e_c	e_p, e_c
PD-PD	e_p, e_c			e_c	e_p, e_c		e_c
SMC-single-first (explicit)	e_p, e_c			e_c	e_p, e_c		e_c
SMC-single-first (implicit)	e_p, e_c			e_c	e_p, e_c		e_c
SMC-single-last (explicit)	e_p, e_c			e_c	e_p, e_c		e_p, e_c
SMC-single-last (implicit)	e_p, e_c			e_c	e_p, e_c		e_p, e_c
SMC-double (explicit)	e_p,e_c,e_a,F	e_p,e_c, e_a,F	e_p, e_c		e_p,e_c,e_a,F	e_p,e_c,e_a,F	e_p,e_c,e_a,F
SMC-double (implicit)	e_p,e_a,F	e_p,e_c, e_a,F	e_p, e_c		e_a,F	e_a,F	F
PD energy (first)	e_a,F	e_p,e_c, e_a,F			e_a		e_c
PD energy (last)	e_a,F				e_a		e_p,e_c
Coupling tracking (first)	e_p,e_c		e_a				e_p
Coupling tracking (last)	e_p,e_c	e_p,e_c					e_p

8 Comparisons of the controllers implemented for 3D space (trolley moves on a plane)

As it was mentioned in Section 3.4.4, Some controllers have also been developed for the 3D space to handle the coupling between the x and y axes [Wu and He, 2017, Tuan et al., 2012, 2014, Lee et al., 2013, Sun et al., 2013, Chwa, 2009, Wu and He, 2016, Tuan et al., 2012, 2014, Lee et al., 2013, Chwa, 2017, Knierim et al., 2010]. Note that [Tuan et al., 2012, 2014, Lee et al., 2013] has been designed when the cable length is variable, and therefore the cable's length is a control output. Hence, implementation of this method on the 20-link fixed length model developed in this study may not be straightforward and is ignored (finite element modeling of variable cables addressed in [Quan and Chang, 2020] may be used for this purpose). These controllers are briefly introduced below:

different control methods developed for cranes in 3D space are reviewed in Section 3.4.4, and it was mentioned that a portion of these methods are to handle the coupling effect in 3D space. In summary, the control methods developed for cranes with lumped masses in 3D space to handle the coupling are as follows:

- Methods developed by defining a Lyapunov function containing the error variables corresponding to two axes.
- Methods designed based on the partial feedback linearization.
- Methods developed based on the flatness theory.
- Methods derived by adding some extra terms to the previous methods developed for 2D space.
- Methods developed based on the SMC to reject the coupling as a disturbance.

8.1 Parameter tuning in 3D space

The controllers' parameters in 3D space are just tuned based on the single-pendulum model because of the complexity of the problem. The equations of the single-pendulum system where the masses are lumped in the trolley and the payload are as follows [Sun et al., 2013, Lee, 1998, Wu et al., 2014]:

$$\begin{cases} (m+m_x)\ddot{x} + mlC_xC_y\ddot{\theta}_x - mlS_xS_y\ddot{\theta}_y - mlS_xC_y\dot{\theta}_x^2 - 2mlC_xS_y\dot{\theta}_x\dot{\theta}_y - mlS_xC_y\dot{\theta}_y^2 = F_x \\ (m+m_y)\ddot{y} + mlC_y\ddot{\theta}_y - mlS_y\dot{\theta}_y^2 = F_y \\ mlC_xC_y\ddot{x} + ml^2C_y^2\ddot{\theta}_x - 2ml^2S_yC_y\dot{\theta}_x\dot{\theta}_y + mglS_xC_y = 0 \\ mlS_xS_y\ddot{x} - mlC_y\ddot{y} - ml\ddot{\theta}_y - ml^2S_yC_y\dot{\theta}_x^2 - mglC_xS_y = 0 \end{cases} \tag{148}$$

where m is the payload mass, m_x and m_y are the cart masses toward the x and y axes. The parameters of the 2D controllers are the same as before. However, the 3D controllers are tuned based on the model

explained above. The only 3D controller considered in the simulations, *i.e.*, coupling tracking, is tuned based on this strategy. This controller in 2D setting is as follows (compare it with Section 7.1.9):

$$\begin{cases} e_v = (v - v_d) \\ \zeta = e_v - \lambda \sin(\theta) \\ F = -k_d \zeta - k_p \int_0^t \zeta dt + m_t a_d + \lambda m_t \cos(\theta)\dot{\theta} \end{cases} \tag{149}$$

Compared to the 2D version of this controller presented in (144)

$$\begin{cases} e_{vx} = (v_x - v_{xd}), \quad e_{vy} = (v_y - v_{yd}) \\ \zeta_x = e_{vx} - \lambda \sin(\theta_x), \quad \zeta_y = e_{vy} - \lambda \sin(\theta_y) \\ F_x = -k_{dx}\zeta_x - k_{px} \int_0^t \zeta_x dt + m_t a_{dx} + \lambda m_t \cos(\theta_x)\cos(\theta_y)\dot{\theta}_x \\ F_y = -k_{dy}\zeta_y - k_{py} \int_0^t \zeta_y dt + m_t a_{dy} + \lambda m_t \dot{\theta}_y \end{cases} \tag{150}$$

The parameters $k_{px} = 1749, k_{dx} = 3449, k_{py} = 0, k_{dy} = 2911, \lambda = 0$ have been obtained for the 3D setting. It can be seen that $\lambda = 0$ has been obtained for this controller meaning that considering the comping in the 3D space between the x and y axes does not provide any advantage.

The 3D model has been developed in Matlab Multibody toolbox to study the performances of the controllers in 3D space. To this aim, spherical joints are used instead of the revolute joint to be able to simulate the sway in both x and y axes. Furthermore, other 3D rotations, *i.e.*, skew, trim, and list, can be studied using this model as shown in Fig. 5. As the result, the some of the masses are not lumped anymore, and they are distributed uniformly along the objects. Assuming that the gravity $-g$ is toward the Z axis, the specifications of the bodies are as follows:

- **Cart**: a point mass body
- **Payload**: a solid $[1, 1, 0.5]$m (along $[x, y, z]$ axes) cube uniformly distributed mass. For the unbalanced payload, an extra point mass is attached to the payload trough a one meter massless link. In this case, the mass of the extra object is equal to the balanced payload mass multiplied by a factor (unbalanced factor=0.1) and the new payload mass would be the normal payload mass multiplied by 1-unbalanced factor=0.9.
- **Hook**: a solid $[0.2, 0.2, 0.1]$m cube uniformly distributed mass.
- **Joints**: massless spherical joint are used.
- **Links**: cylindrical links with 20cm of radius are used with uniformly distributed masses.

Compared with the desired trajectory in x axis, defined in (146), the trajectory in the other axis is defined as follows:

$$\begin{cases} y_d(t) = \dfrac{x_d(t-2)}{2} & \text{for} \quad t \geq 2 \\ y_d(t) = 0 & \text{for} \quad t < 2 \end{cases} \tag{151}$$

Note that the objective functions in this simulation are different from the 2D one. The L_2 and L_∞ denote the standard norms and the measurements are sampled with the same sampling rate as the controller, *i.e.*, $h = 50$ms. It should be noted that the measurement of angles in 3D space follows several conventions, *e.g.*, pure rotation trough arbitrary axes, quaternion, and rotation matrix. To study the payload rotation in 3D space, in this section, the pure rotation of the payload trough all axes are measured, which is shown by ϕ indicates the total rotations along all axes. In other words, $\phi(t)$ means pure rotation of the payload at the time step t, along an arbitrary axis. Hence, $\phi(t) \in [0, \pi]$.

8.2 Regulation without perturbation

The results for the regulation trajectory (151) are shown in Table 52. This simulation is conducted for the nominal condition with full payload. It can be seen that the open-loop methods show the worst responses in case of the payload and cart position error. Note that, according to Table 36, while the open-loop methods show relatively good responses for the 2D case under nominal condition, they are almost the worst for the unperturbed 3D case. This is probably caused by the coupling effect between x and y axes that produces a coupling disturbance between the axes. Hence, feedback is crucial for the 3D case, even for the unperturbed condition.

Another observation from Table 52 is that the collocated PD control shows one of the best responses for the payload and cart position tracking. Moreover, Collocated PD, Noncollocated PD regulation (first angle) and PD energy controllers show the smallest amount of payload rotation ($L_2(\phi)$). Comparing these methods, one can see they shows the smallest amounts of control energy ($L_2(\phi)$). Hence, smaller amount of control energy leads to a smaller payload rotation for this unperturbed case. As before, the SMC designed for the double pendulum system shows the worst responses. Comparing the Coupling tracking implemented in a decentralized way (first and last) with the centralized form taking coupling into account in 3D space) one can see that there is no significant difference between these implementations.

Table 52: Comparing the methods in 3D case (reference trajectory: piecewise, heavy load, no initial sway, damping coefficient=1.6 NM/(deg/s), joint stiffness=0.8 NM/deg, cart mass=10000.00, SNR=Inf, cart damping=0.00, no dis.).

Method	$L_2(e_p)$	$L_2(e_c)$	$L_2(F)$	$L_\infty(F)$	$L_2(\phi)$	$L_\infty(\phi)$
Unshaped input	223.84	227.01	1.06e+06	8.38e+04	8.41	0.32
ZV	144.75	147.45	8.47e+05	8.38e+04	4.72	0.23
ZVD	209.58	209.21	7.40e+05	6.29e+04	3.56	0.21
Collocated PD	142.18	138.59	8.66e+05	7.84e+04	1.08	0.10
Quasi-PID	87.58	79.41	1.07e+06	9.55e+04	1.33	0.12
Non.CO.PD.Reg.1	143.40	139.85	8.61e+05	7.78e+04	1.07	0.10
Non.CO.PD.Reg.n	92.05	72.95	1.37e+06	1.27e+05	1.72	0.16
Col.PD.Track	36.70	23.55	1.20e+06	1.16e+05	1.93	0.17
PD-PD	93.60	74.03	1.39e+06	1.29e+05	1.74	0.16
SMC-single-first (explicit)	93.36	73.65	1.39e+06	1.29e+05	1.75	0.16
SMC-single-first (implicit)	93.30	73.60	1.39e+06	1.29e+05	1.75	0.16
SMC-single-last (explicit)	92.04	72.97	1.37e+06	1.27e+05	1.72	0.16
SMC-single-last (implicit)	91.85	72.74	1.37e+06	1.27e+05	1.72	0.16
SMC-double (explicit)	178.71	179.54	8.85e+06	2.00e+05	84.57	3.14
SMC-double (implicit)	76.20	73.72	7.74e+06	2.00e+05	81.65	3.14
PD energy (first)	131.31	127.88	8.48e+05	7.56e+04	1.05	0.09
PD energy (last)	141.57	138.02	8.37e+05	7.56e+04	1.03	0.09
Coupling tracking (first)	78.73	76.62	1.08e+06	1.03e+05	1.65	0.17
Coupling tracking (last)	74.28	71.81	1.12e+06	1.09e+05	1.71	0.17
Coupling tracking (3D)	69.68	71.54	1.06e+06	9.25e+04	2.99	0.20

8.3 Tracking performances

The results for the sinusoidal trajectory tracking with frequency $\omega = 0.2$rad/s are listed in Table 53. Similar to the regulation in 3D space, the open-loop methods show the worst payload and cart position error. On the other hand, the Quasi-PID method shows almost the best responses. One of the interesting observation is that the tracking controllers, *i.e.*, collocated PD tracking and coupling tracking do not show the best responses for the tracking in 3D space mainly because of the coupling effect. In fact, according to table 15, the tracking controllers depend on the feedforward term ($m_t a_d$) which improves their performances. However, for the 3D case, the performances are degraded because of the coupling between the x and y axes (we already saw from Table 51 that the tracking controllers are sensitive to the perturbations). Considering the coupling in the control design would probably improve the results. As before, the SMC designed for the double pendulum

system shows the worst responses. Comparing the Coupling tracking implemented in a decentralized way (first and last) with the centralized form taking coupling into account in 3D space) it can be seen that the centralized implementation

Table 53: Comparing the methods (reference trajectory: sinusoidal with initial error, heavy load, no initial sway, damping coefficient=1.6 NM/(deg/s), joint stiffness=0.8 NM/deg, cart mass=10000.00, SNR=Inf, cart damping=0.00, dis. on load).

Method	$L_2(e_p)$	$L_2(e_c)$	$L_2(F)$	$L_\infty(F)$	$L_2(\phi)$	$L_\infty(\phi)$
Unshaped input	1477.76	1477.04	5.99e+05	1.92e+04	0.87	0.04
ZV	936.36	936.23	3.82e+04	1.19e+03	0.05	0.00
ZVD	906.18	906.07	3.76e+04	1.19e+03	0.04	0.00
Collocated PD	123.33	120.06	7.38e+05	4.24e+04	1.21	0.06
Quasi-PID	64.06	54.26	9.34e+05	7.71e+04	1.74	0.09
Non.CO.PD.Reg.1	124.49	121.25	7.36e+05	4.19e+04	1.20	0.06
Non.CO.PD.Reg.n	73.59	58.49	1.01e+06	6.60e+04	1.62	0.09
Col.PD.Track	85.24	74.81	9.29e+05	4.00e+04	1.40	0.07
PD-PD	74.19	58.84	1.01e+06	6.10e+04	1.59	0.09
SMC-single-first (explicit)	73.71	58.26	1.01e+06	5.98e+04	1.64	0.09
SMC-single-first (implicit)	73.66	58.21	1.01e+06	5.99e+04	1.65	0.09
SMC-single-last (explicit)	73.60	58.52	1.01e+06	6.60e+04	1.62	0.09
SMC-single-last (implicit)	73.36	58.25	1.01e+06	6.62e+04	1.62	0.09
SMC-double (explicit)	223.39	223.59	8.86e+06	2.00e+05	85.29	3.14
SMC-double (implicit)	140.08	139.33	7.96e+06	2.00e+05	85.46	3.14
PD energy (first)	209.24	192.07	3.36e+06	2.00e+05	15.90	1.09
PD energy (last)	133.10	127.63	7.88e+05	4.10e+04	1.24	0.06
Coupling tracking (first)	212.83	193.25	1.31e+06	6.47e+04	1.57	0.08
Coupling tracking (last)	144.03	128.90	1.11e+06	5.18e+04	1.50	0.08
Coupling tracking (3D)	123.25	121.87	5.67e+05	2.21e+04	0.68	0.03

The responses of the controllers for the sinusoidal trajectory with different frequencies $\omega = 0.05 - 0.5$ rad/s are shown in Fig. 18. This figure is quite similar to the one for the 2D case Fig. 17, where the tracking controllers are almost insensitive to the frequency, and they show the best payload position tracking performances for large frequencies.

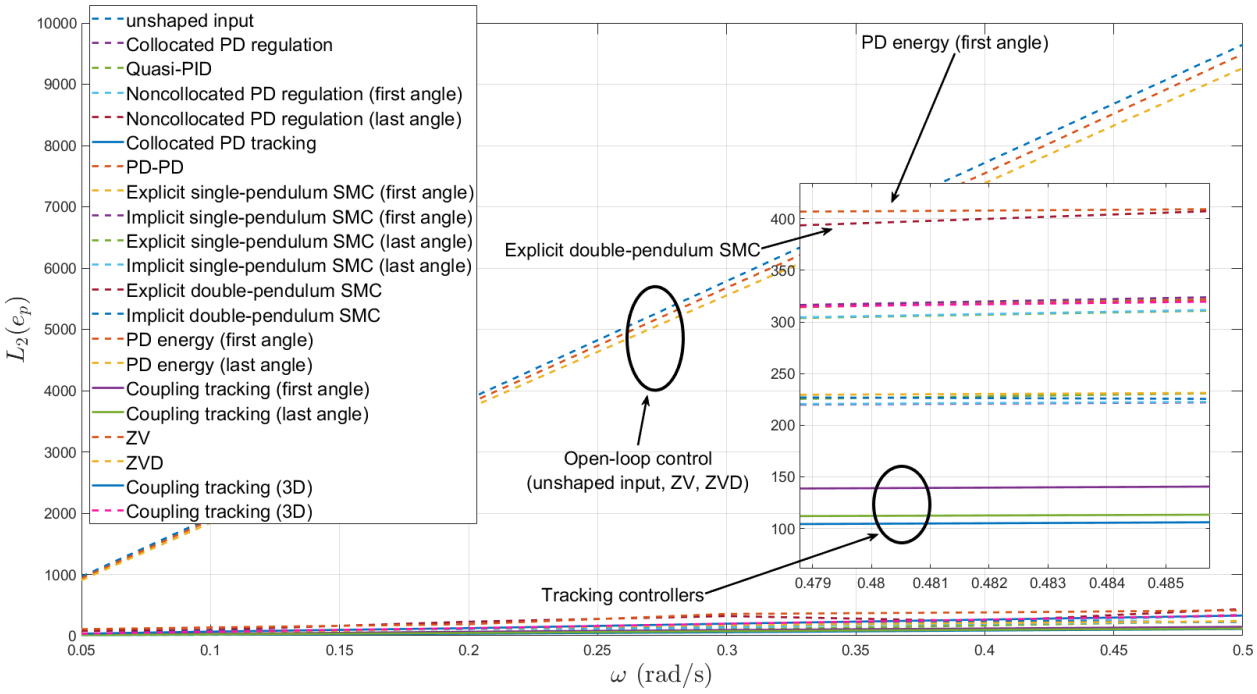

Figure 18: Tracking performances for the decentralized controllers applied to the 3D case.

8.4 Robustness to initial sway

The initial sway is considered in this simulation by rotation the spherical joints only along the Y axes. In this simulation, 30 degrees of initial sway is considered on the first joint while the initial sway corresponding to other joints are zero. As can be seen in Table 54, the open-loop methods as well as the double pendulum SMC show the worst responses in case of payload position error. It should be noted that the open-loop methods show the smallest amount of control effort, the closed-loop schemes tried to inject damping to cancel the effect of the initial sway leading to a higher energy consumption for the closed-loop methods. Considering the payload and cart position error, the collocated PD controller shows the best response.

Table 54: Comparing the methods (reference trajectory: piecewise, heavy load, 30 degrees on the first angle, damping coefficient=1.6 NM/(deg/s), joint stiffness=0.8 NM/deg, cart mass=10000.00, SNR=Inf, cart damping=0.00, no dis.).

Method	$L_2(e_p)$	$L_2(e_c)$	$L_2(F)$	$L_\infty(F)$	$L_2(\phi)$	$L_\infty(\phi)$
Unshaped input	422.46	451.86	1.06e+06	8.38e+04	37.59	1.25
ZV	265.62	356.05	8.47e+05	8.38e+04	73.16	2.75
ZVD	326.23	419.58	7.40e+05	6.29e+04	66.92	3.14
Collocated PD	177.38	174.46	1.08e+06	1.26e+05	2.50	0.52
Quasi-PID	157.60	153.08	1.17e+06	1.07e+05	2.89	0.52
Non.CO.PD.Reg.1	178.31	175.42	1.07e+06	1.26e+05	2.50	0.52
Non.CO.PD.Reg.n	112.72	94.05	1.59e+06	1.42e+05	3.43	0.52
Col.PD.Track	72.33	59.44	1.39e+06	1.39e+05	7.47	0.52
PD-PD	113.38	94.23	1.59e+06	1.43e+05	3.33	0.52
SMC-single-first (explicit)	112.74	93.46	1.58e+06	1.43e+05	3.47	0.52
SMC-single-first (implicit)	112.70	93.41	1.59e+06	1.43e+05	3.47	0.52
SMC-single-last (explicit)	112.74	94.11	1.58e+06	1.42e+05	3.43	0.52
SMC-single-last (implicit)	112.56	93.87	1.59e+06	1.42e+05	3.43	0.52
SMC-double (explicit)	315.18	313.59	8.85e+06	2.00e+05	83.40	3.14
SMC-double (implicit)	146.01	144.63	7.88e+06	2.00e+05	81.61	3.14
PD energy (first)	136.21	132.10	1.14e+06	1.26e+05	5.99	0.52
PD energy (last)	183.56	180.95	1.05e+06	1.26e+05	2.47	0.52
Coupling tracking (first)	108.80	99.96	1.32e+06	1.34e+05	7.02	0.52
Coupling tracking (last)	98.64	90.60	1.33e+06	1.36e+05	9.36	0.52
Coupling tracking (3D)	117.55	115.79	1.17e+06	1.24e+05	4.76	0.52

8.5 Matched disturbance

In this simulation, the matched disturbance for the x axis is the same as the one for the 2D case. Assuming that the disturbance towards the x axis is $f(t)$, the disturbance towards the y axis is $\frac{f(t-2)}{2}$ for $t \geq 2$s and $f(t) = 0$ for $t < 2$s. One can see that under such disturbance, the open-loop and the double pendulum SMC show the worst responses. Moreover, considering the cart and payload tracking, the quasi-PID shows the best response. Other methods show the same level of performance. It should also be noted that $L_\infty(\phi)$ pure payload rotation along an arbitrary axis for at leas π rad.

Table 55: Comparing the methods (reference trajectory: piecewise, heavy load, no initial sway, damping coefficient=1.6 NM/(deg/s), joint stiffness=0.8 NM/deg, cart mass=10000.00, SNR=Inf, cart damping=0.00, dis. on cart).

Method	$L_2(e_p)$	$L_2(e_c)$	$L_2(F)$	$L_\infty(F)$	$L_2(\phi)$	$L_\infty(\phi)$
Unshaped input	5743.76	5741.24	1.06e+06	8.38e+04	64.62	3.14
ZV	6045.46	6045.45	8.47e+05	8.38e+04	59.22	3.14
ZVD	6040.89	6035.56	7.40e+05	6.29e+04	57.38	3.14
Collocated PD	171.84	156.15	1.26e+06	9.41e+04	2.29	0.17
Quasi-PID	106.13	89.10	1.68e+06	1.08e+05	3.52	0.19
Non.CO.PD.Reg.1	173.34	157.66	1.26e+06	9.38e+04	2.29	0.17
Non.CO.PD.Reg.n	124.79	100.87	2.00e+06	1.35e+05	3.14	0.22
Col.PD.Track	196.08	170.49	2.06e+06	1.51e+05	3.38	0.24
PD-PD	131.22	106.57	2.04e+06	1.37e+05	3.02	0.22
SMC-single-first (explicit)	131.72	107.00	2.05e+06	1.38e+05	3.10	0.22
SMC-single-first (implicit)	131.62	106.90	2.05e+06	1.38e+05	3.10	0.22
SMC-single-last (explicit)	124.76	100.87	2.00e+06	1.35e+05	3.14	0.22
SMC-single-last (implicit)	124.45	100.55	2.00e+06	1.35e+05	3.14	0.22
SMC-double (explicit)	438.26	430.90	8.85e+06	2.00e+05	84.36	3.14
SMC-double (implicit)	144.45	133.18	7.67e+06	2.00e+05	81.34	3.14
PD energy (first)	165.83	146.23	1.52e+06	1.33e+05	6.53	0.24
PD energy (last)	174.22	156.28	1.31e+06	9.68e+04	2.32	0.17
Coupling tracking (first)	505.77	451.19	2.93e+06	1.50e+05	4.32	0.23
Coupling tracking (last)	336.19	298.85	2.46e+06	1.51e+05	3.50	0.24
Coupling tracking (3D)	363.72	335.10	1.38e+06	1.20e+05	4.39	0.26

8.6 Mismatched disturbance

The mismatched disturbance along the y axis is generated with the same method is explained for the matched one in the previous section. The only difference between this case and the matched disturbance is that the collocated PD tracking shows one of the best responses.

Table 56: Comparing the methods (reference trajectory: piecewise, heavy load, no initial sway, damping coefficient=1.6 NM/(deg/s), joint stiffness=0.8 NM/deg, cart mass=10000.00, SNR=Inf, cart damping=0.00, dis. on load).

Method	$L_2(e_p)$	$L_2(e_c)$	$L_2(F)$	$L_\infty(F)$	$L_2(\phi)$	$L_\infty(\phi)$
Unshaped input	2165.51	2165.83	1.06e+06	8.38e+04	7.94	0.30
ZV	2469.13	2469.21	8.47e+05	8.38e+04	4.23	0.23
ZVD	2466.56	2466.41	7.40e+05	6.29e+04	3.21	0.21
Collocated PD	130.52	127.49	9.08e+05	7.70e+04	1.21	0.09
Quasi-PID	83.05	73.37	1.19e+06	9.42e+04	1.61	0.13
Non.CO.PD.Reg.1	131.61	128.63	9.03e+05	7.65e+04	1.20	0.09
Non.CO.PD.Reg.n	96.54	76.25	1.48e+06	1.24e+05	1.95	0.15
Col.PD.Track	94.85	79.03	1.43e+06	1.31e+05	2.36	0.18
PD-PD	98.31	77.50	1.50e+06	1.25e+05	1.98	0.15
SMC-single-first (explicit)	98.19	77.21	1.50e+06	1.26e+05	1.98	0.16
SMC-single-first (implicit)	98.13	77.15	1.50e+06	1.26e+05	1.98	0.16
SMC-single-last (explicit)	96.50	76.25	1.48e+06	1.24e+05	1.95	0.15
SMC-single-last (implicit)	96.34	76.02	1.48e+06	1.24e+05	1.95	0.15
SMC-double (explicit)	210.03	208.85	8.85e+06	2.00e+05	84.81	3.14
SMC-double (implicit)	89.49	87.82	7.75e+06	2.00e+05	82.45	3.14
PD energy (first)	119.45	115.63	9.14e+05	7.44e+04	1.23	0.09
PD energy (last)	128.04	123.53	9.24e+05	7.42e+04	1.23	0.09
Coupling tracking (first)	229.97	209.47	1.66e+06	1.23e+05	2.23	0.18
Coupling tracking (last)	163.06	146.97	1.52e+06	1.27e+05	2.25	0.18
Coupling tracking (3D)	158.43	151.88	1.16e+06	1.03e+05	2.82	0.21

8.7 Robustness to noise

All measurement in this simulation are affected by a Gaussian noise with SNR=90db. One can see that the Collocated PD has achieved the best responses.

Table 57: Comparing the methods (reference trajectory: piecewise, heavy load, no initial sway, damping coefficient=1.6 NM/(deg/s), joint stiffness=0.8 NM/deg, cart mass=10000.00, SNR=90.00, cart damping=0.00, no dis.).

Method	$L_2(e_p)$	$L_2(e_c)$	$L_2(F)$	$L_\infty(F)$	$L_2(\phi)$	$L_\infty(\phi)$
Unshaped input	223.84	227.01	1.06e+06	8.38e+04	8.41	0.32
ZV	144.75	147.45	8.47e+05	8.38e+04	4.72	0.23
ZVD	209.58	209.21	7.40e+05	6.29e+04	3.56	0.21
Collocated PD	142.18	138.59	8.66e+05	7.84e+04	1.08	0.10
Quasi-PID	87.58	79.41	1.07e+06	9.55e+04	1.33	0.12
Non.CO.PD.Reg.1	143.40	139.85	8.61e+05	7.78e+04	1.07	0.10
Non.CO.PD.Reg.n	92.05	72.95	1.37e+06	1.27e+05	1.72	0.16
Col.PD.Track	36.70	23.55	1.20e+06	1.16e+05	1.93	0.17
PD-PD	93.60	74.03	1.39e+06	1.29e+05	1.74	0.16
SMC-single-first (explicit)	93.36	73.65	1.39e+06	1.29e+05	1.75	0.16
SMC-single-first (implicit)	93.30	73.60	1.39e+06	1.29e+05	1.75	0.16
SMC-single-last (explicit)	92.04	72.97	1.37e+06	1.27e+05	1.72	0.16
SMC-single-last (implicit)	91.85	72.74	1.37e+06	1.27e+05	1.72	0.16
SMC-double (explicit)	175.86	176.69	8.87e+06	2.00e+05	84.16	3.14
SMC-double (implicit)	76.08	73.59	7.74e+06	2.00e+05	81.64	3.14
PD energy (first)	131.31	127.88	8.48e+05	7.56e+04	1.05	0.09
PD energy (last)	141.57	138.02	8.37e+05	7.56e+04	1.03	0.09
Coupling tracking (first)	78.73	76.62	1.08e+06	1.03e+05	1.65	0.17
Coupling tracking (last)	74.28	71.81	1.12e+06	1.09e+05	1.71	0.17
Coupling tracking (3D)	69.68	71.54	1.06e+06	9.25e+04	2.99	0.20

8.8 Robustness to no load condition

In this case, the weights of the payload and the hook are 20kg. According to Table 58, the results have been changed significantly, compared to the previous cases.

Table 58: Comparing the methods (reference trajectory: piecewise, light load, no initial sway, damping coefficient=1.6 NM/(deg/s), joint stiffness=0.8 NM/deg, cart mass=10000.00, SNR=Inf, cart damping=0.00, no dis.).

Method	$L_2(e_p)$	$L_2(e_c)$	$L_2(F)$	$L_\infty(F)$	$L_2(\phi)$	$L_\infty(\phi)$
Unshaped input	216.00	189.36	1.71e+05	1.36e+04	7.13	0.27
ZV	209.58	209.21	7.40e+05	6.29e+04	3.56	0.21
ZVD	223.25	220.25	1.20e+05	1.02e+04	1.02	0.09
Collocated PD	106.01	39.56	1.69e+05	1.52e+04	6.96	0.27
Quasi-PID	104.90	18.69	1.87e+05	2.81e+04	7.28	0.28
Non.CO.PD.Reg.1	106.03	39.80	1.69e+05	1.51e+04	6.95	0.27
Non.CO.PD.Reg.n	108.92	14.97	1.86e+05	2.95e+04	7.57	0.29
Col.PD.Track	109.88	10.51	1.86e+05	2.81e+04	7.76	0.30
PD-PD	502.99	78.90	2.58e+06	2.00e+05	65.59	3.14
SMC-single-first (explicit)	581.12	140.96	4.39e+06	2.00e+05	75.20	3.14
SMC-single-first (implicit)	580.91	141.34	4.45e+06	2.00e+05	75.35	3.14
SMC-single-last (explicit)	109.03	14.98	1.86e+05	2.95e+04	7.58	0.29
SMC-single-last (implicit)	109.10	14.93	1.86e+05	2.96e+04	7.58	0.29
SMC-double (explicit)	11916.98	11899.15	8.34e+06	2.00e+05	93.86	3.14
SMC-double (implicit)	10015.01	9995.69	4.22e+06	2.00e+05	85.90	3.14
PD energy (first)	306.56	36.94	4.84e+05	7.10e+04	29.35	1.78
PD energy (last)	108.46	29.67	1.73e+05	1.56e+04	7.30	0.28
Coupling tracking (first)	89.66	68.10	1.76e+05	1.64e+04	4.32	0.27
Coupling tracking (last)	127.07	67.07	1.78e+05	1.77e+04	7.65	0.30
Coupling tracking (3D)	125.75	66.18	1.81e+05	1.52e+04	7.53	0.30

8.9 Unbalanced payload

To simulate the unbalanced payload, a one meter massless bar is connected to the center of payload along the $-y$ axis, and a lumped mass is connected to the end of the bar. The mass of this extra object is equal to the payload mass, in balanced condition, multiplied by the unbalanced factor, while the payload mass is equal to the total payload mass in the balanced condition multiplied by $1-$ unbalanced factor. In this simulation, unbalanced factor is equal to 0.1.

Table 59: Comparing the methods (reference trajectory: piecewise, heavy load, no initial sway, damping coefficient=1.6 NM/(deg/s), joint stiffness=0.8 NM/deg, cart mass=10000.00, SNR=Inf, cart damping=0.00, no dis.).

Method	$L_2(e_p)$	$L_2(e_c)$	$L_2(F)$	$L_\infty(F)$	$L_2(\phi)$	$L_\infty(\phi)$
Unshaped input	226.08	229.44	1.06e+06	8.38e+04	88.05	3.14
ZV	145.55	146.91	8.47e+05	8.38e+04	79.23	3.14
ZVD	207.96	209.31	7.40e+05	6.29e+04	95.97	3.14
Collocated PD	141.71	138.61	8.68e+05	8.11e+04	11.94	0.38
quasi-PID	87.39	79.40	1.08e+06	1.00e+05	5.98	0.21
Non.CO.PD.Reg.1	142.93	139.87	8.64e+05	8.06e+04	11.83	0.37
Non.CO.PD.Reg.n	92.13	72.86	1.37e+06	1.29e+05	20.30	0.65
Col.PD.Track	37.00	23.56	1.21e+06	1.15e+05	42.37	1.56
PD-PD	93.68	73.94	1.39e+06	1.31e+05	23.05	0.75
SMC-single-first (explicit)	93.43	73.56	1.39e+06	1.31e+05	24.96	0.81
SMC-single-first (implicit)	93.38	73.50	1.39e+06	1.31e+05	24.94	0.81
SMC-single-last (explicit)	92.12	72.88	1.37e+06	1.29e+05	20.23	0.65
SMC-single-last (implicit)	91.94	72.64	1.37e+06	1.29e+05	20.19	0.65
SMC-double (explicit)	120.04	119.14	8.87e+06	2.00e+05	82.75	3.14
SMC-double (implicit)	133.70	133.43	7.80e+06	2.00e+05	82.67	3.14
PD energy (first)	130.76	127.68	8.48e+05	7.71e+04	15.90	0.51
PD energy (last)	140.74	137.96	8.39e+05	7.83e+04	12.85	0.41
Coupling tracking (first)	81.11	76.60	1.08e+06	1.04e+05	78.54	2.79
Coupling tracking (last)	76.89	71.77	1.12e+06	1.08e+05	81.45	2.89
Coupling tracking 3D	68.76	71.71	1.06e+06	9.30e+04	70.09	3.14

Note that $L_\infty = 3.14$ shows that the payload rotates at least for π rad along an arbitrary axis, indicating that the payload flips. A control system leading to such a response should probably be avoided because of too much rotation.

8.10 Summarized results

The summarized results of the numerical simulations for the 3D case are provided in Table 60. Comparing the results obtained for the 3D case with the ones presented for 2D operating space in Section 7.11, one can see that the results almost match, except for the following cases:

- Unlike the 2D case, the open-loop methods are not efficient in cart and payload position tracking, even for the regulation case. The reason is that for the 3D case, the coupling between x and y axes

applies a kind of disturbance to the system. Since the open-loop methods cannot compensate for the disturbances, they presented the worst responses for all cases.

- Comparing the performances of the coupling tracking controller, one can see that this controller showed better responses for the 3D operating space because it is designed to handle the coupling effect between the x and y axes.

9 Conclusions

In this work, a complete review of the modeling strategies used for overhead cranes including the pendulum-like models (single and double-pendulum models and flexible link model) has been made. Subsequently, it is shown that while the existing models may be used for the controller design, they are not accurate enough to be used for the numerical simulations. Hence, a new simulation-oriented model has been proposed enabling one to take into account more details that exist in a real system, *e.g.*, global nonlinearities, high-frequencies vibrations caused by the cable dynamics. The mathematical equations of the proposed model have been developed and formulated and the characteristics of the model under different conditions have been studied analytically. Subsequently, a complete introduction to the control methods developed for overhead cranes has been presented and classified in tabular forms based on their properties, stability, feedback type, validity, etc. Such a classification allows one to select the most appropriate controller for each specific application. Afterward, some controllers have been selected from each category and a comparative analysis is made under different conditions to extract the key characteristics of each category of controllers.

The following open issues are identified during this research that should be addressed in the future:

- Krasovskii-LaSalle invariance principle and passivity-based control, with the N-pendulum multibody cable's model has only been studied for the single and double-pendulum systems, and it is not clear how to use them to validate the controllers for a higher number of links, like the 20-link pendulum system used for the numerical simulations.

- FEM cable's model for control and simulation (the ALE-ANCF approach allows for large deformations and yields an apparently tractable Lagrange dynamics, with possible cable-pulleys interactions if such detailed modeling is needed Fotland et al. [2020], Fotland and Haugen [2022]) may be considered in future works;

- The methods developed for multi-cable parallel robotic systems may be employed to handle the cranes with several parallel cranes which are widely used. To this end, the kinematic and dynamic modeling of such crane structures should be addressed in the future.

- Control strategies with varying cable length require a specific model (the multibody approach with N-pendulum model may not be tractable), the ALE-ANCF FEM approach may be better-suited Fotland

Table 60: Summarized results obtained from the numerical simulations (3D case)

Method	Regulation	Track.	Init. sway	Matched	Mismatched	Noise	load-free	Unbalanced load
Unshaped input	e_p, e_c, ϕ_2	e_p, e_c	$e_p, e_c, \phi_2, F_\infty$	$e_p, e_c, \phi_2, \phi_\infty$	e_p, e_c	e_p, e_c	e_p, e_c	$e_p, e_c, \phi_2, \phi_\infty$
ZV	e_p, e_c, ϕ_2	e_p, e_c	$e_p, e_c, \phi_2, F_\infty$	$e_p, e_c, \phi_2, \phi_\infty$	e_p, e_c	e_p, e_c	$e_p, e_c, \phi_2, \phi_\infty$	e_p, e_c
ZVD	e_p, e_c, ϕ_2	e_p, e_c	$e_p, e_c, \phi_2, \phi_\infty, F_\infty$	$e_p, e_c, \phi_2, \phi_\infty$	e_p, e_c	e_p, e_c	$e_p, e_c, \phi_2, \phi_\infty$	e_p, e_c
Collocated PD	ϕ_2	—	—	—	—	—	—	—
quasi-PID	—	e_p, e_c	—	e_p, e_c	e_p, e_c	—	—	ϕ_2, ϕ_∞
Non.CO.PD.Reg. (first)	ϕ_2	—	—	—	—	—	—	—
Non.CO.PD.Reg. (last)	—	—	—	—	—	—	—	—
Col.PD.Track	e_p, e_c	—	e_p, e_c	—	—	e_p, e_c	—	e_p, e_c
PD-PD	—	—	—	—	—	—	$e_p, F_\infty, \phi_2, \phi_\infty$	—
SMC-single-first (explicit)	—	—	—	—	—	—	$e_p, e_c, F_\infty, \phi_2, \phi_\infty$	—
SMC-single-first (implicit)	—	—	—	—	—	—	$e_p, e_c, F_\infty, \phi_2, \phi_\infty$	—
SMC-single-last (explicit)	—	—	—	—	—	—	—	—
SMC-single-last (implicit)	—	—	—	—	—	—	—	—
SMC-double (explicit)	$e_p, e_c, F_2, F_\infty, \phi_2, \phi_\infty$	$e_p, e_c, F_2, F_\infty, \phi_2, \phi_\infty$	$e_p, e_c, F_2, F_\infty, \phi_2, \phi_\infty$	$F_2, F_\infty, \phi_2, \phi_\infty$	$F_2, F_\infty, \phi_2, \phi_\infty$	$e_p, e_c, F_2, F_\infty, \phi_2, \phi_\infty$	$e_p, e_c, F_2, F_\infty, \phi_2, \phi_\infty$	$F_2, F_\infty, \phi_2, \phi_\infty$
SMC-double (implicit)	$F_2, F_\infty, \phi_2, \phi_\infty$	$F_2, F_\infty, \phi_2, \phi_\infty$	$F_2, F_\infty, \phi_2, \phi_\infty$	$F_2, F_\infty, \phi_2, \phi_\infty$	$F_2, F_\infty, \phi_2, \phi_\infty$	$F_2, F_\infty, \phi_2, \phi_\infty$	$e_p, e_c, F_2, F_\infty, \phi_2, \phi_\infty$	$F_2, F_\infty, \phi_2, \phi_\infty$
PD energy (first)	—	F_∞	—	—	—	—	e_p	—
PD energy (last)	—	—		—	—	—	—	—
Coupling tracking (first)	—	—	—	—	—	—	—	ϕ_2
Coupling tracking (last)	—	—	—	—	—	—	—	ϕ_2
Coupling tracking (3D)	—	—	—	—	—	—	—	ϕ_2,ϕ_∞

et al. [2020], Hong et al. [2011].

Acknowledgement

This work was supported by the project IRT NanoElec Levage, Grenoble, France.

References

E. Abdel-Rahman and A. Nayfeh. Cargo-pendulation reduction in boom cranes via cable-length manipulation. In *41st Structures, Structural Dynamics, and Materials Conference and Exhibit*, 2000.

E. M. Abdel-Rahman, A. H. Nayfeh, and Z. N. Masoud. Dynamics and control of cranes: A review. *Journal of Vibration and Control*, 9(7):863–908, 2003.

A. M. Abdullahi, Z. Mohamed, H. Selamat, H. R. Pota, M. Zainal Abidin, F. Ismail, and A. Haruna. Adaptive output-based command shaping for sway control of a 3d overhead crane with payload hoisting and wind disturbance. *Mechanical Systems and Signal Processing*, 98:157–172, 2018.

J. Ackermann. *Robust control: Systems with uncertain physical parameters*. Springer Science & Business Media, 2012.

A. Al-Garni, K. Moustafa, and S. Javeed Nizami. Optimal control of overhead cranes. *Control Engineering Practice*, 3(9):1277–1284, 1995.

K. Alhazza, Z. Masoud, and N. Alotaibi. A smooth wave-form shaped command with flexible maneuvering time: Analysis and experiments. *Asian Journal of Control*, 18(4):1376–1384, 2016.

H. Alli and T. Singh. Passive control of overhead cranes. In *Proceedings of the 1998 IEEE International Conference on Control Applications*, volume 2, pages 1046–1050 vol.2, 1998. doi: 10.1109/CCA.1998.721617.

A. Alshaya and K. Alghanim. Command shaping for sloshing suppression of a suspended liquid container. *Journal of Dynamic Systems, Measurement, and Control*, 142(12), 2020.

A. Arena, A. Casalotti, W. Lacarbonara, and M. P. Cartmell. Three-Dimensional Modeling of Container Cranes. In *9th International Conference on Multibody Systems, Nonlinear Dynamics, and Control*, volume 7A of *International Design Engineering Technical Conferences and Computers and Information in Engineering Conference*, 08 2013.

A. Arena, A. Casalotti, W. Lacarbonara, and M. Cartmell. Dynamics of container cranes: three-dimensional modeling, full-scale experiments, and identification. *International Journal of Mechanical Sciences*, 93:8–21, 2015. ISSN 0020-7403.

H. Aschemann. Passivity-based trajectory control of an overhead crane by interconnection and damping assignment. In H. Ulbrich and L. Ginzinger, editors, *Motion and Vibration Control*, pages 21–30. Springer Netherlands, 2009.

J. Auernig and H. Troger. Time optimal control of overhead cranes with hoisting of the load. *Automatica*, 23(4): 437–447, 1987.

B. Balachandran, Y.-Y. Li, and C.-C. Fang. A mechanical filter concept for control of non-linear crane-load oscillations. *Journal of Sound and Vibration*, 228(3):651–682, 1999.

G. Bartolini, N. Orani, A. Pisano, and E. Usai. Load swing damping in overhead cranes by sliding mode technique. In *Proceedings of the 39th IEEE Conference on Decision and Control*, volume 2, pages 1697–1702 vol.2, 2000.

G. Bartolini, A. Pisano, and E. Usai. Second-order sliding-mode control of container cranes. *Automatica*, 38(10): 1783–1790, 2002.

G. Bartolini, A. Pisano, and E. Usai. Output-feedback control of container cranes: A comparative analysis. *Asian Journal of Control*, 5(4):578–593, 2003.

D. Bernstein. *Matrix Mathematics. Theory, Facts and Formulas.* Princeton University Press, 2nd edition, 2009.

C. Bertrand, V. Acary, C.-H. Lamarque, and A. T. Svadkoohi. A robust and efficient numerical finite element method for cables. *Int. J. for Num. Methods in Eng.*, 121(18):4157–4186, 2020.

A. Blumentals, B. Brogliato, and F. Bertails-Descoubes. The contact problem in Lagrangian systems subject to bilateral and unilateral constraints, with or without sliding Coulomb's friction: A tutorial. *Multibody System Dynamics*, 38(1):43–76, 2016.

A. Bockstedte and E. Kreuzer. Hoisting manipulation by modal coupling control for underactuated cranes. In *IUTAM Symposium on Vibration Control of Nonlinear Mechanisms and Structures*, pages 121–130. Springer, 2005.

S. Bonnabel and X. Claeys. The industrial control of tower cranes: An operator-in-the-loop approach [applications in control]. *IEEE Control Systems Magazine*, 40(5):27–39, 2020.

F. Boustany and B. d'Andrea Novel. Adaptive control of an overhead crane using dynamic feedback linearization and estimation design. In *Proceedings 1992 IEEE International Conference on Robotics and Automation*, volume 3, pages 1963–1968, 1992.

B. Brogliato. Inertial couplings between unilateral and bilateral holonomic constraints in frictionless lagrangian systems. *Multibody System Dynamics*, 29(3):289–325, 2013.

B. Brogliato. *Nonsmooth Mechanics. Models, Dynamics and Control.* Communications and Control Engineering. Springer Int. Publishing Switzerland, third edition, 2016.

B. Brogliato. Lagrange dynamics of lumped-mass multibody models of overhead cranes in 2D operational space. Research report, INRIA, May 2022. https://hal.inria.fr/hal-03674652/file/models2.pdf.

B. Brogliato and A. Tanwani. Dynamical systems coupled with monotone operators: Formalisms, applications, well-posedness, and stability. *SIAM Review*, 62(1):3–129, 2020.

B. Brogliato, R. Ortega, and R. Lozano. Global tracking controllers for flexible-joint manipulators: a comparative study. *Automatica*, 31(7):941–956, 1995.

B. Brogliato, R. Lozano, B. Maschke, and O. Egeland. *Dissipative Systems Analysis and Control. Theory and Applications*. Communications and Control Engineering. Springer Nature Switzerland AG, Cham, CH, third edition, 2020.

C. Byrnes, A. Isidori, and J. Willems. Passivity, feedback equivalence, and the global stabilization of minimum phase nonlinear systems. *IEEE Transactions on Automatic Control*, 36(11):1228–1240, 1991.

M. Cartmell, L. Morrish, T. E. Alberts, and A. J. Taylor. Controlling the nonlinear dynamics of gantry cranes. *Machine vibration*, 5(4):197–210, 1996.

R. Caverly, J. Forbes, and D. Mohammadshahi. Dynamic modelling and passivity-based control of a single degree of freedom cable-actuated system. *IEEE Transactions on Control Systems Technology*, 23(3):898–909, 2014.

C.-Y. Chang and K.-H. Chiang. The nonlinear 3-D crane control with an intelligent operating method. In *2008 SICE Annual Conference*, pages 2917–2921, 2008.

H. Chen, B. Gao, and X. Zhang. Dynamical modelling and nonlinear control of a 3d crane. In *2005 International Conference on Control and Automation*, volume 2, pages 1085–1090, 2005.

H. Chen, Y. Fang, and N. Sun. A swing constraint guaranteed mpc algorithm for underactuated overhead cranes. *IEEE/ASME Transactions on Mechatronics*, 21(5):2543–2555, 2016.

H. Chen, Y. Fang, and N. Sun. Optimal trajectory planning and tracking control method for overhead cranes. *IET Control Theory & Applications*, 10(6):692–699, 2016.

H. Chen, B. Xuan, P. Yang, and H. Chen. A new overhead crane emergency braking method with theoretical analysis and experimental verification. *Nonlinear Dynamics*, 98(3):2211–2225, 2019.

J.-y. Chen, W.-l. Yang, H.-y. Ni, and W.-x. Yan. A hierarchical sliding mode control method for bridge crane system. In *2020 IEEE International Conference on High Voltage Engineering and Application (ICHVE)*, pages 1–4, 2020.

W. Chen and M. Saif. Output feedback controller design for a class of mimo nonlinear systems using high-order sliding-mode differentiators with application to a laboratory 3-D crane. *IEEE Transactions on Industrial Electronics*, 55 (11):3985–3997, 2008.

B. Chentouf and Z. J. Han. On the stabilization of an overhead crane system with dynamic and delayed boundary conditions. *IEEE Transactions on Automatic Control*, 65(10):4273–4280, 2020.

Chunshien Li, Chun-Yi Lee, and Kuo-Hsiang Cheng. Pseudoerror-based self-organizing neuro-fuzzy system. *IEEE Transactions on Fuzzy Systems*, 12(6):812–819, 2004.

D. Chwa. Nonlinear tracking control of 3-D overhead cranes against the initial swing angle and the variation of payload weight. *IEEE Transactions on Control Systems Technology*, 17(4):876–883, 2009.

D. Chwa. Sliding-mode-control-based robust finite-time antisway tracking control of 3-D overhead cranes. *IEEE Transactions on Industrial Electronics*, 64(8):6775–6784, 2017.

J. Collado, R. Lozano, and I. Fantoni. Control of convey-crane based on passivity. In *Proceedings of the 2000 American Control Conference. ACC*, volume 2, pages 1260–1264, 2000.

L. Cui and D. Zheng. Visual servoing of a flexible gantry crane with a sway range constraint. *IEEE Control Systems Letters*, 3(1):138–143, 2019.

C. Damaren. On the dynamics and control of flexible multibody systems with closed loops. *International Journal of Robotics Research*, 2000.

B. d'Andréa Novel, F. Boustany, F. Conrad, and B. Rao. Feedback stabilization of a hybrid PDE-ODE system: Application to an overhead crane. *Mathematics of Control, Signals and Systems*, 7(1):1–22, 1994.

J. Diwold, B. Kolar, and M. Schöberl. Discrete-time flatness-based control of a gantry crane. *Control Engineering Practice*, 119:104980, 2022.

B. d' Andréa-Novel and J. Coron. Exponential stabilization of an overhead crane with flexible cable via a back-stepping approach. *Automatica*, 36(4):587–593, 2000.

B. d'Andréa Novel and J. Coron. Stabilization of an overhead crane with a variable length flexible cable. *Computational and Applied Mathematics*, 21(1):101–134, 2002.

B. d'Andrea Novel, F. Boustany, and B. Rao. Control of an overhead crane: Feedback stabilization of a hybrid PDE-ODE system. In *Proceedings of the 1st European Control Conference: ECC*, volume 91, pages 2244–2249, 1991.

B. d'Andréa Novel, I. Moyano, and L. Rosier. Finite-time stabilization of an overhead crane with a flexible cable. *Mathematics of Control, Signals, and Systems*, 31(2):1–19, 2019.

A. M. Ebeid, K. A. F. Moustafa, and H. E. Emara-Shabaik. Electromechanical modelling of overhead cranes. *International Journal of Systems Science*, 23(12):2155–2169, 1992.

O. Egeland and J. Gravdahl. *Modeling and Simulation for Automatic Control*. Marine Cybernetics A.S., 2002. Corrected second printing 2003.

Y. Fang, W. Dixon, D. Dawson, and E. Zergeroglu. Nonlinear coupling control laws for a 3-DOF overhead crane system. In *Proceedings of the 40th IEEE Conference on Decision and Control (Cat. No.01CH37228)*, volume 4, pages 3766–3771 vol.4, 2001.

Y. Fang, E. Zergeroglu, W. E. Dixon, and D. M. Dawson. Nonlinear coupling control laws for an overhead crane system. In *Proceedings of the 2001 IEEE International Conference on Control Applications (CCA'01)*, pages 639–644, 2001.

Y. Fang, W. Dixon, D. Dawson, and E. Zergeroglu. Nonlinear coupling control laws for an underactuated overhead crane system. *IEEE/ASME Transactions on Mechatronics*, 8(3):418–423, 2003.

Y. Fang, B. Ma, P. Wang, and X. Zhang. A motion planning-based adaptive control method for an underactuated crane system. *IEEE Transactions on Control Systems Technology*, 20(1):241–248, 2012.

L. Faravelli and F. Ubertini. Nonlinear state observation for cable dynamics. *Journal of Vibration and Control*, 15 (7):1049–1077, 2009.

L. Faravelli, C. Fuggini, and F. Ubertini. Toward a hybrid control solution for cable dynamics: Theoretical prediction and experimental validation. *Structural Control and Health Monitoring*, 17:386–403, 2010.

M. H. Fatehi, M. Eghtesad, and R. Amjadifard. Modelling and control of an overhead crane system with a flexible cable and large swing angle. *Journal of Low Frequency Noise, Vibration and Active Control*, 33(4):395–409, 2014.

M. Fliess, J. Levine, and P. Rouchon. A simplified approach of crane control via a generalized state-space model. In *[1991] Proceedings of the 30th IEEE Conference on Decision and Control*, pages 736–741 vol.1, 1991.

M. Fliess, J. Lévine, P. Martin, and P. Rouchon. Flatness and defect of non-linear systems: introductory theory and examples. *International journal of control*, 61(6):1327–1361, 1995.

P. Foehn, D. Falanga, N. Kuppuswamy, R. Tedrake, and D. Scaramuzza. Fast trajectory optimization for agile quadrotor maneuvers with a cable-suspended payload. In *Proceedings of Robotics: Science and Systems*, Cambridge, Massachusetts, July 2017. doi: 10.15607/RSS.2017.XIII.030.

G. Fotland and B. Haugen. Numerical integration algorithms and constraint formulations for ALE-ANCF cable element. *Mechanism and Machine Theory*, 170:104659, 2022.

G. Fotland, C. Haskins, and T. Roelvag. Trade study to select best alternative for cable and pulley simulation for cranes on offshore vessels. *Systems Engineering*, 23:177–188, 2020.

S. Garrido, M. Abderrahim, A. Gimenez, R. Diez, and C. Balaguer. Anti-swinging input shaping control of an automatic construction crane. *IEEE Transactions on Automation Science and Engineering*, 5(3):549–557, 2008.

V. Gattulli. Advanced control strategies in cable dynamics. in *Civil Engineering Computations: Tools and Techniques,* B.H.V. Topper (Ed.), pages 243–269, 2007. Saxe-Coburg Publications, Stirlinghshire, Scotland.

V. Gattulli, L. Martinelli, F. Perotti, and F. Vestroni. Nonlinear oscillations of cables under harmonic loading using analytical and finite element models. *Comput. Methods Appl. Mech. Engrg.*, 93(1-2):69–85, 2004.

D. Gueners, B. Bouzgarrou, and H. Chanal. Cable behaviour influence on cable-driven parallel-robots vibrations: Experimental characterization and simulation. *ASME Journal of Mechanisms and Robotics*, 13:041003–1–17, August 2021.

M. Hamdy, R. Shalaby, and M. Sallam. A hybrid partial feedback linearization and deadbeat control scheme for a nonlinear gantry crane. *Journal of the Franklin Institute*, 355(14):6286–6299, 2018.

M. T. Hayajneh, S. M. Radaideh, F. M. AL-Oqla, and I. Nejdawi. Reductions of pendulations of overhead cranes under the effect of air resistance by a cable manipulation manner. In *2008 5th International Symposium on Mechatronics and Its Applications*, pages 1–6, 2008. doi: 10.1109/ISMA.2008.4648840.

A. Hazlerigg. Automatic control of crane operations. *IFAC Proceedings Volumes*, 5(1, Part 1):250–258, 1972.

W. He and S. S. Ge. Cooperative control of a nonuniform gantry crane with constrained tension. *Automatica*, 66: 146–154, 2016.

W. He, S. Zhang, and S. S. Ge. Adaptive control of a flexible crane system with the boundary output constraint. *IEEE Transactions on Industrial Electronics*, 61(8):4126–4133, 2014. doi: 10.1109/TIE.2013.2288200.

M. Hičár and J. Ritók. Robust crane control. *Acta Polytechnica Hungarica*, 3(2):91–101, 2006.

D. Hong, J. Tang, and G. Ren. Dynamic modeling of mass-flowing linear medium with large amplitude displacement and rotation. *Journal of Fluids and Structures*, 27:1137–1148, 2011.

K.-S. Hong and Q. H. Ngo. Dynamics of the container crane on a mobile harbor. *Ocean Engineering*, 53:16–24, 2012.

K.-S. Hong and U. H. Shah. *Dynamics and control of industrial cranes*. Springer, 2019.

K.-T. Hong, C.-D. Huh, and K.-S. Hong. Command shaping control for limiting the transient sway angle of crane systems. *International Journal of Control, Automation, and Systems*, 1(1):43–53, 2003.

R. Huston and J. Kamman. A representation of fluid forces in finite segment cable models. *Computers and Structures*, 14:281–287, 1981.

R. Huston and J. Kamman. Validation of finite segment cable models. *Computers and Structures*, 15:653–660, 1982.

R. Huston, C. Passerello, and M. Harlow. Dynamics of multi-rigid-body systems. *Journal of Applied Mechanics*, 45: 889–894, 1978.

L. Jaulin and Éric Walter. Guaranteed tuning, with application to robust control and motion planning. *Automatica*, 32(8):1217–1221, 1996.

E. Johnson, G. Baker, J. F. Spencer, and Y. Fujino. Semiactive damping of stay cables. *ASCE Journal of Engineering Mechanics*, 133(1):1–23, 2007.

J. Kamman and R. Huston. Modeling of submerged cable dynamics. *Computers and Structures*, 20(103):623–629, 1985.

J. Kamman and R. Huston. Multibody dynamics modeling of variable length cable systems. *Multibody System Dynamics*, 5:211–221, 2001.

Y. Kanno. *Nonsmooth Mechanics and Convex Optimization*. CRC Press, Taylor and Francis Group, 2011.

M. A. Karkoub and M. Zribi. Robust control schemes for an overhead crane. *Journal of Vibration and Control*, 7(3): 395–416, 2001.

S. A. Khalilpour, R. Khorrambakht, H. Damirchi, H. D. Taghirad, and P. Cardou. Tip-trajectory tracking control of a deployable cable-driven robot via output redefinition. *Multibody System Dynamics*, 52:31–58, 2021.

E. Khorshid and A. Al-Fadhli. Optimal command shaping design for a liquid slosh suppression in overhead crane systems. *Journal of Dynamic Systems, Measurement, and Control*, 143(2), 2021.

C. Kim and K. Hong. Boundary control of container cranes from the perspective of controlling an axially moving string system. *Int. J. of Control, Automation, and Systems*, 7(3):437–445, 2009.

G.-H. Kim and K.-S. Hong. Adaptive sliding-mode control of an offshore container crane with unknown disturbances. *IEEE/ASME Transactions on Mechatronics*, 24(6):2850–2861, 2019.

Y.-S. Kim, K.-S. Hong, and S.-K. Sul. Anti-sway control of container cranes: inclinometer, observer, and state feedback. *International Journal of Control, Automation, and Systems*, 2(4):435–449, 2004.

B. Kimiaghalam, A. Homaifar, M. Bikdash, and G. Dozier. Genetic algorithms solution for unconstrained optimal crane control. In *Proceedings of the 1999 Congress on Evolutionary Computation-CEC99*, volume 3, pages 2124–2130 Vol. 3, 1999.

J. Klaassens, G. Honderd, A. El Azzouzi, K. C. Cheok, and G. Smid. 3d modeling visualization for studying controls of the jumbo container crane. In *Proceedings of the 1999 American Control Conference (Cat. No. 99CH36251)*, volume 3, pages 1754–1758, 1999.

K. L. Knierim, K. Krieger, and O. Sawodny. Flatness based control of a 3-DOF overhead crane with velocity controlled drives. *IFAC Proceedings Volumes*, 43(18):363–368, 2010.

F. Kolonic, A. Poljugan, and I. Petrovic. Tensor product model transformation-based controller design for gantry crane control system–an application approach. *Acta Polytechnica Hungarica*, 3(4):95–112, 2006.

Kuo-Kai Shyu, Cheng-Lung Jen, and Li-Jen Shang. Design of sliding-mode controller for anti-swing control of overhead cranes. In *31st Annual Conference of IEEE Industrial Electronics Society, 2005. IECON 2005.*, pages 6 pp.–, 2005.

J. Lamaury and M. Gouttefarde. Control of a large redundantly actuated cable-suspended parallel robot. In *2013 IEEE International Conference on Robotics and Automation*, pages 4659–4664, 2013.

L. Lanza. Internal dynamics of multibody systems. *Systems and Control Letters*, 152:104931, 2021.

T. A. Le, G.-H. Kim, M. Y. Kim, and S.-G. Lee. Partial feedback linearization control of overhead cranes with varying cable lengths. *International Journal of Precision Engineering and Manufacturing*, 13(4):501–507, 2012.

T. A. Le, S.-G. Lee, and S.-C. Moon. Partial feedback linearization and sliding mode techniques for 2d crane control. *Transactions of the Institute of Measurement and Control*, 36(1):78–87, 2014.

H.-H. Lee. Modeling and Control of a Three-Dimensional Overhead Crane. *Journal of Dynamic Systems, Measurement, and Control*, 120(4):471–476, 12 1998.

H.-H. Lee. A new design approach for the anti-swing trajectory control of overhead cranes with high-speed hoisting. *International Journal of Control*, 77(10):931–940, 2004.

H.-H. Lee and S.-K. Cho. A new fuzzy-logic anti-swing control for industrial three-dimensional overhead cranes. In *Proceedings 2001 ICRA. IEEE International Conference on Robotics and Automation (Cat. No.01CH37164)*, volume 3, pages 2956–2961 vol.3, 2001.

H.-H. Lee, S.-K. Cho, and J.-S. Cho. A new anti-swing control of overhead cranes. *IFAC Proceedings Volumes*, 30 (13):115–120, 1997.

H.-H. Lee, Y. Liang, and D. Segura. A sliding-mode antiswing trajectory control for overhead cranes with high-speed load hoisting. *J. Dyn. Sys., Meas., Control.*, 128(4):842–845, 2006.

L.-H. Lee, C.-H. Huang, S.-C. Ku, Z.-H. Yang, and C.-Y. Chang. Efficient visual feedback method to control a three-dimensional overhead crane. *IEEE Transactions on Industrial Electronics*, 61(8):4073–4083, 2014.

S.-G. Lee, V.-H. Dang, S. Moon, B. Kim, et al. Partial feedback linearization control of a three-dimensional overhead crane. *International Journal of Control, Automation and Systems*, 11(4):718–727, 2013.

M. Li, H. Chen, and R. Zhang. An input dead zones considered adaptive fuzzy control approach for double pendulum cranes with variable rope lengths. *IEEE/ASME Transactions on Mechatronics*, pages 1–12, 2022.

Y. Liang and K. Koh. Concise anti-swing approach for fuzzy crane control. *Electronics Letters*, 33(2):167–168, 1997.

F. Lin, P. Chou, C. Chen, and Y. Lin. Three-degree-of-freedom dynamic model-based intelligent nonsingular terminal sliding mode control for a gantry position stage. *IEEE Transactions on Fuzzy Systems*, 20(5):971–985, 2012. doi: 10.1109/TFUZZ.2012.2191412.

Y. Liu and H. Yu. A survey of underactuated mechanical systems. *IET Control Theory and Applications*, 7(7): 921–935, 2013.

R. Lozano and B. Brogliato. Adaptive control of robot manipulators with flexible joints. *IEEE Transactions on Automatic Control*, 37(2):174–181, 1992.

B. Lu, Y. Fang, and N. Sun. Sliding mode control for underactuated overhead cranes suffering from both matched and unmatched disturbances. *Mechatronics*, 47:116–125, 2017.

B. Lu, Y. Fang, and N. Sun. Nonlinear control for underactuated multi-rope cranes: Modeling, theoretical design and hardware experiments. *Control Engineering Practice*, 76:123–132, 2018.

B. Lu, Y. Fang, and N. Sun. Adaptive output-feedback control for dual overhead crane system with enhanced anti-swing performance. *IEEE Transactions on Control Systems Technology*, 28(6):2235–2248, 2020.

N. Lv, J. Liu, H. Xia, J. Ma, and X. Yang. A review of techniques for modeling flexible cables. *Computer-Aided Design*, 122:102826, 2020.

N. Lv, J. Liu, and Y. Jia. Coordinated control of flexible cables with human-like dual manipulators. *ASME Journal of Dynamic Systems, Measurement, and Control*, 143:081006, 2021.

M. J. Maghsoudi, Z. Mohamed, A. Husain, and M. Tokhi. An optimal performance control scheme for a 3d crane. *Mechanical Systems and Signal Processing*, 66-67:7F56–768, 2016.

M. J. Maghsoudi, Z. Mohamed, S. Sudin, S. Buyamin, H. Jaafar, and S. Ahmad. An improved input shaping design for an efficient sway control of a nonlinear 3d overhead crane with friction. *Mechanical Systems and Signal Processing*, 92:364–378, 2017.

G. A. Manson. Time-optimal control of an overhead crane model. *Optimal Control Applications and Methods*, 3(2): 115–120, 1982.

L. Meirovitch. *Fundamentals of vibrations*. Waveland Press, 2010.

J.-P. Merlet. Simulation of discrete-time controlled cable-driven parallel robots on a trajectory. *IEEE Transactions on Robotics*, 33(3):675–688, 2017.

S.-C. Moon, W. G. Lee, S.-G. Lee, et al. Adaptive sliding mode control of overhead cranes with varying cable length. *Journal of Mechanical Science and Technology*, 27(3):885–893, 2013.

L. Morrish, M. P. Cartmell, and A. J. Taylor. Cable stretch asymmetries in multi-cable spreader suspension systems undergoing combined translations and rotations. *Proceedings of the Institution of Mechanical Engineers, Part C: Journal of Mechanical Engineering Science*, 210(3):225–237, 1996.

L. Morrish, M. P. Cartmell, and A. J. Taylor. Geometry and kinematics of multicable spreader lifting gear. *Proceedings of the Institution of Mechanical Engineers, Part C: Journal of Mechanical Engineering Science*, 211(3):185–194, 1997.

K. A. F. Moustafa. Feedback control of overhead cranes swing with variable rope length. In *Proceedings of 1994 American Control Conference - ACC '94*, volume 1, pages 691–695 vol.1, 1994.

A. H. Nayfeh. *Nonlinear interactions: analytical, computational, and experimental methods*. Wiley New York, 2000.

N. Nayfeh, Z. Masoud, and W. Baumann. A Comparison of Three Feedback Controllers for Container Cranes. In *5th International Conference on Multibody Systems, Nonlinear Dynamics, and Control, Parts A, B, and C*, volume 6 of *International Design Engineering Technical Conferences and Computers and Information in Engineering Conference*, pages 935–945, 09 2005.

N. A. Nayfeh and W. T. Baumann. Nonlinear analysis of time-delay position feedback control of container cranes. *Nonlinear dynamics*, 53(1):75–88, 2008.

Q. Ngo and K.-S. Hong. Adaptive sliding mode control of container cranes. *IET control theory & applications*, 6(5): 662–668, 2012.

Q. H. Ngo and K. Hong. Sliding-mode antisway control of an offshore container crane. *IEEE/ASME Transactions on Mechatronics*, 17(2):201–209, 2012.

Q. H. Ngo, K.-S. Hong, K. H. Kim, Y. J. Shin, and S.-H. Choi. Skew control of a container crane. In *2008 International Conference on Control, Automation and Systems*, pages 1490–1494, 2008.

E. Ohnishi, I. Tsuboi, T. Egusa, and M. Uesugi. Automatic control of an overhead crane. *IFAC Proceedings Volumes*, 14(2):1885–1890, 1981.

H. M. Omar. *Control of gantry and tower cranes*. PhD thesis, Virginia Tech, 2003.

H. M. Omar and A. H. Nayfeh. Gantry cranes gain scheduling feedback control with friction compensation. *Journal of Sound and Vibration*, 281(1):1–20, 2005.

H. Ouyang, J. Hu, G. Zhang, L. Mei, and X. Deng. Sliding-mode-based trajectory tracking and load sway suppression control for double-pendulum overhead cranes. *IEEE Access*, 7:4371–4379, 2019.

H. Ouyang, J. Hu, G. Zhang, L. Mei, and X. Deng. Decoupled linear model and s-shaped curve motion trajectory for load sway reduction control in overhead cranes with double-pendulum effect. *Proceedings of the Institution of Mechanical Engineers, Part C: Journal of Mechanical Engineering Science*, 233(10):3678–3689, 2019a.

H. Ouyang, J. Wang, G. Zhang, L. Mei, and X. Deng. Novel adaptive hierarchical sliding mode control for trajectory tracking and load sway rejection in double-pendulum overhead cranes. *IEEE Access*, 7:10353–10361, 2019b.

H. Ouyang, B. Zhao, and G. Zhang. Swing reduction for double-pendulum three-dimensional overhead cranes using energy-analysis-based control method. *International Journal of Robust and Nonlinear Control*, 31(9):4184–4202, 2021.

A. Ovseevich and I. Ananievski. Robust feedback control for a linear chain of oscillators. *Journal of Optimization Theory and Applications*, 188(1):307–316, 2021.

A. I. Ovseevich and A. K. Fedorov. Feedback control for damping a system of linear oscillators. *Automation and Remote Control*, 76(11):1905–1917, 2015.

H. Park, D.-K. Chwa, and K.-S. Hong. A feedback linearization control of container cranes: Varying rope length. *International Journal of Control, Automation, and Systems*, 5(4):379–387, 2007.

M. Park, D. Chwa, and S. Hong. Antisway tracking control of overhead cranes with system uncertainty and actuator nonlinearity using an adaptive fuzzy sliding-mode control. *IEEE Transactions on Industrial Electronics*, 55(11): 3972–3984, 2008.

M. Park, D. Chwa, and M. Eom. Adaptive sliding-mode antisway control of uncertain overhead cranes with high-speed hoisting motion. *IEEE Transactions on Fuzzy Systems*, 22(5):1262–1271, 2014.

K. C. C. Peng, W. Singhose, and P. Bhaumik. Using machine vision and hand-motion control to improve crane operator performance. *IEEE Transactions on Systems, Man, and Cybernetics - Part A: Systems and Humans*, 42 (6):1496–1503, 2012.

A. Piazzi and G. Marro. Robust stability using interval analysis. *International Journal of Systems Science*, 27(12): 1381–1390, 1996.

A. Piazzi and A. Visioli. Optimal dynamic-inversion-based control of an overhead crane. *IEE Proceedings - Control Theory and Applications*, 149:405–411(6), 2002.

D. Qian and J. Yi. Hierarchical sliding mode control for under-actuated cranes. *Heidelberg, Ber: Springer*, 2016.

W. Quan and Q. Chang. Variable-length cable dynamics of payout reel-in with a vertically tethered underwater drill rig. *IEEE Acess*, 8:66625–66636, 2020.

L. Ramli, Z. Mohamed, A. M. Abdullahi, H. Jaafar, and I. M. Lazim. Control strategies for crane systems: A comprehensive review. *Mechanical Systems and Signal Processing*, 95:1–23, 2017.

F. Rauscher and O. Sawodny. Modeling and control of tower cranes with elastic structure. *IEEE Transactions on Control Systems Technology*, 29(1):64–79, 2021.

M. Reeken. The equation of motion of a chain. *Mathematische Zeitschrift*, 155(3):219–237, 1977.

Y. Ren, M. Chen, and Q. Wu. Disturbance observer-based boundary control for a suspension cable system moving in the horizontal plane. *Transactions of the Institute of Measurement and Control*, 41(2):340–349, 2019.

M. Reyhanoglu, A. van der Schaft, N. McClamroch, and I. Kolmanovsky. Dynamics and control of a class of underactuated mechanical systems. *IEEE Transactions on Automatic Control*, 44(9):1663–1671, 1999.

Y. Sakawa and Y. Shindo. Optimal control of container cranes. *Automatica*, 18(3):257–266, 1982.

H. Sano, K. Ohishi, T. Kaneko, and H. Mine. Anti-sway crane control based on dual state observer with sensor-delay correction. In *2010 11th IEEE International Workshop on Advanced Motion Control (AMC)*, pages 679–684, 2010.

D. Schindele and H. Aschemann. Fast nonlinear mpc for an overhead travelling crane. *IFAC Proceedings Volumes*, 44(1):7963–7968, 2011.

X. Shao, J. Zhang, X. Zhang, Z. Zhao, and Z. Chen. A novel anti-swing and position control method for overhead crane. *Science Progress*, 103(1):1–24, 2020.

P. Shen and R. J. Caverly. Noncolocated passivity-based control of a 2 dof tower crane with a flexible hoist cable. In *2020 American Control Conference (ACC)*, pages 5046–5051, 2020.

P.-Y. Shen, J. Schatz, and R. J. Caverly. Passivity-based adaptive trajectory control of an underactuated 3-DOF overhead crane. *Control Engineering Practice*, 112:104834, 2021.

H. Shi, F. Yao, Z. Yuan, S. Tong, Y. Tang, and G. Han. Research on nonlinear coupled tracking controller for double pendulum gantry cranes with load hoisting/lowering. *Nonlinear Dynamics*, pages 1–16, 2022.

W. Singhose, W. Seering, and N. Singer. Shaping inputs to reduce vibration: a vector diagram approach. In *Proceedings., IEEE International Conference on Robotics and Automation*, pages 922–927 vol.2, 1990.

W. Singhose, L. Porter, M. Kenison, and E. Kriikku. Effects of hoisting on the input shaping control of gantry cranes. *Control Engineering Practice*, 8(10):1159–1165, 2000.

W. Singhose, D. Kim, and M. Kenison. Input Shaping Control of Double-Pendulum Bridge Crane Oscillations. *Journal of Dynamic Systems, Measurement, and Control*, 130(3), 2008.

W. E. Singhose, L. J. Porter, and W. P. Seering. Input shaped control of a planar gantry crane with hoisting. In *Proceedings of the 1997 American Control Conference*, volume 1, pages 97–100, 1997.

J. Smoczek and J. Szpytko. Particle swarm optimization-based multivariable generalized predictive control for an overhead crane. *IEEE/ASME Transactions on Mechatronics*, 22(1):258–268, 2017. doi: 10.1109/TMECH.2016.2598606.

N. Sun and Y. Fang. New energy analytical results for the regulation of underactuated overhead cranes: An end-effector motion-based approach. *IEEE Transactions on Industrial Electronics*, 59(12):4723–4734, 2012.

N. Sun and Y. Fang. Nonlinear tracking control of underactuated cranes with load transferring and lowering: Theory and experimentation. *Automatica*, 50:2350–2357, 2014.

N. Sun, Y. Fang, and X. Zhang. Energy coupling output feedback control of 4-dof underactuated cranes with saturated inputs. *Automatica*, 49(5):1318–1325, 2013.

N. Sun, Y. Fang, H. Chen, and B. He. Adaptive nonlinear crane control with load hoisting/lowering and unknown parameters: Design and experiments. *IEEE/ASME Transactions on Mechatronics*, 20(5):2107–2119, 2015.

N. Sun, Y. Fang, H. Chen, and B. Lu. Amplitude-saturated nonlinear output feedback antiswing control for underactuated cranes with double-pendulum cargo dynamics. *IEEE Transactions on Industrial Electronics*, 64(3): 2135–2146, 2017.

N. Sun, Y. Wu, H. Chen, and Y. Fang. An energy-optimal solution for transportation control of cranes with double pendulum dynamics: Design and experiments. *Mechanical Systems and Signal Processing*, 102:87–101, 2018.

N. Sun, Y. Wu, Y. Fang, and H. Chen. Nonlinear antiswing control for crane systems with double-pendulum swing effects and uncertain parameters: Design and experiments. *IEEE Transactions on Automation Science and Engineering*, 15(3):1413–1422, 2018.

N. Sun, T. Yang, Y. Fang, Y. Wu, and H. Chen. Transportation control of double-pendulum cranes with a nonlinear Quasi-PID scheme: Design and experiments. *IEEE Transactions on Systems, Man, and Cybernetics: Systems*, 49 (7):1408–1418, 2019.

N. Sun, J. Zhang, X. Xin, T. Yang, and Y. Fang. Nonlinear output feedback control of flexible rope crane systems with state constraints. *IEEE Access*, 7:136193–136202, 2019.

R. Tang and J. Huang. Control of bridge cranes with distributed-mass payloads under windy conditions. *Mechanical Systems and Signal Processing*, 72-73:409–419, 2016.

P. Tomei. A simple PD controller for robots with elastic joints. *IEEE Transactions on Automatic Control*, 36(10): 1208–1213, 1991.

R. Toxqui, W. Yu, and X. Li. Anti-swing control for overhead crane with neural compensation. In *The 2006 IEEE International Joint Conference on Neural Network Proceedings*, pages 4697–4703. IEEE, 2006.

L. A. Tuan and S.-G. Lee. Sliding mode controls of double-pendulum crane systems. *Journal of Mechanical Science and Technology*, 27(6):1863–1873, 2013.

L. A. Tuan, G.-H. Kim, and S.-G. Lee. Partial feedback linearization control of the three dimensional overhead crane. In *2012 IEEE International Conference on Automation Science and Engineering (CASE)*, pages 1198–1203, 2012.

L. A. Tuan, S.-G. Lee, D. H. Ko, and L. C. Nho. Combined control with sliding mode and partial feedback linearization for 3d overhead cranes. *International Journal of Robust and Nonlinear Control*, 24(18):3372–3386, 2014.

F. Ubertini. Active feedback control for cable vibrations. *Smart Structures and Systems*, 4(4):407–428, 2008.

J. Vaughan, D. Kim, and W. Singhose. Control of tower cranes with double-pendulum payload dynamics. *IEEE Transactions on Control Systems Technology*, 18(6):1345–1358, 2010.

J. Vaughan, E. Maleki, and W. Singhose. Advantages of using command shaping over feedback for crane control. In *Proceedings of the 2010 American Control Conference*, pages 2308–2313, 2010.

T. Vyhlídal, V. Kučera, and M. Hromčík. Signal shaper with a distributed delay: Spectral analysis and design. *Automatica*, 49(11):3484–3489, 2013.

C. Vázquez, J. Collado, and L. Fridman. Super twisting control of a parametrically excited overhead crane. *Journal of the Franklin Institute*, 351(4):2283–2298, 2014.

T. Wang, N. Tan, J. Qiu, Y. Yu, X. Zhang, Y. Zhai, R. D. Labati, V. Piuri, and F. Scotti. Global-equivalent sliding mode control method for bridge crane. *IEEE Access*, pages 1–1, 2021a.

T. Wang, N. Tan, X. Zhang, G. Li, S. Su, J. Zhou, J. Qiu, Z. Wu, Y. Zhai, R. Donida Labati, V. Piuri, and F. Scotti. A time-varying sliding mode control method for distributed-mass double pendulum bridge crane with variable parameters. *IEEE Access*, 9:75981–75992, 2021b. doi: 10.1109/ACCESS.2021.3079303.

L. Wei, T. Limin, and J. Zhengnan. Research on anti-swing characteristic of redundancy cable-driven parallel robot. In *2017 IEEE 2nd Advanced Information Technology, Electronic and Automation Control Conference (IAEAC)*, pages 1504–1508, 2017.

G. Weiping, L. Diantong, Y. Jianqiang, and Z. Dongbin. Passivity-based-control for double-pendulum-type overhead cranes. In *2004 IEEE Region 10 Conference TENCON 2004.*, volume Vol. 4, pages 546–549, 2004.

J. Winget and R. Huston. Cable dynamics–a finite segment appraoch. *Computers and Structures*, 6:475–480, 1981.

T. Wu, M. Karkoub, H. Wang, H. Chen, and T. Chen. Robust tracking control of mimo underactuated nonlinear systems with dead-zone band and delayed uncertainty using an adaptive fuzzy control. *IEEE Transactions on Fuzzy Systems*, 25(4):905–918, 2017. doi: 10.1109/TFUZZ.2016.2586970.

X. Wu and X. He. Enhanced damping-based anti-swing control method for underactuated overhead cranes. *IET Control Theory & Applications*, 9(12):1893–1900, 2015.

X. Wu and X. He. Partial feedback linearization control for 3D underactuated overhead crane systems. *ISA Transactions*, 65:361–370, 2016.

X. Wu and X. He. Nonlinear energy-based regulation control of three-dimensional overhead cranes. *IEEE Transactions on Automation Science and Engineering*, 14(2):1297–1308, 2017.

X. Wu, X. He, N. Sun, and Y. Fang. A novel anti-swing control method for 3-D overhead cranes. In *2014 American Control Conference*, pages 2821–2826, 2014.

Z. Wu and X. Xia. Optimal motion planning for overhead cranes. *IET Control Theory & Applications*, 8:1833–1842(9), 2014.

Z. Wu, X. Xia, and B. Zhu. Model predictive control for improving operational efficiency of overhead cranes. *Nonlinear Dynamics*, 79(4):2639–2657, 2015.

Z. Xi and T. Hesketh. Discrete time integral sliding mode control for overhead crane with uncertainties. *IET Control Theory & Applications*, 4:2071–2081(10), 2010. ISSN 1751-8644.

X. Xing, H. Yang, and J. Liu. Vibration control for nonlinear overhead crane bridge subject to actuator failures and output constraints. *Nonlinear Dynamics*, 101(1):419–438, 2020.

J. Yang and K. Yang. Adaptive control for 3-D overhead crane systems. In *2006 American Control Conference*, pages 6 pp.–, 2006.

Y. Yang, D. Zhang, H. Xi, and G. Zhang. Anti-swing control and trajectory planning of quadrotor suspended payload system with variable length cable. *Asian Journal of Control*, n/a(n/a), 2021.

J. Yi, N. Yubazaki, and K. Hirota. Anti-swing and positioning control of overhead traveling crane. *Information Sciences*, 155(1-2):19–42, 2003.

J. Yoon, W. Singhose, J. Vaughan, G. Ramirez, M. Kim, and S. Tawde. Dynamics and control of crane payloads that bounce and pitch during hoisting. *Proc. ASME Int. Des. Eng. Tech. Conf. Comput. Inf. Eng. Conf. DETC2009*, pages 871–880, 2010. San Diego, USA.

J. Yoon, S. Nation, W. Singhose, and J. Vaughan. Control of crane payloads that bounce during hoisting. *IEEE Transactions on Control Systems Technology*, 22(3):1233–1238, 2014.

K. Yoshida and H. Kawabe. A design of saturating control with a guaranteed cost and its application to the crane control system. *IEEE Transactions on Automatic Control*, 37(1):121–127, 1992.

Y. Yoshida and H. Tabata. Visual feedback control of an overhead crane and its combination with time-optimal control. In *2008 IEEE/ASME International Conference on Advanced Intelligent Mechatronics*, pages 1114–1119. IEEE, 2008.

J. Yu, F. L. Lewis, and T. Huang. Nonlinear feedback control of a gantry crane. In *Proceedings of 1995 American Control Conference - ACC'95*, volume 6, pages 4310–4315 vol.6, 1995. doi: 10.1109/ACC.1995.532748.

M. Zhang. Finite-time model-free trajectory tracking control for overhead cranes subject to model uncertainties, parameter variations and external disturbances. *Transactions of the Institute of Measurement and Control*, 41(12): 3516–3525, 2019.

M. Zhang, X. Ma, X. Rong, X. Tian, and Y. Li. Adaptive tracking control for double-pendulum overhead cranes subject to tracking error limitation, parametric uncertainties and external disturbances. *Mechanical Systems and Signal Processing*, 76-77:15–32, 2016.

M. Zhang, X. Ma, X. Rong, X. Tian, and Y. Li. Error tracking control for underactuated overhead cranes against arbitrary initial payload swing angles. *Mechanical Systems and Signal Processing*, 84:268–285, 2017a.

M. Zhang, X. Ma, X. Rong, R. Song, X. Tian, and Y. Li. An enhanced coupling nonlinear tracking controller for underactuated 3d overhead crane systems. *Asian Journal of Control*, 20(5):1839–1854, 2018.

S. Zhang, X. He, Q. Chen, and Y. Feng. Improved energy dissipation control of overhead cranes. *Asian Journal of Control*, 22(4):1729–1735, 2020.

X. Zhang, Y. Fang, and N. Sun. Minimum-time trajectory planning for underactuated overhead crane systems with state and control constraints. *IEEE Transactions on Industrial Electronics*, 61(12):6915–6925, 2014.

Z. Zhang, Y. Wu, and J. Huang. Differential-flatness-based finite-time anti-swing control of underactuated crane systems. *Nonlinear Dynamics*, 87:1749–1761, 2017b.

B. Zhao, H. Ouyang, and M. Iwasaki. Motion trajectory tracking and sway reduction for double-pendulum overhead cranes using improved adaptive control without velocity feedback. *IEEE/ASME Transactions on Mechatronics*, pages 1–10, 2021.

Y. Zhao and H. Gao. Fuzzy-model-based control of an overhead crane with input delay and actuator saturation. *IEEE Transactions on Fuzzy Systems*, 20(1):181–186, 2012. doi: 10.1109/TFUZZ.2011.2164083.